Subspace Control of Nitrogen Vacancy centers at Zero Field

by

Romain Ruhlmann

A thesis
presented to the University of Waterloo
in fulfillment of the
thesis requirement for the degree of
Master of Science
in
Physics (Quantum Information)

Waterloo, Ontario, Canada, 2020

© Romain Ruhlmann 2020

I hereby declare that I am the sole author of this thesis. This is a true copy of the thesis, including any required final revisions, as accepted by my examiners.

I understand that my thesis may be made electronically available to the public.

Abstract

Nitrogen-Vacancy centers negatively charged (NV^-) are spin-1 objects in diamond. In the absence of a magnetic field, two of its levels are degenerate, which is why a field is often used to lift the degeneracy and allow easy access to each level. Following the work Alegre, Mrózek and others [1–3], it was established that circularly polarized microwaves could address the difference in angular momentum between each level, making the introduction of the magnetic field unnecessary. These methods were assuming that the position of the microwave sources and the NV^- was ideal. There was then work to be done to enable circularly polarized microwaves to work with an NV^- at any position. To handle this freedom in the NV^- position, characterization methods need to be developed to measure it and take it into account. This can be done with a custom built confocal microscope, taking into account the orientation of a single NV^-.

Acknowledgements

I would like to thank people for their help with this project, closely and remotely related; Ian Hincks, Madelaine Liddy, Guanru Feng, Dusan Sarenca, Zimeng Wang, Thomas Alexander, Peter Sprenger, and Yuanye Zhu.

Thank you to the people that helped me maintain sanity: Stefanie Beale for obvious reasons, Cliffor Plesha, Vic Newell, Kayla Hardie, and Chester

Finally, thanks to professor David Cory, my supervisor, for his expectations, encouraging me to maintain rigor throughout the project.

Dedication

This is dedicated to the one I love.

Table of Contents

List of Tables x

List of Figures xi

Glossary xiv

List of Symbols xv

Introduction 1

Outline of the thesis 2

1 Physics of the Nitrogen-Vacancy Center 3

1.1 Geometry of the Nitrogen-Vacancy center 3

1.2 Spin operators 4

1.3 Electronic and optical structure 6

1.4 Initialization and measurement 10

1.4.1 Time dependent evolution 11

1.5 Rotating Wave Approximation for NV centers 16

1.5.1 Transverse Magnetic Field 19

2 Confocal Microscopy **22**
2.1 Laser Source . . . 23
2.1.1 Description . . . 24
2.1.2 Maintenance . . . 25
2.2 Switching arm . . . 26
2.2.1 Description . . . 27
2.2.2 Maintenance . . . 29
2.3 Mode Shaping Arm . . . 29
2.3.1 Description . . . 29
2.3.2 Maintenance . . . 30
2.4 Scanning Optics . . . 31
2.4.1 Description . . . 32
2.4.2 Maintenance . . . 32
2.5 Microscope Objective . . . 34
2.5.1 Description . . . 34
2.5.2 Maintenance . . . 36
2.6 Detector . . . 37
2.6.1 Description . . . 38
2.6.2 Maintenance . . . 39

3 Characterization of two microwave sources, theory and experiments **42**
3.1 Transitions available under different conditions and their Rabi frequencies . 42
3.1.1 High field . . . 43
3.1.2 No field . . . 46
3.1.3 Insight from the previous section . . . 48
3.2 Two wires board . . . 49
3.3 Two microwave sources . . . 54
3.3.1 Perpendicular microwave sources . . . 54

3.3.2 Microwave sources with arbitrary microwave orientation 55
3.3.3 Microwave sources with arbitrary microwave orientation and no magnetic field 56
3.3.4 Microwave sources with arbitrary microwave orientation and magnetic field 57
3.4 Theoretical target 58
3.4.1 Data collection 58
3.5 Relative amplitude 60
3.6 Relative phase 61
3.7 Absolute phase 63
3.8 Relative phase at low field 66
3.8.1 Discrete Ramsey experiment at zero field 66
3.8.2 Phase-phase experiment at zero field 67
3.9 Confirmation of the characterization 68
3.9.1 Confirmation of relative amplitudes 68
3.9.2 Confirmation of relative phase 68

4 Improvements on the current design **75**
4.1 Current issues 75
4.2 Proposition for a new sample board 77
4.3 Improvement for the magnet 79
4.4 Synchronize the devices 80

5 Extension to ensemble control **82**

Conclusion **89**

References **89**

Appendices **95**

A Introduction to M squares measurement by ISO **96**

B Choosing a fiber coupler **97**

C Common experimental problems and solutions **98**

C.1 Hard reset of the Micro Stepper and piezo controller 98

C.2 Sweeping the phase 99

C.3 AWG Socket Server protocol 99

D Instructions to reset the AWG Socket Server **100**

E Ad hoc confirmation of microwave control **104**

F Commands relevant to synchronizing the devices to the same clock **107**

List of Tables

2.1 List of the components of the custom built confocal microscope. Labels of this table correspond to those of figure 2.1 23

3.1 Relative Rabi frequencies under different regimes and with different objectives. $\perp$ expresses that the microwave sources are perpendicular. 49

3.2 Fit of the Rabi oscillations displayed in figure 3.9 using MATLAB fit function. Function fitted: $\mathrm{Tr}[\rho\,|0\rangle\langle 0|] = A\cos(2\pi\omega t)e^{-t/T_2} + C$ 61

3.3 Fit of the Discrete Ramsey experiment oscillations displayed in figure 3.12 using MATLAB fit function. Function fitted: $\mathrm{Tr}[\rho\,|0\rangle\langle 0|] = A\cos(\pi(2\theta)n + \phi)e^{-t/T_2} + C$ 63

3.4 Fit of the pulsed experiment displayed in figure 3.13 using MATLAB fit function. Function fitted: $\mathrm{Tr}[\rho\,|0\rangle\langle 0|] = A\cos(2\pi\phi_2 + \psi_i) + C$ 66

3.5 Rabi Frequency measured under different conditions. 69

5.1 Frame transformation between the crystal frame and each NV center frame 83

5.2 Unit vectors of the laboratory frame expressed in NV center frames 84

5.3 Amplitudes of each operator in the frame of the $(1,1,1)$ NV center in the $\langle 1\,1\,1\rangle$ diamond cut 84

C.1 Values to provide to the "Sweeps" environment to perform an experiment sweeping ph1 from $\pi/3$ to $5\pi/6$ in 25 steps 99

List of Figures

1.1 Diamond structure and single NV center 4

1.2 Full and simplified energy diagrams of the NV center. 7

1.3 NV center dynamics with laser and microwaves on or off, starting in $|g,0\rangle\langle g,0|$ or $(|g,-\rangle\langle g,-| + |g,+\rangle\langle g,+|)/2$. 13

1.4 Outline of a single shot of an experiment. 15

1.5 Simulated example of optimizing measurement time for a low visibility experiment. 17

2.1 Diagram of the experimental setup. Part numbers correspond to the list in table 2 24

2.2 Diagram of the laser head in its enclosing, with mirrors to guide the beam outside 25

2.3 Temporal stability of the laser power 27

2.4 Diagram of the AOM with telescope focusing the beam onto its center point 27

2.5 Mode Shaping Arm, with two mirrors mounted on spring loaded screws, to adjust tilt and yaw of the beam at each mirror. 30

2.6 Scanning optics. Note that the last mirror (leftmost) deflects the beam downward (into the page), whereas we show it here remaining in the page for clarity. 32

2.7 Evolution of the beam width at the pinhole as a function of the displacement of one lens at a time. Rectangle on 2.7b shows the domain and image chosen for the graph on the left. 33

2.8 Microscope objective sitting on the sample. 35

2.9 From left to right, reflected pattern when the sample (mirror) is too high, at the right height or too low. 37

2.10 Avalanche Photodiode collecting light coming through the pinhole. 38

3.1 Difference in population ($P(t)$) if the qubit approximation is made or not, in 100 MHz magnetic field, with Rabi Frequency of 6 MHz 45

3.2 Top view of the parallel wires setup on a PCB. 50

3.3 Cross section of the diamond (seen from the side of fig: 3.2a). The NV of interest is not necessarily in the center and its orientation is not predetermined. 51

3.4 Response of the circuit for transmission. Transmissions forward and backward are similar. Their difference is less that 0.3 dB on average. 52

3.5 Reflections from and to the same port 53

3.6 New circuit with 2 control wires on the sample holder 54

3.7 Pulse diagram of the Rabi Experiment. 60

3.8 Rabi experiment repeated 65 million times for each wire. Line connecting each point is given as a guide to the eye. 70

3.9 Normalized data from 3.8. Line connecting the points is a guide to the eye. Fit results given in table 3.2 71

3.10 Power spectrum of the Rabi flops 71

3.11 Pulse diagram of the Discrete Ramsey Experiment. 72

3.12 Discrete Ramsey experiment repeated 75 million times. 72

3.13 Evolution of the population of $|0\rangle$ as the two $\pi/2$ pulses get in and out of alignment. 73

3.14 An expected frequency of 1Ω corresponds to a single transition under a magnetic field. Expected ratios are treated in section 3.1 and summarized in table 3.5 74

4.1 Phase accumulated in the wires from the channels 1 and 2 of the AWG (I and Q) to the mixer 76

4.2 Electrical length of the wires from the channels 3 and 4 of the AWG (I and Q) to the mixer 77

4.3 Electrical length of the wires from the mixers 1 and 2 to the input of the sample board 78
4.4 Current and suggested PCB sample holders. 79
4.5 Current and suggested magnet holders. 80

5.1 Example of pulse sequence producing a $\pi/2$ rotation about S_x^+ for each NV center orientation. 87
5.2 Trajectories in a Bloch Sphere representation as per our simulation. 88

E.1 CW ESR experiment with similar contribution from each wire, $\phi_1 = 0$ and ϕ_2 defined for each curve. 106

Glossary

AOM Acousto Optic Modulator 26

APD Avalanche Photo Diode 38

AWG Arbitrary Waveform Generator 51, 76, 80

CCD Charge-Couple Device 25

CW Continuous Wave 104

DQT Double Quantum Transition 6, 54, 58

ISC Inter-Sysyem Crossing 9

NV Nitrogen-Vacancy 1, 3–5, 22, 42, 56, 62, 82, 89, 98

PAS Principal Axis System 3, 5, 56, 62, 85

RWA Rotating Frame Approximation 16, 44, 86

SQT Single Quantum Transition 5, 58

$\mathbf{TEM_{00}}$ Lowest order of the Transverse Electromagnetic Mode orthogonal to the travelling wave 26, 29

VNA Vector Network Analyzer 49, 50

ZFS Zero Field Splitting 4, 5, 18, 53, 86

List of Symbols

Δ Zero Field Splitting (rad s^{-1}) 4

Λ Accoustic wavelength (m) 28

L Grating thicnkness (m) 28

B_z $\hat{z}$ component of the magnetic field (Gauss) 7

f Focal Length (mm) 28, 97

γ_e Magnetic moment (MHz/Gauss) 7

λ Wavelength (m) 28

M^2 Beam quality factor (unitless) 26

v_a Acoustic velocity (m/s) 28

Introduction

Nitrogen-Vacancy (NV) centers are Spin-1 defects in diamonds that have gained a lot of attraction in recent research due to their long coherence times at room temperatures [4, 5], and the fact that their state can be individually initialized and measured with visible light and manipulated with microwaves [6, 7]. Their coherence time can reach milliseconds at room temperatures [4, 5], while reaching seconds at low temperatures (77K) [8]. They were demonstrated to possess high sensitivity for alternating magnetic fields on the sub micrometer scale [5, 9–13]. Furthermore, they have been used as temperature sensors at room temperature [14] and have been demonstrated to be sensitive to electric fields [15]. Thanks to these useful and versatile properties, numerous applications have been proposed in the field of quantum sensing and life sciences [16].

A common feature of the NV center experiments detecting alternating magnetic fields is looking at a subset of the spin levels while using a non-negligible constant field. As a result, these experiments are not well suited to measure small and static fields [10]. A more appropriate approach for small magnetic fields is to make use of two microwave sources to generate circularly polarized excitation and take advantage of the polarization selection rules, as previously demonstrated by Alegre, Mrózek and others [1–3]. It was demonstrated that for a single NV center, using circularly polarized pulses, one could generate single transitions between levels that would otherwise be degenerate and indistinguishable. Previous work used the geometry of two perpendicular wires and looked at NV centers placed above the intersection point [1, 2] and also two parallel wires and looked at NV centers placed on a line equidistant from each wire [3]. The last case, the most interesting one, deals with the situation in which we have access to two independent microwave sources. In this thesis, we explore methods to manipulate single NV centers in a much larger volume above two parallel wires. This is accomplished by determining the optimal interaction parameters between the microwave sources and the NV center of interest. Concrete techniques for determining the optimal amplitude and phase of the microwave sources are presented. This work enables more sensitive probes of magnetic fields and lays the ground work for

expanding these techniques to ensemble of NV centers.

Outline of the thesis

The thesis is separated in 5 chapters.

In chapter 1, we will introduce the NV center, its spin-1 operators and the internal transition rates that describe its optical initialization and read-out.

In chapter 2, we will describe the custom built confocal microscope that we used to conduct the experiments. Since this optical table has been assembled by Om Patange in the previous years [17], we will focus on detailing the maintenance of this optical table.

In chapter 3, we will describe the methods to characterize the amplitude and phase of the microwave sources as well as present the results we obtained with the sus mentioned ODMR setup.

In chapter 4, we will describe the current limitations of the setup such as inconsistent electrical length and inability to turn the magnetic field off and we will offer solutions to address each of them.

In chapter 5, we will suggest that the use of homogeneous microwave sources such as coils can allow one to use the methods described earlier to now manipulate ensemble of NV centers, one orientation at a time, to increase the signal read-out.

Chapter 1

Physics of the Nitrogen-Vacancy Center

1.1 Geometry of the Nitrogen-Vacancy center

An ideal diamond lattice consists of a collection of Carbons, each connected to four other Carbons, in a tetrahedral organization. Its unit cell is shown in figure 1.1a. Impurities can find themselves at these Carbon sites, changing the properties of the diamond. One such impurity is the Nitrogen-Vacancy center, a defect where one Carbon atom is replaced by a Nitrogen atom, which has a vacant neighbour, with no Carbon[18], as depicted in figure 1.1b. This impurity comes in two flavours: NV^- and NV^0. The NV^- center is the polarized version of the electrically neutral NV^0. With 5 electrons coming from the Nitrogen (2) and the nearby Carbons (3), it acquires an extra electron from somewhere else in the matrix or from outside the matrix [19–21]. The defect then has a total of 6 electrons (even), whose organization generates the spin-1 object [19] [22]. We will consider a model where the center of the defect is the vacancy, surrounded by 3 atoms of Carbon and one of Nitrogen. This defect then displays a C_{3v} symmetry, with 3 axes of reflection and 3 rotations of 120 deg around the Nitrogen-Vacancy axis. Since this is the main axis, the one that is defining the symmetry, it is called the Principal Axis System (PAS). The other argument defending the name is that the organization of the orbitals generated by the 6 electrons shields the quantum object against magnetic fields orthogonal to the PAS. Magnetic fields are then mostly affecting the NV center along that axis, the Principal Axis System.

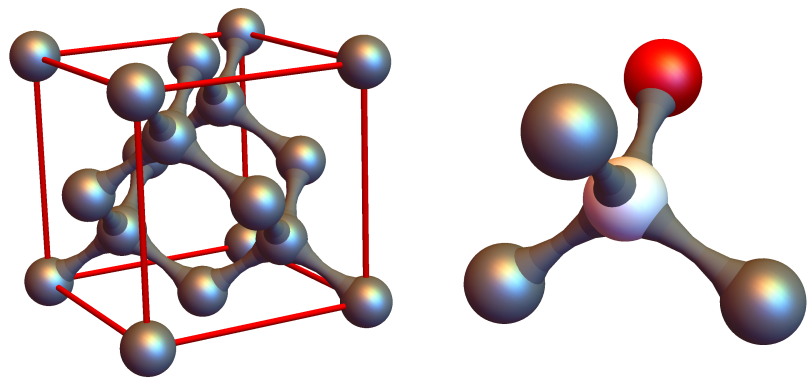

(a) Unit cell of the diamond

(b) Nitrogen (red) and Vacancy (white) center, surrounded by three atoms of Carbon (gray)

Figure 1.1: Diamond structure and single NV center

1.2 Spin operators

This section describes how the different transitions, between the optically ground state and the optically excited state, allow for preparation and measurement of the spin of the object.

The structure of the NV center is described by the interaction of two indistinguishable electrons, in the absence of a magnetic field. This $\sigma \cdot \sigma$ then displays eigenvectors split into a singlet and triplet. In the up-down picture, the eigenvectors are then: $|\uparrow\uparrow\rangle$, $\frac{|\uparrow\downarrow\rangle+|\downarrow\uparrow\rangle}{\sqrt{2}}$ and $|\downarrow\downarrow\rangle$ for the triplet and $\frac{|\uparrow\downarrow\rangle-|\downarrow\uparrow\rangle}{\sqrt{2}}$ for the singlet. In this basis, the $\sigma_x^1 + \sigma_x^2$ operator maps eigenvectors of the triplet to the triplet and leaves the singlet untouched. Since the triplet remains separate from the singlet, we focus our attention to it, concentrating our efforts on the spin-1 obejct.

Before describing the dynamics within the spin-1 of the NV centers, we need to establish some convention for its operators. We define the principal axis as the $\hat{z}$. This is the direction along which the NV center exhibits a Zero Field Splitting (ZFS) with value Δ, along the Nitrogen-Vacancy bond, along which the angular momentum is discretized.

Hence, the three basis vectors we use will be the eigenvectors of the angular momentum

operator S_z:

$$|m_s = +1\rangle = \begin{pmatrix}1\\0\\0\end{pmatrix};\ |m_s = 0\rangle = \begin{pmatrix}0\\1\\0\end{pmatrix};\ |m_s = -1\rangle = \begin{pmatrix}0\\0\\1\end{pmatrix}$$

As we focus our attention on the NV center as a spin 1 object, we will need 9 linearly independent spin operators to fully describe the dynamics of the system.

After the angular momentum operator S_z, we will need 8 other spin operators.

Let's consider the S_z^2 operator, describing the zero field splitting. In the absence of a magnetic field, the degeneracy of the triplet states can be lifted by the geometry of the object. In the case of spherical orbitals, all three states of the triplet are degenerate. In the case of an deformation of the orbitals along the $\hat{z}$ axis, there will be a Zero Field Splitting between the states $|m_s = 0\rangle$ and the others while a deformation of the orbitals along $\hat{x}$ or $\hat{y}$ will induce a splitting between the $|\pm 1\rangle$ states. In the case of the NV center, with a C_{3v} symmetry along the PAS, the ZFS will be along the $\hat{z}$ direction, separating the state with angular momentum 0 from the two others. It is defined as the square of the S_z operator. In matrix form:

$$S_z = \begin{pmatrix}1 & 0 & 0\\0 & 0 & 0\\0 & 0 & -1\end{pmatrix};\ S_z^2 = \begin{pmatrix}1 & 0 & 0\\0 & 0 & 0\\0 & 0 & 1\end{pmatrix}$$

The next pair are the S_x and S_y operators, which are derived from the usual commutative properties of angular momentum [23] while S'_x and S'_y are operators that emerge when S_y and S_x are brought in the rotating frame of S_z^2. Since the angular momentum difference between each pair of level is of 1, we will refer to them as Single Quantum Transitions (SQTs). We will cover that frame transformation in a further section (see section 3.1.1).

$$S_x = \begin{pmatrix}0 & 1/\sqrt{2} & 0\\1/\sqrt{2} & 0 & 1/\sqrt{2}\\0 & 1/\sqrt{2} & 0\end{pmatrix};\ S'_x = i[S_z^2, S_y] = \begin{pmatrix}0 & 1/\sqrt{2} & 0\\1/\sqrt{2} & 0 & -1/\sqrt{2}\\0 & -1/\sqrt{2} & 0\end{pmatrix}$$

$$S_y = \begin{pmatrix}0 & -i/\sqrt{2} & 0\\i/\sqrt{2} & & -i/\sqrt{2}\\0 & i/\sqrt{2} & 0\end{pmatrix};\ S'_y = i[S_z^2, S_x] = \begin{pmatrix}0 & i/\sqrt{2} & 0\\-i/\sqrt{2} & 0 & -i/\sqrt{2}\\0 & i/\sqrt{2} & 0\end{pmatrix}$$

The last pair of spin operators are the Double Quantum Transitions (DQTs), in and out of phase:

$$S_x^{++} = \begin{pmatrix} 0 & 0 & 1 \\ 0 & 0 & 0 \\ 1 & 0 & 0 \end{pmatrix}; \; S_y^{++} = \begin{pmatrix} 0 & 0 & -i \\ 0 & 0 & 0 \\ i & 0 & 0 \end{pmatrix}.$$

The last operator is trivially the identity:

$$\mathbb{1}_3 = \begin{pmatrix} 1 & 0 & 0 \\ 0 & 1 & 0 \\ 0 & 0 & 1 \end{pmatrix}.$$

1.3 Electronic and optical structure

In this section, we will describe the electronic structure of the NV center and cover the transitions that happen under the effect of laser and microwave excitation.

Previous studies have shown that the ground state of the NV center is a triplet [7, 19, 24]. That ground state can be excited by green light to a meta stable state that rapidly decays to an excited triplet. Since the levels in the meta stable state are only relevant to the excitation of the ground state, we will neglect it for this section. Similarly, a dark transition that happen between the excited state and the ground state occurs through a pair of singlet states but since we use the simplified case where the excited singlet only decays to the ground singlet, we will treat them as a single level (simplified system displayed in figure 1.2. This section and its notation are following previous work from I. Hincks [25], to which we will append a section on microwave dynamics.

Each level of the triplets will be labelled by its angular momentum, +1, 0 or -1. The triplets from the first set, with lower energy, are in the ground state while the others are in the excited state. It is worth noting that the energy difference between each of these levels is dependent on the strains: we are working at room temperature, such that we work with high strains [19]. We will label them $|m, m_s\rangle$, m for the excitation of the triplets (g for ground and e for excited) and m_s for their angular momentum (values from $\{-1, 0, 1\}$). The two triplets are separated by 1.945 eV. The singlet is energetically located between the two sets of triplets and will be labelled $|s\rangle$. See fig. 1.2 for a diagram.

Since these groups of levels are disjoint as far as microwave dynamics go, we will consider the operators to be part of different Hamiltonians in a larger Hilbert space:

$$H_{NV} = H_g \oplus H_e \oplus H_s$$

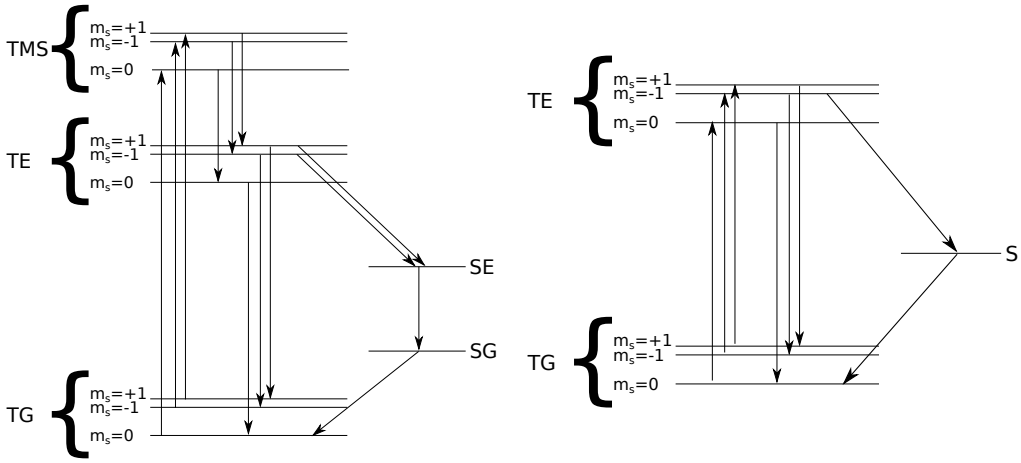

(a) Full energy diagram of the NV center.

(b) Simplified 7 levels model of the energy diagram, used for the simulations. Transition rates defined in text.

Figure 1.2: Full and simplified energy diagrams of the NV center. TMS: Triplet Meta-Stable level. TE: Triplet Excited level. TG: Triplet Ground level. SE: Singlet Excited level. SG: Singlet Ground level. S: Singlet level. $m_s = i$: level with angular momentum i. Energy difference between $m_s = -1$ and $m_s = +1$ is $2\gamma_e B_z$ with γ_e is the gyromagnetic ratio and B_z is the magnetic field along the PAS

Where H_{NV} is the total Hamiltonian, with dimension 7, H_g is limited to the ground states and has dimension 3, H_e is limited to the excited states and has dimension 3 and H_s is limited to the singlet state, with dimension 1.

Neglecting the nearby Nitrogen and any Carbon isotope interactions, the internal electronic Hamiltonian H_0 can then be expressed as

$$H_0 = \Delta_g S_z^2 \oplus \Delta_e S_z^2 \oplus \mathbb{0}_1$$

Where $\Delta_g \approx 2.87$ GHz is the zero field splitting of the ground state, $\Delta_e \approx 1.4$ GHz is the zero field splitting of the excited state [24] and $\mathbb{0}_1$ is the null matrix of dimension 1.

To describe the dynamics within the center, we will use the following basis vectors, eigenvectors of S_z in the ground and the excited state and eigenvector of the singlet state:

$$|g,-1\rangle = \begin{pmatrix}1\\0\\0\\0\\0\\0\\0\end{pmatrix};\ |g,0\rangle = \begin{pmatrix}0\\1\\0\\0\\0\\0\\0\end{pmatrix};\ |g,1\rangle = \begin{pmatrix}0\\0\\1\\0\\0\\0\\0\end{pmatrix};$$

$$|e,-1\rangle = \begin{pmatrix}0\\0\\0\\1\\0\\0\\0\end{pmatrix};\ |e,0\rangle = \begin{pmatrix}0\\0\\0\\0\\1\\0\\0\end{pmatrix};\ |e,1\rangle = \begin{pmatrix}0\\0\\0\\0\\0\\1\\0\end{pmatrix};$$

$$|s\rangle = \begin{pmatrix}0\\0\\0\\0\\0\\0\\1\end{pmatrix}$$

Beyond the Zero Field Splittings, there are few transitions that are allowed in this system, and they will be described by dissipators.

First off, the green laser excites the triplet from the ground state to a meta stable state, higher in energy than the excited state, which then rapidly decays to the excited state. The rate at which this happens depends on the laser power. The excited state decays to the ground state by emitting a red photon. This will prove invaluable for measuring the state of the NV center, which we describe later. Using Lindblad operators, the laser transitions can be described as

$$L_1 = \sqrt{k\gamma_{eg}}(|e,-1\rangle\langle g,-1| + |e,0\rangle\langle g,0| + |e,1\rangle\langle g,1|) \tag{1.1}$$

$$L_2 = \sqrt{\gamma_{eg}}(|g,-1\rangle\langle e,-1| + |g,0\rangle\langle e,0| + |g,1\rangle\langle e,1|) \tag{1.2}$$

Where $\gamma_{eg} = 77$ MHz is the rate of the excited state [19] and $k \in [0,1]$ is a scaling factor associated with the power of the laser: $k = 0$ when the laser is off and $k = 1$ when the laser saturates the NV.

The Inter-Sysyem Crossing (ISC) transitions, normally forbidden because they do not conserve angular momentum between the triplet and the singlet state, are allowed in our case because of extra strains. These transitions link the $|g,-1\rangle$ and $|e,1\rangle$ levels to $|s\rangle$, and $|s\rangle$ to $|g,0\rangle$:

$$L_3 = \sqrt{\gamma_{es}/2}\,|s\rangle\,\langle e,+1| \tag{1.3}$$

$$L_4 = \sqrt{\gamma_{es}/2}\,|s\rangle\,\langle e,-1| \tag{1.4}$$

$$L_5 = \sqrt{\gamma_{sg}}\,|g,0\rangle\,\langle s| \tag{1.5}$$

The rate of decay to the singlet state is $\gamma_{es} = 30$ MHz [19]. Comparing that rate to γ_e shows that this path is taken about a third of the time. Since this transition only emits photons in the Infra-Red range, our counter (in the visible range) will not record such transition and on average, will record about 70% of the maximal amount of photons when the NV center is in the $|e,+1\rangle$ or $|e,-1\rangle$ state as opposed to the $|e,0\rangle$ state. Hence, by applying green, off resonance laser, which excites the stable ground state to its corresponding excited state, we can distinguish between states of the NV center by mean of photon collection. The allowed transitions from the singlet are still under study [19, 26, 27], so for this work, we will consider that the decay happens from the singlet state to the $|g,0\rangle$ state only. The decay rate being $\gamma_{sg} = 3.3$ MHz, we note that this is the slowest decay, the bottleneck of these optical transitions, which is the timescale over which an NV center in the $m_s = \pm 1$ state is darker than an NV center in the $m_s = 0$ state, since this pathway does not emit in the visible range. In consequence, after a time $t = 5 \cdot \frac{\gamma_{es}+\gamma_e}{\gamma_{es}} \cdot 1/\gamma_{sg} \approx 5\ \mu$s, under laser excitation, any NV center can be expected to be polarized to the $|g,0\rangle$ state, regardless of its initial state.

Finally, some spin non-conserving transitions have been observed from the excited to the ground triplet states [19]:

$$L_6 = \sqrt{\gamma_{01}/4}\,|g,0\rangle\,\langle e,+1| \tag{1.6}$$

$$L_7 = \sqrt{\gamma_{01}/4}\,|g,0\rangle\,\langle e,-1| \tag{1.7}$$

$$L_8 = \sqrt{\gamma_{01}/4}\,|g,+1\rangle\,\langle e,0| \tag{1.8}$$

$$L_9 = \sqrt{\gamma_{01}/4}\,|g,-1\rangle\,\langle e,0| \tag{1.9}$$

These transitions are slow ($\gamma_{01} = 1.5$ MHz) and as such, do not contribute extensively to the dynamics of the NV center

For completeness, let's mention that the singlet is treated here, for simplicity, like a single level whereas it was predicted and measured to display a pair of ground and excited states, joined by and infrared transition at 1042 nm whereas the transition from the excited triplet state to the excited singlet state is non radiative, similar to the transition from the singlet ground state to the triplet ground state, using phononic transitions [26].

1.4 Initialization and measurement

All these Lindblad operators can be used in a Lindblad Master Equation to follow the evolution of the density state of an NV center. Using $\rho(t)$ to describe the density matrix of the NV center:

$$\frac{\mathrm{d}\rho(t)}{\mathrm{d}t} = -\mathrm{i}[\mathrm{H}, \rho(\mathrm{t})] + \sum_{\mathrm{i}=1}^{9} (\mathrm{L_i}\rho(\mathrm{t})\mathrm{L_i^\dagger} - (\rho(\mathrm{t})\mathrm{L_i^\dagger}\mathrm{L_i} + \mathrm{L_i^\dagger}\mathrm{L_i}\rho(\mathrm{t}))/2) \tag{1.10}$$

In the absence of time dependent Hamiltonian, we will describe the evolution of the 7-levels model with a rate equation picture.

Let's define the vector of observables:

$$p_{g0}(t) = \mathrm{Tr}[|g,0\rangle \langle g,0| \rho(t)] \tag{1.11}$$
$$p_{g+}(t) = \mathrm{Tr}[|g,+1\rangle \langle g,+1| \rho(t)] \tag{1.12}$$
$$p_{g-}(t) = \mathrm{Tr}[|g,-1\rangle \langle g,-1| \rho(t)] \tag{1.13}$$
$$p_{e0}(t) = \mathrm{Tr}[|e,0\rangle \langle e,0| \rho(t)] \tag{1.14}$$
$$p_{e+}(t) = \mathrm{Tr}[|e,+1\rangle \langle e,+1| \rho(t)] \tag{1.15}$$
$$p_{e-}(t) = \mathrm{Tr}[|e,-1\rangle \langle e,-1| \rho(t)] \tag{1.16}$$
$$p_s(t) = \mathrm{Tr}[|s\rangle \langle s| \rho(t)] \tag{1.17}$$
$$p(t) = \{p_{g0}(t), p_{g+}(t), p_{g-}(t), p_{e0}(t), p_{e+}(t), p_{e-}(t), p_s(t)\} \tag{1.18}$$

Using the Master Equation 1.10 to describe the time evolution of each level (eqn. 1.11 -

1.17), we get a collection of expressions of the following form:

$$
\begin{aligned}
\frac{\mathrm{d}p_{g0}(t)}{\mathrm{d}t} &= \mathrm{Tr}[|g,0\rangle\langle g,0|\,\dot{\rho}(t)] \\
&= \mathrm{Tr}\left[|g,0\rangle\langle g,0|\,(-\mathrm{i}[\mathrm{H},\rho(\mathrm{t})] + \sum_{\mathrm{i}=1}^{9}(\mathrm{L_i}\rho(\mathrm{t})\mathrm{L_i^\dagger} - (\rho(\mathrm{t})\mathrm{L_i^\dagger}\mathrm{L_i} + \mathrm{L_i^\dagger}\mathrm{L_i}\rho(\mathrm{t}))/2))\right] \\
&= ... \\
&= -k\gamma_{eg}p_{g0}(t) + \gamma_{eg}p_{e0}(t) + \frac{\gamma_{01}}{4}(p_{e+}(t) + p_{e-}(t)) + \gamma_{sg}p_s(t)
\end{aligned}
$$

Solving the Master Equation for each level probability, we find that the relationship between $\dot{p}(t)$ and $p(t)$ can be summarized, linearly, under the matrix form $\dot{p}(t) = R \cdot p(t)$ with R:

$$
R = \begin{pmatrix}
-k\gamma_{eg} & 0 & 0 & \gamma_{eg} & \frac{\gamma_{01}}{4} & \frac{\gamma_{01}}{4} & \gamma_{sg} \\
0 & -k\gamma_{eg} & 0 & \frac{\gamma_{01}}{4} & \gamma_{eg} & 0 & 0 \\
0 & 0 & -k\gamma_{eg} & \frac{\gamma_{01}}{4} & 0 & \gamma_{eg} & 0 \\
k\gamma_{eg} & 0 & 0 & \frac{-\gamma_{01}}{2} - \gamma_{eg} & 0 & 0 & 0 \\
0 & k\gamma_{eg} & 0 & 0 & \frac{-\gamma_{01}}{4} - \gamma_{eg} - \frac{\gamma_{es}}{2} & 0 & 0 \\
0 & 0 & k\gamma_{eg} & 0 & 0 & \frac{-\gamma_{01}}{4} - \gamma_{eg} - \frac{\gamma_{es}}{2} & 0 \\
0 & 0 & 0 & 0 & \frac{\gamma_{es}}{2} & \frac{\gamma_{es}}{2} & -\gamma_{sg}
\end{pmatrix}
$$

This is the rate equation.

Note that each column of the rate equation sums to zero to conserve probabilities and that we have no contribution from the Hamiltonian in this rate equation, because each projector is an eigenvector of the Hamiltonian. This argument will change when the Hamiltonian gets some off-axis magnetic field of magnitude comparable to the ZFS or off-axis microwave excitation. We will cover this case in the next section.

1.4.1 Time dependent evolution

An interesting case we will simulate here is to introduce a control Hamiltonian in the previously time independent Hamiltonian. Assuming a microwave control in resonance with the ground state transition and in the absence of other fields, the Hamiltonian becomes

$$
H_{NV} = (\Delta_g S_z^2 + \Omega S_x \cos(\omega t)) \oplus \Delta_e S_z^2 \oplus \mathbb{0}_1 \tag{1.19}
$$

Where Ω is the Rabi drive.

In conjunction with the Lindblad dissipators defined previously, we then have the operators necessary to describe the dynamics during a Continuous Wave experiment, during which we are interested in the steady state of the system under the application of both laser and microwaves. At this point, for visibility in the results, we will consider the $m_s = +1$ and $m_s = -1$ together rather than separate since they undergo very similar transitions and keeping them separate after the simulation will not bring any more insight.

$$p_{g1}(t) = (p_{g+}(t) + p_{g-}(t))/2 \tag{1.20}$$

$$p_{e1}(t) = (p_{e+}(t) + p_{e-}(t))/2 \tag{1.21}$$

To do so, we will use a Mathematica package developed by C. J. Woods and others to simulate quantum states evolution[28]. We will compare what happens over long periods of time (up to 5μs) whether the NV center starts in a state of $|g,0\rangle\langle g,0|$ or $(|g,-\rangle\langle g,-| + |g,+\rangle\langle g,+|)/2$ and whether the microwaves are on or far off resonance; if they are effective (present) or ineffective (absent). The results are displayed in figure 1.3.

In the two first cases (cases (a) and (b)), when the microwaves are on resonance and the transitions are a mix of the Lindblad dissipator and S_x operator, the excited state of the initial state is quick to get populated ($\approx 40-50$ ns) but the situation becomes different based on the initial state. In the first case (case (a)), as p_{g0} gets depopulated, the p_{g1} level gets populated quickly by the microwaves. The singlet state then eventually gets populated. In the second case (case (b)), we have the opportunity to see each transition happen one after the other, as one level gets populated more and more, until its emptying process takes over. The first transition is quickly triggered by the laser excitation, populating p_{e1}. This one then decays to p_s before the microwaves have a real opportunity to populate p_{g0}, simply because of the smaller value chosen for Ω; $\Omega = 20$ MHz in this simulation, close to what we measured for our system. Finally, we notice that we reach an equilibrium state after 5μs, which is identical in both cases, supporting the claim that laser excitation for few μs brings the NV center to a steady state.

In the next two cases (cases (c) and (d)), we simulate the static case, which is to say that we only have the internal Hamiltonian and no contribution from a control Hamiltonian, leaving the meaningful transitions to come from the Lindblad dissipators and be time-independent. When the initial state is p_{g0} (case (c)), the only meaningful transition is the laser excitation (with rate $k\ \gamma_{eg} = 23.1$ MHz) and laser de excitation (with rate $\gamma_{eg} = 77$ MHz), which reach quasi equilibrium within 50 ns, before the spin non-conserving transitions come have a little effect with $\gamma_{01} = 1.5$ MHz). When the initial state is p_{g1} (case (d)), we see how the ground state gets excited (p_{e1} increasing), how this excited population gets transferred to the singlet state (dashed peak at 300-400 ns) and how this singlet state

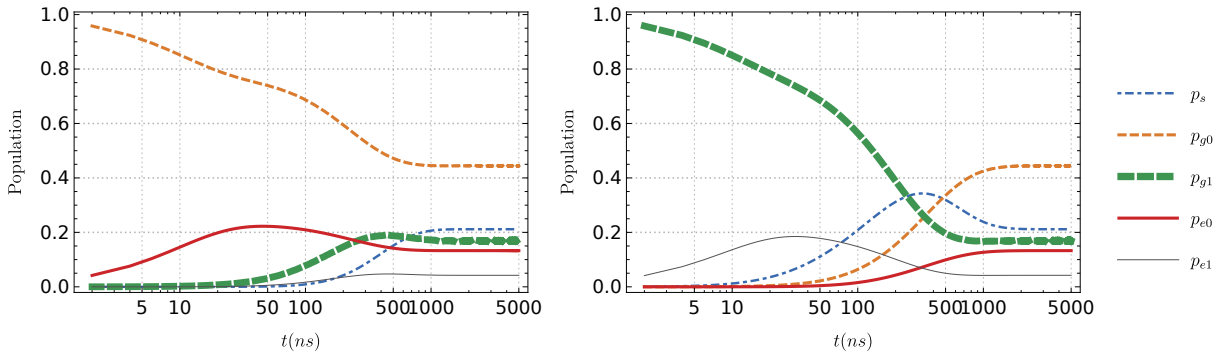

(A) Laser on and μw on, starting in p_{g0}

(B) Laser on and μw on, starting in p_{g1}

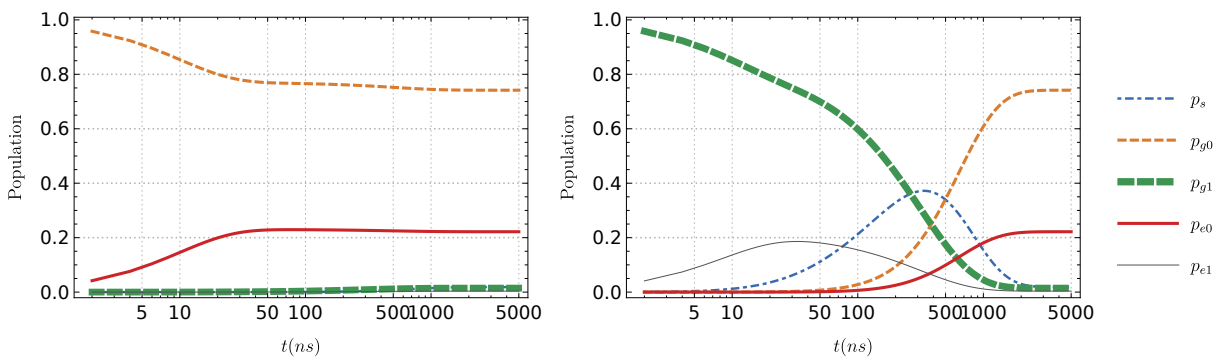

(C) Laser on and μw off, starting in p_{g0}

(D) Laser on and μw off, starting in p_{g1}

Figure 1.3: NV center dynamics with laser and microwaves on or off, starting in $|g,0\rangle\langle g,0|$ or $(|g,-\rangle\langle g,-| + |g,+\rangle\langle g,+|)/2$.
Values used here are: $\omega = \Delta_g = 2.87$ GHz, $\Delta_e = 1.4$ GHz, $\Omega = 20$ MHz, $k = 0.3$, $\gamma_{eg} = 77$ MHz, $\gamma_{es} = 30$ MHz, $\gamma_{sg} = 3.3$ MHz, $\gamma_{01} = 1.5$ MHz. Plots (A) and (C) show the evolution of $|0\rangle$ under the presence or the absence of the microwaves while (B) and (D) show the same evolution, but starting in $\frac{|-1\rangle+|+1\rangle}{\sqrt{2}}$. (A) and (B) reach the same final state while (C) and (D) also reach the same final state.

then feeds the ground state with null angular momentum, which then undergoes the same process as in case (c) and starts feeding the p_{e0} state. A quick inspection confirms that the final state of (d) is again identical to the final state of (c), as we can expect from NVs under laser excitation.

As discussed above, the steady state of an NV center will be identical regardless of the initial state, which means that any discrimination between $m_s = 0$ and $m_s = \pm 1$ must be done faster than a few microseconds. Ian Hincks covered the statistical aspect of the NV center state measurement in his thesis, which we will reproduce here, with permission of the author.

To understand measurements, we first observe that $m_s = 1$ is, on average, dimmer than $m_s = 0$, since $|e, +1\rangle$ and $|e, -1\rangle$ are likely to decay, through phononic and infrared transitions, to $|g_0\rangle$ through the singlet. We then remember that after some time, the NV center is polarized to $|g, 0\rangle$ and will emit photons with a constant rate, independent of its initial state (1.5 (b)). By consequence, counting photons after the NV is polarized will yield identical results regardless of its initial state. We thus want to count photons from the moment the laser is turned on to an optimal time t_{opt}. We then need to know how many photons to expect from the bright state and the dark state. With these two values measured precisely, a reliable collection of photons will let us measure the state of the NV center. We will label the average per-shot reference values $\bar{\alpha}(\Delta t)$ and $\bar{\beta}(\Delta t)$ for the number of photon collected when the NV center is in the bright state and in the dark state, respectively, when the counter is open for time Δt from the moment the laser is turned on. For a general experiment, we will open the counter three times, measuring three times, as depicted in figure 1.4. First we polarize the NV center with the application of the laser for a few μs. We wait a μs to let the NV center relax and the singlet state to depopulate. We then reopen the laser with the counter to take a reference of the bright state. The counter is open for some time, Δt, and the laser is left open for longer, few μs once more. Following this, we apply an adiabatic pulse to invert the population from the $m_s = 0$ to the $m_s = 1$ state and re-apply the laser and the counter to take a dark reference. The laser being applied for a few μs, the NV center is re-initialized, ready to start the experiment. We then apply the pulse sequence required by the experiment and open the counter and the laser one last time, to take a measure of the NV center state. Defining T_e to be the length of time, for a single experiment, where the counter is not open (the sum of the initialization, wait times, pulses, etc.) and N to be the number of repetitions, we can define the total duration of the experiment as $T = N(T_e + 3\Delta t)$.

Redefining $p = g_{g0}(t)$ to be the probability that the density state is found to be in the bright state, and assuming that a single experiment happens much faster than the time it takes an NV center to drift under the microscope, we can simplify the photons emitted in

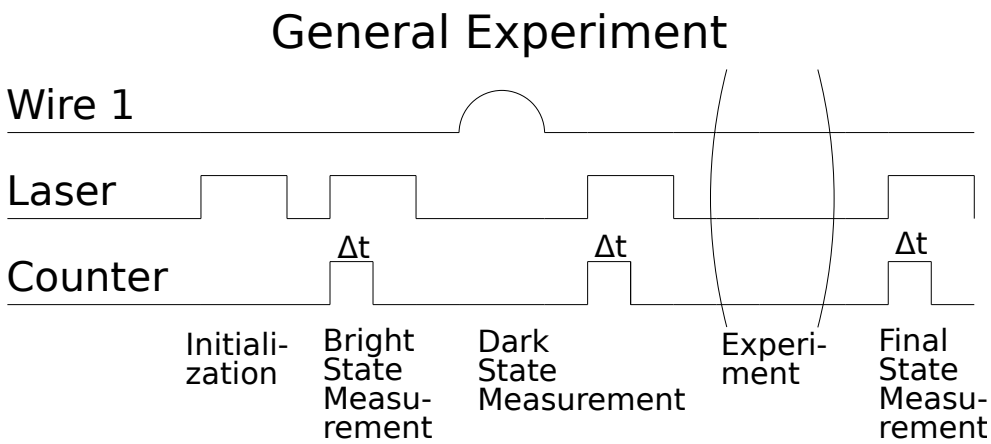

Figure 1.4: Outline of a single shot of an experiment.
During the Initialization, a laser pulse polarizes the NV center to $|0\rangle$. During the Bright State Measurement, the counter opens to measure the photons emitted by the NV center in the $|0\rangle$ state. The Dark State Measurement sees an adiabatic pulse to invert populations followed by the counter opening again to measure the photons emitted by the NV center in the $|-1\rangle$ state. The Experiment is kept general for now. During the Final State Measurement, the counter opens one last time to measure the photons emitted by the NV center in the state of interest.

the dark and bright states $\bar{\alpha}(\Delta t) = \alpha$ and $\bar{\beta}(\Delta t) = \beta$ and we will follow I. Hincks steps to approximate that the variance on p can be expressed as

$$\Delta p^2 = \frac{p(p+1)N\alpha + (p-2)(p-1)N\beta}{(N\alpha - N\beta)^2} \tag{1.22}$$

It was shown that we get the worst case when $p = 1$ and replacing values for N, we get the Cramer-Rao Bound:

$$\Delta p\sqrt{T} = \frac{\sqrt{2(T_e + 3\Delta t)\alpha(\Delta t)}}{\alpha(\Delta t) - \beta(\Delta t)} \tag{1.23}$$

Equipped with this expression to find the minimal variance of p for a given experiment, we sweep Δt until we find the minimal value of Δp. As shown in figure 1.5 (c), Δp is more sensitive to under estimating Δt than it is to over estimate it. This is important for experiments with different wait times T_e where the shorter experiments would want Δt that are too short for the longer experiments.

1.5 Rotating Wave Approximation for NV centers

In order to run simulations with frequencies on the order of a small magnetic field (about 50-100 MHz) and Rabi oscillations (about 5-20 MHz) and to avoid dealing with the ZFS term, we use a frame transformation to boost into a frame rotating by Δ around S_z^2 and then reject time dependent terms.

Neglecting nearby Carbon isotopes for simplicity, the Hamiltonian will be reduced to $H = H_{int} + H_{\vec{B}} + H_{ctrl}(t)$ where H_{int} is the internal Hamiltonian, intrinsic, $H_{\vec{B}}$ is the effect of an applied magnetic field, time independent, due, in our case, to a disk magnet positioned nearby, and $H_{ctrl}(t)$ is the control Hamiltonian due, in our case, to a nearby wire carrying a current and producing a time dependent magnetic field. Specifically, $H_{int} = \Delta S_z^2 + A_N \vec{S} \otimes \vec{I}$, where ΔS_z^2 is the Zero Field Splitting, at $\Delta \approx 2.87$ GHz and $A_N \vec{S} \otimes \vec{I}$ is the hyperfine interaction with the nearby Nitrogen nuclear spin. $H_{\vec{B}} = \gamma_e \vec{B} \cdot \vec{S}$ where $\gamma_e = 2.8$ MHz/G is the gyromagnetic ratio and $\vec{B}$ is the magnetic field at the NV center site. $H_{ctrl}(t) = \cos(\omega t + \phi)\vec{\Omega} \cdot \vec{S}$, where ω is the carrier frequency, ϕ is the phase shift and $\vec{\Omega}$ is the Rabi strength of the microwave field at the NV center site. Each of these three parameters (ω, $\vec{\Omega}$ and ϕ) are time dependent and are controlled with an Arbitrary Waveform Generator and mixed with a local oscillator.

To simplify the description of this Hamiltonian under the Rotating Frame Approximation (RWA), we will split it in two parts. The first part is going to collect the terms that

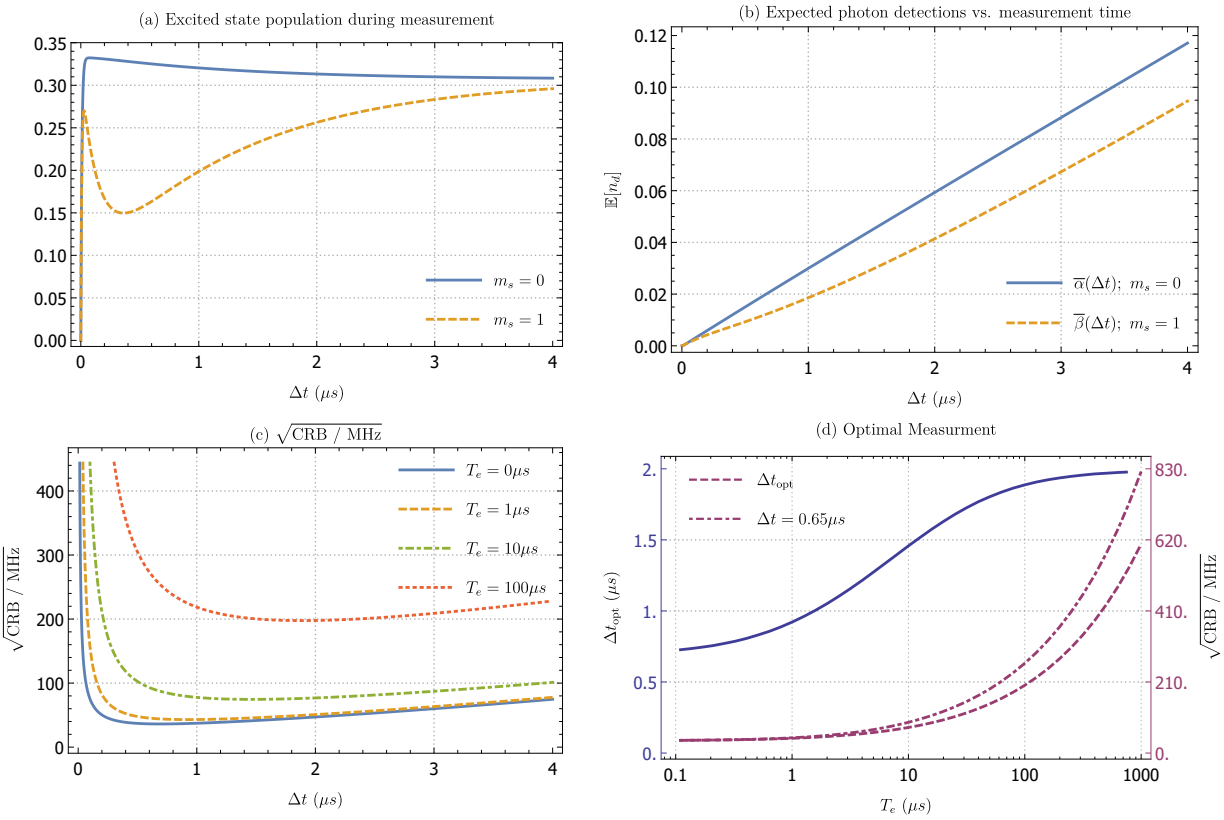

Figure 1.5: Simulated example of optimizing measurement time for a low visibility experiment.
The same analysis holds for high visibility experiments (a) The population of the optical excited state is plotted for two initial states, (b) which results in distinguishable numbers of detected photons given that we average enough repetitions. They are labeled $\alpha(\Delta t)$ and $\beta(\Delta t)$ in the main body and asymptote to the same slope since they both end up in the same steady state of the master equation. (c) These curves can be used to estimate the standard deviation of p normalized to square-root run time for various experiment lengths. For example, given $\sqrt{CRB/\text{MHz}} = 400/\sqrt{\text{MHz}}$, a total run time of 100s $= 10^8 \mu$s will approximately reduce the uncertainty of Δp to 0.04. (d) As a function of T_e, optimal measurement window length $\Delta t_{opt}$is shown (left axis) along with the corresponding $\sqrt{CRB/\text{MHz}}$ values for both the optimal measurement time, and a fixed measurement time of 0.65 μs (right axis). It is seen that in this regime the payoff of using the optimal measurement time is rather slim. [figure and caption from Ian Hincks[25]]

commute with the frame of choice: S_z^2 while the other is going to collect the terms that don't.

$$H = \Delta S_z^2 + A_{N,\parallel} S_z \otimes I_z + \gamma_e B_z S_z + \Omega_z \cos(\omega t + \phi) S_z \tag{1.24}$$
$$+ A_{N,\perp}(S_x \otimes I_x + S_y \otimes I_y) + \gamma_e (B_x S_x + B_y S_y) + \Omega_x \cos(\omega t + \phi) S_x \tag{1.25}$$

Here, we chose $\vec{\Omega}$ to be expressed in the xz plane for convenience. As a matter of fact, since the only restriction imposed by the system is to align the PAS with $\hat{z}$, we are free to define the direction of the microwave oscillations as the $\hat{x}$ direction.

To express this Hamiltonian in the rotating frame of the ZFS, we will apply the usual frame transformation, for a given operator or Hamiltonian, following from the Schrödinger equation:

$$\tilde{H} = e^{iH_0 t}(H - H_0)e^{-iH_0 t}$$

Where $H_0 = \omega S_z^2$ is the rotating frame of interest. Since S_x and S_y do not commute with S_z^2 like they would with S_z, we will take a quick look at the rotating Hamiltonian.

The first part of the Hamiltonian (1.24) will remain untouched under the frame transformation since each term commutes with S_z^2.

For the second part of the Hamiltonian (1.25), we will first observe that S_x and S_y transform like:

$$\tilde{S}_x = e^{i\omega S_z^2 t} \cdot S_x \cdot e^{-i\omega S_z^2 t} = \cos(\omega t) S_x + \sin(\omega t) S_y' \tag{1.26}$$
$$\tilde{S}_y = e^{i\omega S_z^2 t} \cdot S_y \cdot e^{-i\omega S_z^2 t} = \cos(\omega t) S_y + \sin(\omega t) S_x' \tag{1.27}$$

Using trigonometric identities to expand the modulation of the control part of the Hamiltonian and setting the modulation frequency to the one of the rotation, we get

$$\cos(\omega t + \phi) = \cos(\omega t)\cos(\phi) - \sin(\omega t)\sin(\phi) \tag{1.28}$$

By substituting 1.27 and 1.28 in the non commuting part of H (1.25), we get :

$$\begin{aligned}\tilde{H}_\perp =& A_{N,\perp}((\cos(\omega t)S_x + \sin(\omega t)S'_y) \otimes I_x + (\cos(\omega t)S_y + \sin(\omega t)S'_x) \otimes I_y) \qquad (1.29)\\ &+ \gamma_e(B_x(\cos(\omega t)S_x + \sin(\omega t)S'_y) + B_y(\cos(\omega t)S_y + \sin(\omega t)S'_x))\\ &+ \Omega_x(\cos(\omega t)\cos(\phi) - \sin(\omega t)\sin(\phi))(\cos(\omega t)S_x + \sin(\omega t)S'_y)\\ &= \cos(\omega t)(\Omega_z \cos(\phi)S_z + A_{N,\perp}(S_x \otimes I_x + S_y \otimes I_y) + \gamma_e(B_x S_x + B_y S_y)) \qquad (1.30)\\ &+ \sin(\omega t)(\Omega_z \sin(\phi)S_z + A_{N,\perp}(S'_y \otimes I_x + S'_x \otimes I_y) + \gamma_e(B_x S'_y + B_y S'_x))\\ &+ \frac{1+\cos(2\omega t)}{2}\Omega_x \cos(\phi)S_x - \frac{1-\cos(2\omega t)}{2}\Omega_x \sin(\phi)S'_y\\ &+ \frac{\sin(2\omega t)}{2}\Omega_x(\cos(\phi)S'_y - \sin(\phi)S_x)\end{aligned}$$

Using the Rotating Wave Approximation, we will only keep the time independent terms, which corresponds to integrating the Hamiltonian over a period $[0, 2\pi/\omega]$. With the re-introduction of the commuting terms, we get

$$\tilde{H} \approx A_{N,\parallel} S_z \otimes I_z + \gamma_e B_z S_z + \frac{\Omega_x}{2}(\cos(\phi)S_x - \sin(\phi)S'_y) \qquad (1.31)$$

Here, we further assume that the perpendicular magnetic fields are small compared to the axial field. For completeness, the same procedure can be followed to express the time independent part of a control in $\hat{y}$ in the rotating frame.

$$\Omega \cos(\omega t + \phi)\tilde{S}_y \approx \frac{\Omega}{2}(\cos(\phi)S_y - \sin(\phi)S'_x) \qquad (1.32)$$

1.5.1 Transverse Magnetic Field

We mentioned in the last section that the approximation was valid if the transverse magnetic field was small enough. In this section, we will explore the effect of a large transverse field by using higher orders of the Magnus expansion, using Floquets coefficients to speed up computation times. In fact, we will consider Rabi and Ramsey experiments under different approximations; by keeping the zeroth term of the Magnus expansion, keeping it and one additional term, keeping it and two additional terms or simulating the system without any approximation and small time intervals.

In the lab frame, we can neglect the hyperfine coupling with the nearby Nitrogen and the dipolar coupling with a nearby Carbon if the coupling to the microwaves is larger than each of them. The Hamiltonian will then be:

$$H = \Delta S_z^2 + \omega_x S_x + \omega_z S_z \Omega \cos(\omega t + \phi)S_x \qquad (1.33)$$

where $\omega_x = \gamma \vec{B_x}$ is the coupling to the magnetic field in the transverse plane and B_x is the magnetic field.

Using $\omega = \Delta - \omega_z$ to perform a single transition, preparing the Hamiltonian for a Ramsey experience and using 1.30 once more, we get :

$$\begin{aligned}\tilde{H} =& \cos(\omega t)\omega_x S_x + \sin(\omega t)\omega_x S'_y \\ &+ \omega_z(S_z^2 + S_z) \\ &+ \frac{1+\cos(2\omega t)}{2}\Omega_x \cos(\phi) S_x \\ &- \frac{1-\cos(2\omega t)}{2}\Omega_x \sin(\phi) S'_y \\ &+ \frac{\sin(2\omega t)}{2}\Omega_x(\cos(\phi)S'_y - \sin(\phi)S_x)\end{aligned} \tag{1.34}$$

which, in its exponential form, looks like:

$$\tilde{H} = e^{-i2\omega t}H_{-2} + e^{-i\omega t}H_{-1} + H_0 + e^{i\omega t}H_1 + e^{i2\omega t}H_2. \tag{1.35}$$

Where H_n is associated with the argument of the exponential $e^{in\omega t}$:

$$H_{-2} = \frac{\Omega_x}{4}(\cos(\phi) - \sin(\phi))(S_x + iS'_y) \tag{1.36}$$

$$H_{-1} = \frac{\omega_x}{2}(S_x + iS'_y) \tag{1.37}$$

$$H_0 = \frac{\Omega_x}{2}(\cos(\phi)S_x - \sin(\phi)S'_y) + \omega_z(S_z^2 + S_z) \tag{1.38}$$

$$H_1 = \frac{\omega_x}{2}(S_x - iS'_y) \tag{1.39}$$

$$H_2 = \frac{\Omega_x}{4}(\cos(\phi) + i\sin(\phi))(S_x - iS'_y) \tag{1.40}$$

where we recognize H_0 to also be the time independent part of the rotating Hamiltonian, the first term of the Magnus expansion.

This form of the Hamiltonian is all we need to use the Floquet coefficients approach used by Leskes et al. [29] to avoid the cumbersome and recursive formulas of the Magnus expansion.

Reproducing their results here, we have:

$$
\begin{aligned}
\overline{H}_0 =& H_0 && (1.41)\\
\overline{H}_1 =& -\frac{1}{2}\sum_{n\neq 0}\frac{[H_{-n},H_n]}{n\omega}+\sum_{n\neq 0}\frac{[H_0,H_n]}{n\omega} && (1.42)\\
\overline{H}_2 =& \frac{1}{3}\sum_{n,n'\neq 0,n\neq n'}\frac{[H_{n'},[H_{n-n'},H_{-n}]]}{n'n\omega^2}+\frac{1}{2}\sum_{n\neq 0}\frac{[H_n,[H_0,H_{-n}]]}{(n\omega)^2} && (1.43)\\
&-\frac{1}{2}\sum_{n\neq 0}\frac{[H_0,[H_0,H_n]]}{(n\omega)^2}+\sum_{n'\neq 0,n\neq 0}\frac{[H_{n'},[H_{-n'},H_n]]}{nn'\omega^2}\\
&+\frac{1}{2}\sum_{n\neq 0,n'\neq 0}\frac{[H_{n'},[H_n,H_0]]}{n'n\omega^2}\\
\overline{H}_3 =& ...
\end{aligned}
$$

Using these simpler formulas, we can simulate Rabi and Ramsey experiments with higher orders of the Magnus expansion. We will also pick values of the transverse field that are reasonable with our experience. The local magnetic field at the NV center is supplied by a bar magnet that is moved around and fitted to a model for a dipole magnet, which is used to help us predict the field that can be achieved for each NV center orientation given the limited volume the bar magnet can be placed in. In some cases, since the sample stage cannot move wider than a volume of 2.54 mm of side and the magnet cannot be placed over the sample holder itself, there are many locations (and field values) that are not accessible, meaning that it is not guaranteed that a field can be uniquely aligned with a given NV center orientation. This is why we look into the effect of the transverse field for at values.

In general, not all orientations of NV centers will be nicely placed for the magnet to produce a clean field along the PAS and we can pick the orientation that gets the best field for our experiments but in this case, since we want each microwave source to be coupled with an NV center that can be aligned with the field, we cannot choose any NV center, so we need to see how much a transverse magnetic field affects the results.

Chapter 2

Confocal Microscopy

To observe NV centers, we used a custom built confocal microscope. This custom built system was first assembled by Om Patange, who graduated in 2013. Between that time and the moment I joined the group, this setup had changed from a optical fiber detector to a free space detector and wasn't used for experiments. I thus took possession of this system and brought it back to full operation. This chapter will cover the adjustments I made on the setup, from learning how to use it to validate its performances. This section also aims to be a helpful tool for anyone that wants to learn about the operation of their confocal microscope and maintain it rather than building one from scratch. For this purpose, this chapter will be divided in several sections corresponding to different parts of the microscope. We will cover: the laser source, the switching arm, the mode shaping arm, the scanning optics, and the detector.

Label	Component	Manufacturer	Part Number
1	Laser head	Coherent Inc.	Sapphire 532-100 CW
2	Half Wave Plate	Thorlabs Inc.	WPMH05M-532
3	Blocker	Thorlabs Inc.	LB1
4	Polarising Beam Splitter	Newport Corp.	05BC16PC.3 (PBS), 9411 (mount)
5, f_1	Lens (f=175.0mm)	Thorlabs Inc.	LA1229-A
7	Acousto Optic Modulator	Isomet Corp., Newport Corp.	1250C-848 (AOM), 9071-M (mount)
7, f_2	Lens (f=1250.0mm)	Thorlabs Inc.	LA1433-A
8	Fiber coupler	Thorlabs Inc.	F240FC-A 543nm

Label	Component	Manufacturer	Part Number
9	Single Mode Fiber	Thorlabs Inc.	P1-630-FC-2
10, f_3	Lens (f=50.0mm)	Thorlabs Inc.	LA1131-A
11, f_4	Lens (f=125.0mm)	Thorlabs Inc.	LA1986-A
12	Dichroic mirror	Semrock Inc., Thorlabs Inc.	LPD01-532RS-25 (dichroic), KM100T (mount)
13	Galvanometer mirrors	Cambridge Technology	6210HM40 (scanner), 6010-29-120 (cables), 67321H-1 (driver), 6102105R20 (mirror mount), 6M2005S20F025S1 (mirrors)
14, f_5	Lens (f=150.0mm)	Thorlabs Inc.	AC254-150-A
15, f_6	Lens (f=200.0mm)	Thorlabs Inc.	AC254-200-A
16	Microscope objective	Nikon	CFI Apochromat TIRF 60XC Oil
17, f_7	Lens (f=100.0mm)	Thorlabs Inc.	AC254-100-A
18	Pinhole	Thorlabs Inc.	P5S
20	Optical table	Technical	784-436-02R (table),
19, f_8	Lens (f=50.0mm)	Thorlabs Inc.	AC254-050-A
		Manufacturing Corporation	12-41H-84 (legs)
20	Single Photon Counting Module	Excelitas Technologies Crop.	SPCM-AQRH-13 CDX

Table 2.1: List of the components of the custom built confocal microscope. Labels of this table correspond to those of figure 2.1

2.1 Laser Source

This piece of equipment generates a 532 nm green Gaussian collimated beam to excite NV centers.

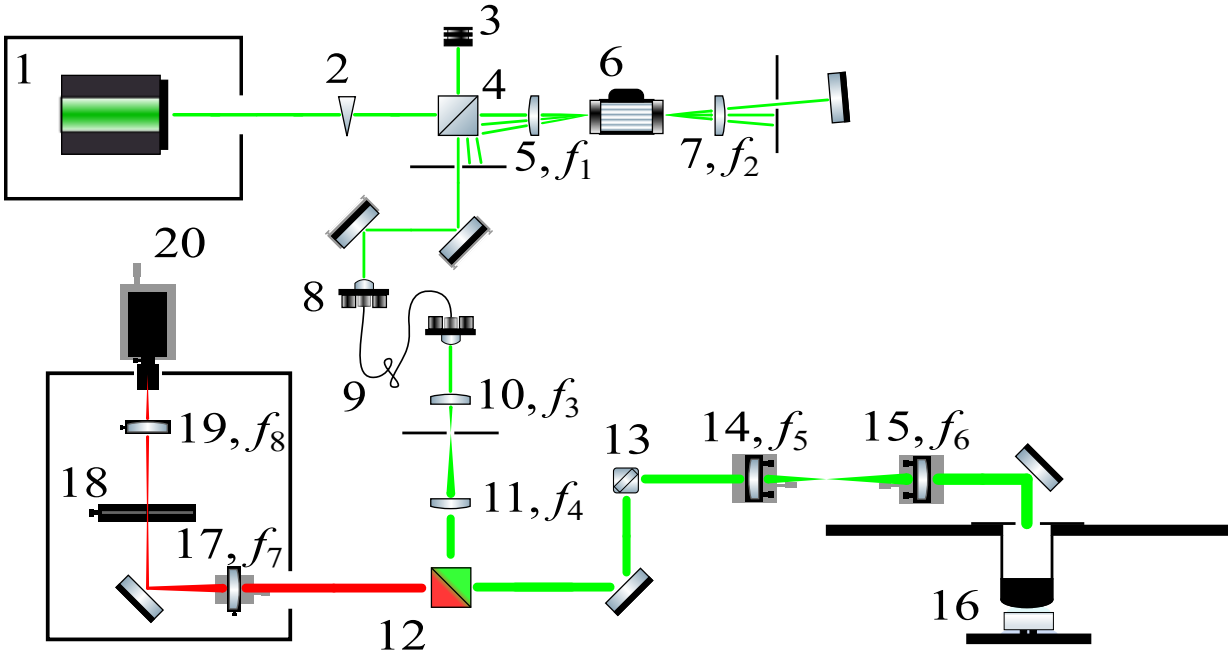

Figure 2.1: Diagram of the experimental setup. Part numbers correspond to the list in table 2

2.1.1 Description

As detailed in the previous chapter, the ground state of the NV center is 1.945 eV below its excited state (637 nm, red light) and can be excited via a meta stable state with green laser excitation, in a process similar to Raman scattering [30]. In consequence, it would be possible to excite the ground state directly to the excited state, but since it would be harder to discriminate photons coming from the excitation source or from NV centers themselves if they were of the same color, we instead excited NV centers with off-resonance, green, light.

The first part of the microscope is then a laser source that can excite NV centers with an off-resonance green laser, producing a Gaussian beam that we control and guide through the microscope with the switching arm, mode shaping arm and scanning optics.

In our microscope, we use a 532 nm (green) laser from Coherent Inc.; a Continuous Wave Sapphire laser with a nominal maximal power of 100 mW, providing a monochromatic source, with a laser beam collimated and stable in direction and power.

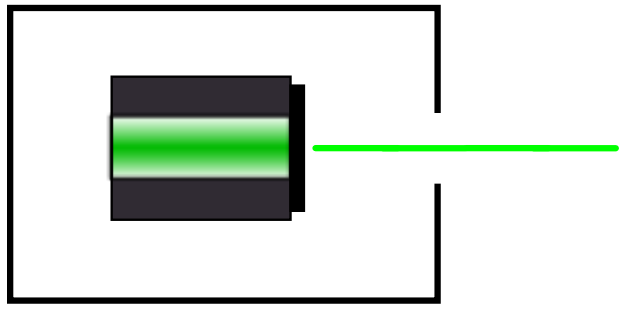

Figure 2.2: Diagram of the laser head in its enclosing, with mirrors to guide the beam outside

2.1.2 Maintenance

When I was taking ownership of the optical equipment, the laser head was outputting a maximum of 55 mW, much below the nominal power of 100 mW. Since there isn't anything to be done about it in the lab, I ordered another identical laser head [1].

There are few things to consider when we want to confirm that this component is working properly. We will cover how to evaluate the quality of the shape of the beam and measure its power stability and mention other parameters to worry about. We will begin with the shape of its cross section, which should be Gaussian, i.e. it should follow a two dimensional Gaussian distribution. For our application, the beam quality didn't need to be perfect and since we took more care in other sections of the experimental setup than with measuring and improving the quality of the beam, this measurement was simplified. However, should one decide to properly measure the quality of the beam, ISO has published standards for the calibration of a Gaussian beam [31]. See appendix A.

For the sake of simplicity we used a Charge-Couple Device (CCD) camera and a beam profiler, paired with the Thorlab software "Beam 7.0", to give us both a correlation between the current beam shape and Gaussian distribution along two axes and a measure of the ellipticity (flattening) of the beam. The correlation is computed using a line that crosses the brightest point of the beam; it uses a least square fit method to fit a Gaussian distribution to the data. This is done in x and y, given by the orientation of the detector. The ellipticity

[1] This model of laser is mounted on a heat sink, a block of metal with protruding guiding pins, four little buttons to guide the sides of the laser head, two per side. Using these guiding pins as a precise guide to put the new laser head on the same place that the previous was, we secured it down. This proved efficient to ensure that the new beam path overlapped the old beam path, requiring minimal adjustment to work efficiently. This is a result of the great care taken by the people setting up the optical table.

is the relative difference between the major and minor axis: $ellipticity : e = \frac{a-b}{a}$ with a the length of the major axis and b the length of the minor axis. For $a \approx b$, for a shape closer to a circle, the ellipticity approaches 0 and when b is close to 0, the ellipticity reaches 1. Note that a will never reach 0 first: by definition it is the longer axis. Repeated measurements of the ellipcity yielded $e = 0.1$.

As per manufacturer's specifications, the laser head should be allowed to warm up for 5 minutes before operation to maximize stability. If given that timeit is expected to have a pointing stability of less than 30 μrad, a long term power stability of less than 2%, and using the Lowest order of the Transverse Electromagnetic Mode orthogonal to the travelling wave (TEM_{00}) as the reference, a transverse beam mode quality of $M^2 < 1.1$ TEM_{00}, where M^2 is the beam quality factor and TEM_{00} is the lowest order of the Transverse Electromagnetic Mode.

To measure the long term power stability, we used a power meter to record power variations over several hours, with the thorlab software"Thorlabs Optical Power Meter Utility". With the laser lowered to about 35 mW to not saturate the power meter rated for a maximal value of 50 mW, we put the power meter just outside the box protecting the laser head and let it collect 10,000 data points, sampled every 5 seconds, measuring overnight to limit the exposure to body heat. Results are displayed in figure 2.3. This yielded an average of 34.9711 ± 0.0003 mW, with minimal and maximal values of 34.859 ± 0.001 mW and 35.102 ± 0.001 mW which are 0.4% away from the average, well within the announced 2% stability.

If the laser power, coming out of the Mode Shaping arm, is found to vary a lot (dropping by a factor of two), one can look at the spatial stability of the laser beam. This has not been an issue while we were running the current experiments but should be kept in mind.

In conclusion, to confirm that this part of the microscope is working properly, one should focus on the quality of the beam (measured with a correlation against a 2D Gaussian distribution or with the M^2 test) and on the stability of its poynting vector and its power, if the laser power is unstable at the sample stage.

2.2 Switching arm

This piece of equipment is an Acousto Optic Modulator (AOM) which is a fast acting optical switch.

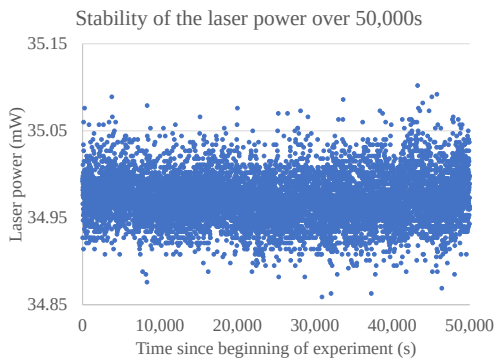

(a) Instantaneous laser power, sampled 10,000 times, once every 5 seconds

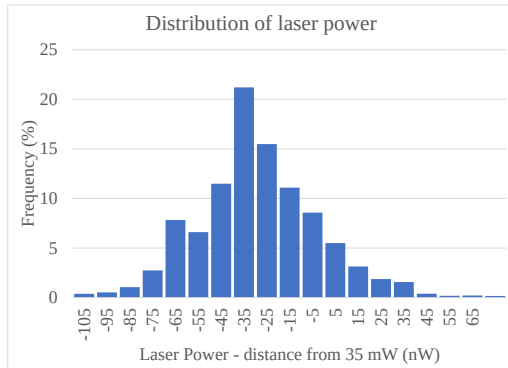

(b) Distribution of the laser power. The horizontal axis is shifted by 35mW (subtracted) for readability

Figure 2.3: Temporal stability of the laser power

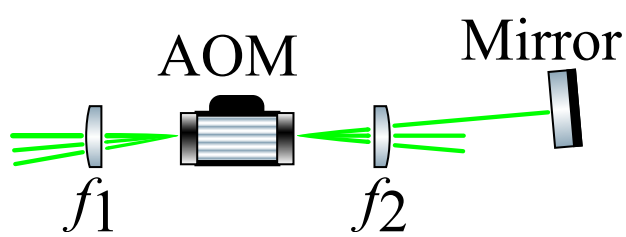

Figure 2.4: Diagram of the AOM with telescope focusing the beam onto its center point

2.2.1 Description

An AOM is a piezoelectric crystal onto which a electrical strain is imposed to change its density. Under that strain, S, the index of refraction, n, changes inversely, related by the photoelastic coefficient, p : $1/n = pS$. By putting this crystal between two electrodes, one can send a sinusoidal electric signal through the medium, which will propagate strains along that signal, compressing and stretching the crystal. This strain, in turn, will induce a sinusoidal change of index of refraction, letting this crystal behave like a diffraction grating. If the thickness of this diffraction grating is small, the AOM will behave like a thin grating, diffracting the light into multiple beams. If the grating is thick enough, the AOM will behave like a thick grating: the input beam will be diffracted with zeroth and first order only, provided it entered the crystal at the Bragg angle.

Given a grating thickness, L, an input light wavelength, λ, an acoustic velocity, v_a, an acoustic frequency, f, and an acoustic wavelength, $\Lambda = v_a/f$, the AOM will display thin grating properties if $L << \Lambda^2/\lambda$ and thick grating properties if $L >> \Lambda^2/\lambda$. Normally, the Bragg angle, θ, is given by $2d\sin\theta = \lambda/m$ where d is the distance between two lattice planes and m is a positive integer, but in this case, we need to use Λ, the distance between two peaks of acoustic maxima, giving a slightly different expression for the Bragg angle : $2\Lambda\sin\theta = \lambda/m$.

Furthermore, since the AOM isn't a simple grating but actually supports mechanical oscillations that modify the medium in which the light travels, this introduces a Doppler shift. If ω is the angular frequency of the incidental optical wave and f is the frequency of the acoustic wave, the diffracted beam will have frequency $\omega' = \omega \pm f$, with increased (decreased) frequency if the incidental optical wave is going in the same (opposite) direction as the acoustic wave.

In this setup, since the laser goes through the AOM twice, this Doppler effect will be compounded and the total frequency shift will be $2f$. However, since ω is about 564 THz (for green light at 532 nm) and $f = 200$ MHz, the shift can be neglected, especially since this green light is used to perform off-resonance excitation and does not need to be exactly at 532 nm.

When the input wave enters the modulator at the Bragg angle, the intensity of the first order diffracted beam will depend on some geometric and intrinsic factors but more importantly will be dependent on the intensity of the acoustic waves; more power goes into the first order diffraction as more power is put in the acoustic wave. As far as the geometric factors go, the diffracted beam gets weaker as the AOM aperture gets larger, or similarly, as the beam gets smaller. A larger beam will display a brighter diffracted beam but at the same time, it will increase the rise time of the device, which increases proportionally with the waist (diameter) of the beam and inversely proportionally with the acoustic velocity.

This AOM requires a beam width of 80 μm. It is then convenient to place the AOM at the focal point between two lenses. For this task, the microscope uses two lenses with focal length of $f_1 = 175$ mm and $f_2 = 150$ mm. These lenses were chosen to accommodate the previous laser that was coupled to an optical fiber at the output of the laser source and right after the switching arm. The current setup doesn't use this fiber but the lenses weren't moved to maintain the alignment of the setup. The beam is then collimated outside of this telescope, focusing the beam in the AOM. When the laser exits the AOM and the second lens, it is reflected off a flat mirror and goes back through the AOM once more, achieving the double pass.

To divert the reflected beam onto a different path, we use a Polarized Beam Splitter

(PBS) and a quarter wavelength plate through which the beam passes twice such that when the beam comes back to the PBS, it is reflected toward the rest of the setup rather than transmitting back to the laser source.

2.2.2 Maintenance

For a beam of 80μm the Tellurium Dioxide modulator from Isomet Corp. is rated to exhibit a rising time of 12 ns and a double pass efficiency of 80%, which is the ratio of light intensity going in and cmoing out of the device. Measuring the rising time with a fast photodiode and an oscilloscope gave values close to 25 ns and measuring the double pass efficiency with a power meter gave double pass efficiency of approximately 65%. These values are not ideal but given that the time scale of the detection window is slower (hundreds of ns), that we can add a delay before the counter opens to take this into account and that we need not use all the laser power, these values remain very acceptable.

In conclusion, to confirm that this part of the microscope is working properly, one should look at its double pass efficiency and its rise time, which can be checked with a power meter and a fast diode.

2.3 Mode Shaping Arm

This piece of equipment consists in an optical fiber and a telescope. The optical fiber is used to clean the spatial mode of the beam, which has gone under some distortions in the AOM. See figure 2.5 for a diagram.

2.3.1 Description

We use a Polarization Maintaining Single mode Fiber (P1-488PM-FC-2), which attenuates the higher modes of the beam, leaving it in its fundamental Gaussian mode TEM_{00}. To couple the free space beam into this optical fiber efficiently, we need to take into account its diameter and its numerical aperture, 3.4 μm and 0.12, respectively. From these model specific values and given the input width of the beam of 1.6 mm, we used a fiber coupler with a 7.86 mm focal distance. Similarly, the ouput coupler is identical, producing a beam of 1.6 mm in the TEM_{00} at the output of the fiber.

Even if we can reliably clean a beam to a width 1.6 mm, a beam with an even larger width is more resistant to far field distortions so we use two lenses as a microscope to expand

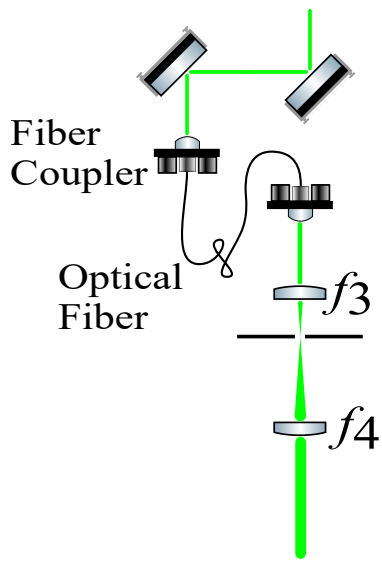

Figure 2.5: Mode Shaping Arm, with two mirrors mounted on spring loaded screws, to adjust tilt and yaw of the beam at each mirror.

the beam as much as we can while remembering that it needs to fit on the galvanometer mirrors. This is done with a telescope of two lenses of focal lengths $f_3 = 50$ mm and $f_4 = 125$ mm with a separating distance of $f_3 + f_4 = 175$ mm, widening the beam by a factor of $f_4/f_3 = 2.5$. The beam width at the output of the telescope is then 1.6 mm $\times$ 2.5 = 4 mm.

The microscope was setup to maintain the beam size with these fiber couplers but if some care is taken with it, other beam dimensions could be obtained (see Appendix B).

After the Mode Shaping Arm and right before the Scanning Optics described in the next section, we place a dichroic mirror which reflects green light perpendicular and lets red light go through. This is so that the incoming green light gets directed to the rest of the microscope objective while the red light coming from the sample gets transmitted to the detector.

2.3.2 Maintenance

There are a few steps that can be followed to establish the performance of this component of the microscope. The optical fiber could be transmitting a faint or distorted mode for few reasons. The most likely reason is that the laser is poorly coupled to the fiber. If

this happens, the laser on the output side of the fiber will be weaker than expected or completely absent. As a rule of thumb, given the specifications at each coupler and of the fiber itself, one can expect a coupling of about 0.5; the laser intensity drops by a factor of 2 by going through the fiber. In experiments where the coupling efficiency is more important, it can be brought much higher but is not crucial in our case. If the coupling falls too low (below half of the usual value), one should look at walking the beam until the beam is pointing at the fiber coupler with the right orientation. This involves 4 degrees of freedom (position in x and y, tilt and yaw), which are controlled by the tilt and yaw of a pair of mirrors. Tilting both mirrors so that they remain parallel will translate the beam while tilting them in opposite directions will rotate the beam. To perform this maintenance operation, we place a power meter at the output of the optical fiber and keep in mind that someone already spent a great deal of effort to align the beam, so moving one mirror a little bit will usually help a lot, it remains to find which mirror is misaligned.

Once the beam is aligned, dirt at the output of the fiber or its coupler can produce several modes, negating the advantage of the optical fiber in the first place. If the beam is closer to a Gaussian beam before the optical fiber rather than after, a fiber inspection scope will help tell if either end of the fiber is dirty by magnifying the head of the fiber, a clean fiber will not have any dirty spots or scratches. The core will still be visible. If the fiber is dirty, it can be cleaned with a cassette type cleaner and if the fiber is scratched, it might be better to replace the fiber entirely if the output mode is not satisfying. Finally, the connection to the coupler itself can still be faulty, mainly if the fiber is not screwed in properly or if the thread is stripped.

For the completion of this degree, I have adjusted the telescope lenses to collimate the output beam, I adjusted the coupling of the fiber several times, cleaned the dirty end of the fiber and confirmed the choice of fiber couplers for the given beam radius and fiber characteristics.

In conclusion, to confirm that this part of the microscope is working properly, one should worry about the size, power and quality of the beam after the fiber coupler as well as at the ouput of the telescope.

2.4 Scanning Optics

.

This piece of equipment is made of a set of mirrors mounted on galvanometers and a telescope.

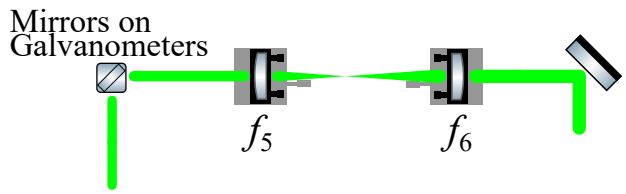

Figure 2.6: Scanning optics. Note that the last mirror (leftmost) deflects the beam downward (into the page), whereas we show it here remaining in the page for clarity.

2.4.1 Description

The galvanometers act as support for two mirrors. Voltage applied to them changes the relative angles of the mirrors by as little as 8 μrad, allowing for control of the direction of the beam for as much as 40° in each direction.

This part of the microscope prepares the beam for it to enter the objective. To make sure that the objective focuses the laser to its smallest width, the beam going into the objective must have a width as large as possible, overfilling its back. To achieve this, we use a pair of bi-convex lenses of focal length 150 mm and 200 mm that produces a magnification of $f_6/f_5 = 4/3$, when placed $f_5 + f_6 = 350$ mm apart. Since the laser beam was 4 mm before entering this telescope, it will have a width of $16/3 \approx 5.3$ mm. Overfilling the back of the objective adds the benefit of allowing some leeway in the beam position.

The galvanometers are at 150 mm from the first lens, and the second lens is also 200 mm from the back of the objective, so that these two points are conjugated and that moving the galvanometers only changes the angle at which the beam hits the microscope and not the position.

2.4.2 Maintenance

Starting from the dichroic mirror, each lens used later is going to be in the return path of the photons emitted by the sample. After reflection or fluorescence, the light comes back through the objective and the lenses, converging eventually onto a pinhole, which acts as a spatial filter, blocking photons coming from somewhere else than the sample. Photons emitted by the sample are converging through this pinhole. If any lens is misaligned, the beam will converge somewhere else in front or behind the plane of the pinhole. One can compute the width of the beam at the pinhole, which also relates to how much light goes through it, given by the formula of the power of a Gaussian beam going through an

aperture: $P(r,z) = P_0\left[1 - e^{-2r^2/\omega^2(z)}\right]$ where P is the power passing through a circle of radius r in the transverse plane at position z, where $\omega(z)$ is the width of the beam at position z and where $P_0 = 1/2\pi I_0\omega_0^2$ is the total power transmitted by the beam, with I_0 the total intensity and ω_0 the minimum beam waist.

With that in mind; the distance between each lens and their focal length known, we can track the width of the beam at the pinhole as each lens gets misaligned. Moving each lens one at a time to simplify the analysis gives us figure 2.7. From the graph and the

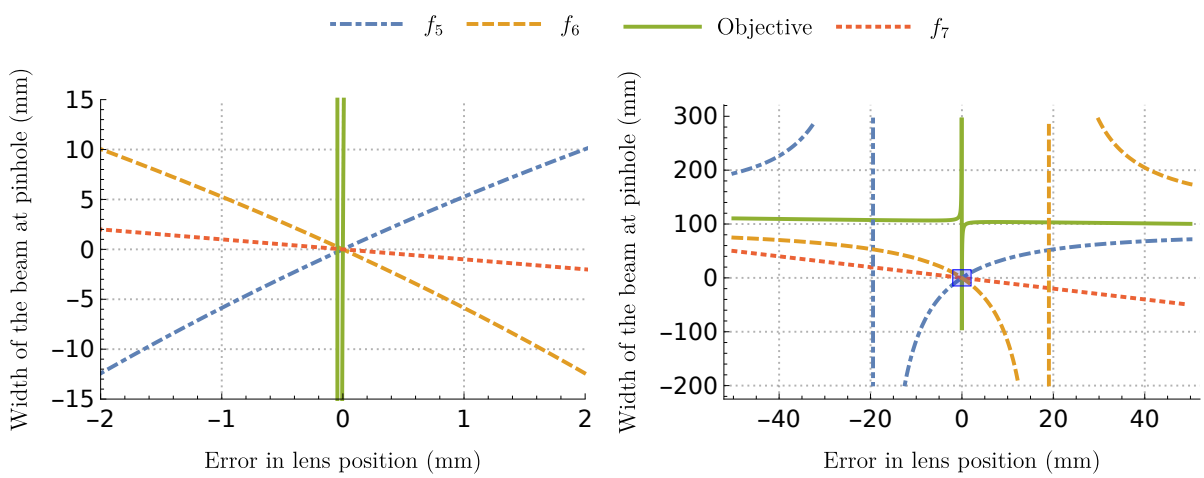

(a) Over a short range of motion.

(b) Over a longer range of motion.

Figure 2.7: Evolution of the beam width at the pinhole as a function of the displacement of one lens at a time. Rectangle on 2.7b shows the domain and image chosen for the graph on the left.

simulations, we can estimate the effect that misalignment of each lens can generate.

The last lens (f_7), closest to the detector, has a small impact on the width. This width changes linearly as the lens moves around. This is easy to picture; a beam collimated going through a single lens will focus down to a single point at the focal distance, moving with the lens.

The two lenses of the telescope (f_5 and f_6) display almost symmetric inverse functions that diverge as they move away from each other. If f_5 moves too close to the galvanometer or f_6 too close to microscope objective, by about 20 mm (see fig. 2.7b), the beam will be too large to meaningfully pass through the pinhole. Given that these lenses are mounted

on a translation stage that has a range of motion of one inch, these values are not to be underestimated and it is safer to keep the lenses closer together.

Finally, the position of the microscope objective itself is crucial. Its influence on the width of the beam through the pinhole is one of an inverse function of its position, which crosses the origin and diverges ≈ 0.05 mm from its optimal position, 350 mm from the galvanometer mirrors. Since the position of this objective is fixed, screwed on the table and at a fixed distance from the galvanometer mirrors, it looks like its very sensitive positioning can't be achieved but we cannot forget that these calculations apply for a point that is fixed on the sample; another plane of the sample will come in focus if the microscope objective is misplaced and the photons emitted by the sample will then be colimated as they come out of the objective, satisfying almost all conditions for the confocal microscope except for the fact that the galvanometers and the microscope objective are not conjugated anymore.

Although it seems like the optimal position is impossible to achieve, with each lens requiring precise positioning, the lenses do work together, such that that re-aligning one lens allows us to undo the misalignment that the previous lens introduced.

We became aware that the lenses used in the section of the microscope were sub-optimal in the sense that their coating was designed to be transparent to light in the wavelength of 650 - 1050 nm, excellent for the collected (red) light, but not for incoming (green) light. With great care to make sure that nothing else would change, we replaced these lenses for lenses identical in all points except for their Anti-Reflective coating, which we chose to be in the whole visible spectrum, 400 - 700 nm.

2.5 Microscope Objective

This piece of equipment focuses the collimated light that is aimed at it into a focal point. Since the diamond has a large index of refraction ($\approx$ 2.4), we use a oil immersion lens, with higher index of refraction than air, such that more light exits the diamond rather than being reflected internally. In consequence, it is placed vertically, with the sample holder underneath, so that the optical oil sits nicely between the objective and the sample and does not smear.

2.5.1 Description

With its idex of refraction of $n = 1.3$, oil is used to keep the index of refraction similar between the microscope objective and the diamond instead of letting the laser transmit

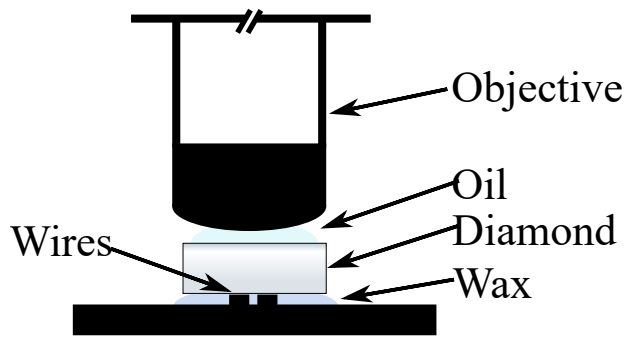

Figure 2.8: Microscope objective sitting on the sample.

from glass ($n \approx 1.4$ in the microscope objective) to air ($n = 1$ above the sample) to diamond ($n = 2.4$ in the sample itself). The direction with which the beam enters the back of the objective is also the direction that the beam will follow once focused. This is why the galvanometer mirrors and the back of the objective are placed at conjugated points, such that tilting the galvanometer mirrors lets us move the focal point inside the diamond. To compute the minimal spot size of the beam, one shouldn't simply reduce the input beam radius via magnification. What we are looking at here is the minimal radius of the beam, which can't be arbitrarily small, remaining consistent with the uncertainty principle. Similarly, the beam will not converge to a point like lens optics would tell. A beam that has well defined columnation, a well defined direction and momentum in the radial direction must sustain some uncertainty in its position on the same direction. Hence, if the beam is perfectly aimed to focus on a single point, it will reach a limit in the definition of its position, reaching a lower bound on its waist.

In fact, for a microscope objective whose back aperture is filled, one can compute the minimal radius of a Gaussian beam with its wavelength and its angular spread. Namely, we will use the formula for the half angle of a Gaussian beam in far field: $\theta = \frac{\lambda}{\pi\omega_0}$ Where θ is the half angle of divergence of the beam, $\lambda = 532$ nm is the wavelength of the monochromatic laser and ω_0 is the minimal waist (radius) of the beam, that we will identify. Instead of measuring the half angle of the microscope objective and since its numerical aperture is known, we will use the definition of the Numerical Aperture to compute the minimal waist. Using $NA = n \sin\theta$, with $NA = 1.49$, the numerical aperture of the microscope objective and $n = 2.41$, the index of refraction of the diamond containing the NV center, we can compute the beam diameter

$$d = 2\omega_0 = 2\frac{\lambda}{\pi \arcsin \frac{NA}{n}} = 508 \text{ nm}$$

We can then quickly calculate the light intensity at that spot, given that the incoming beam carries 2 mW of power for a beam of diameter d =5 mm after going through the rest of the microscope. This gives an initial power density of $P_0 = 1.02 \times 10^{-2}$ W/cm^2 concentrated to a power density of $P_1 = 9.86 \times 10^5$ W/cm^2.

2.5.2 Maintenance

The microscope objective is the hardest part of the microscope to troubleshoot and repair, if required. As part of this degree, the only inspection that I performed on this component was to estimate its quality by observing that the Gaussian collimated beam would go through the objective and would reflect on a mirror surface to give a distorted reflection of concentric rings.

To describe what happens there, let's remember that the working distance is the distance between the front end of the lens and the focal plane, where we want to place our NV centers, at the minimal beam waist. To find this focal plane, we need something much brighter than an NV center, it can be the surface of the diamond or a mirror, which can be used for calibration. When the mirror is at the working distance, the reflection off of it is inverted and follows the same path back, producing a collimated beam from the back of the microscope objective. However, if the mirror is slightly above or below the focal plane, then the reflected beam out of the back of the objective will not be collimated; it will be converging if the mirror is too high (closer to the microscope objective) or diverging if too low. Hence, using another thumbscrew mounted parallel to the motor stepper, we manually bring the sample too high (closer to the microscope objective) to produce a reflected beam that looks like a very large set of concentric rings. Moving the sample lower will shrink the reflection to a point which then expands to another set of concentric rings as the beam goes from diverging to collimated to converging, as the inverted image still is a set of concentric rings. With that in mind, we want the beam to look like a point to get a collimated beam. This should be taken with a grain of salt; since the incoming, collimated beam is 5 mm wide, aiming for the reflected beam to be converging down to a point will not provide us with an identical beam; it will be slightly converging. As long as this is systematically observed, this simply means that the plane of focus is slightly lower than the plane of reflection. This beam convergence is taken care of more easily later with lenses in the detector than it would be to take excessive care when moving the sample stage to ensure the beam is truly collimated. An example for the reflected beam when the sample (or mirror) is placed too far, at the right position or too close is displayed in figure 2.9

Since we expect the reflected light to also display a Gaussian mode (with far field distortion), observing an image that is different from Newton's rings when the incoming

beam is indeed Gaussian is the main sign that the microscope objective is defective. These Newton's rings are an interference pattern in the shape of concentric rings that are produced when light reflects between two surfaces, a spherical one adjacent to a flat one, as it is the case with the microscope near the diamond, which are approximately a spherical and planar surface, respectively. When the original setup produced distorted rings, we promptly changed the objective for another one already available, which then produced the expected Newton's rings, while changing the magnification and numerical aperture (these new magnification of 60x and numerical aperture of 1.49 are used in this work).

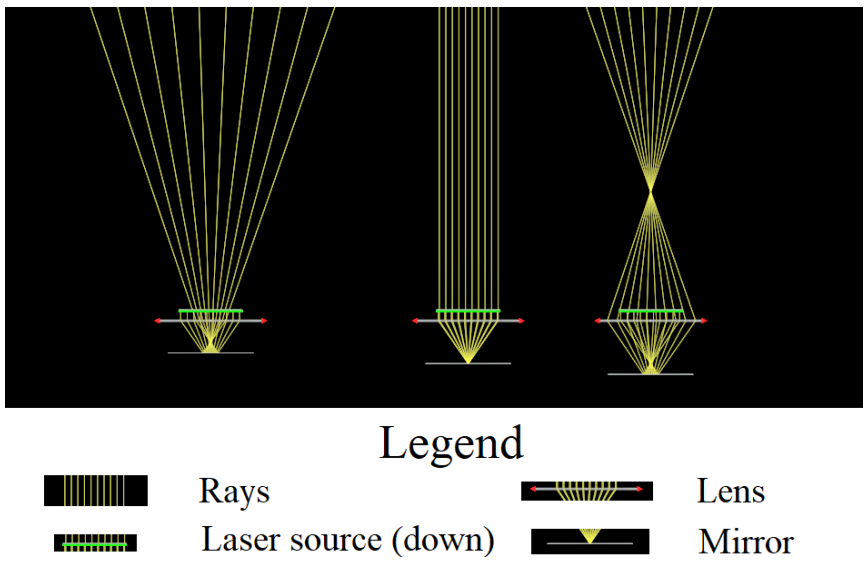

Figure 2.9: From left to right, reflected pattern when the sample (mirror) is too high, at the right height or too low.

2.6 Detector

This piece of equipment collects photons in order to measure the state of NV centers. After the green light has been guided to the NV center of interest, it fluoresces and emits red light, which is guided back towards the detector.

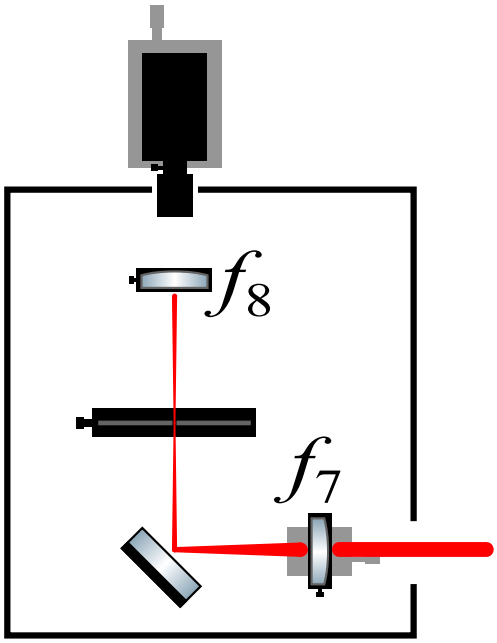

Figure 2.10: Avalanche Photodiode collecting light coming through the pinhole.

2.6.1 Description

The detector is the last part of the microscope, set after the dichroic mirror, once the green light has been filtered. The collimated red light goes through a lens that focuses it on the pinhole, goes trough another lens to focus it again and hits the single photon detector, which has a 180 μm diameter active area.

We are using an Avalanche Photo Diode (APD) as our photon counter. APDs have a series of semi-conductor layers. In the π-layer, the absorption region, the absorption of photons generates pairs of electrons-holes, which each drift in opposite directions under a small electric field, toward the n^+-layer or the p^+-layer, respectively. Before reaching the n^+-layer, electrons reach the p-layer, the avalanche region. In the avalanche region, the field is much stronger, accelerating the electrons until they reach sufficient energy to excite an electron across the bandgap, generating secondary carriers. These new pairs of electrons-holes are also accelerated, each producing additional excitation, leading to the avalanche of impact ionization processes. This amplification of the initial electron is what develops the photo-current.

Before reaching the detector itself, there are 5 elements that need to be aligned to direct as much light as possible to the detector while blocking stray light coming from the rest

of the apparatus and other light sources in the dark laboratory. The first lens has a focal length of $f_7 = 100$ mm to concentrated the collimated beam onto the pinhole, which is 5 μm wide, 200 mm further. Because of spacing concerns, the beam has to be redirected 90 degrees to the right, which complicates the alignment. The second lens has a focal length of F_8 =50 mm and is placed that far behind the pinhole, also 50 mm from the detector.

2.6.2 Maintenance

The detector can easily be misaligned, along the beam or perpendicular to it, as the first lens must aim its focal spot on a 5 μm pinhole.

When the detector is vastly misaligned, one should work with samples of large size first before moving onto smaller calibration samples until an NV center can be observed and used to perform the last adjustments. Here is the list of samples we used: a flat mirror, the gold calibration sample, micro beads and NV centers. The gold calibration sample has two components. The first one is a thin layer of fluorescent beads, few micrometers away from each other, randomly distributed. The other one is a grid just above the beads. At each crossing of the grid are a pair of numbers acting as coordinates. These crossings and numbers provide us with sharp edges to estimate the precision of the detector. The micro beads are the TetraSpeck Fluorescent Microspheres Size Kit, a microscope slice with 4 samples of beads which diameter range from 4 μm to 0.1 μm. Each bead is dyed with blue, green, orange and dark red colors.

In the beginning, for the coarse calibration step, a simple mirror was placed under the microscope objective to redirect as much light as possible to the detector. To make sure the mirror is placed at the right depth of field, we observed the reflected image and moved the mirror to the position where the image was a point, as opposed to rings, as explained previously. At that point, we placed a source of light behind the pinhole and move the pinhole in $\hat{x}$ and $\hat{y}$ until the forward propagating and backward propagating beams were on top of each other. Using the convention that $\hat{z}$ is the direction in which the beam propagates, $\hat{x}$ will be the direction perpendicular to the beam, parallel to the table, while $\hat{y}$ is perpendicular to the beam and upward. Once this is done or if there already is light going through the pinhole, we need to confirm that the beam goes through the pinhole on its waist. For this step, since the first lens has a z micro-metric screw, we can move the lens around until we get the maximum amount of the beam through. As such, we can systematically move the screw and record the amount of light going through the pinhole until the maximum is found. Since it is likely that the beam is not perfectly aligned with the screw, moving the lens back and forth introduces a bit of lateral motion, which needs

to be corrected before the transmitted light is recorded. Furthermore, since the pinhole is most likely already aligned with the rest of the detector, it is wiser to move the lens laterally rather than the pinhole. Finally, before moving on to a more detailed calibration sample, we made sure that the detector received some light by moving it laterally since it wasn't receiving any light yet. Once there is light to the detector, the first half of the battle is won, we simply need to improve the precision of the detector.

The next calibration sample is the gold grid.

While the illuminated point on the sample is as close to the edge as possible, we carefully move each component of the detector until we find the placement that lets the most light reach the detector, which we observe with real time measurements with the detector itself. The order in which these parts are adjusted is the one in which they were placed when the microscope was assembled, which corresponds to parts with increasing sensitivity. This is the optimization routine. We begin with the detector, moving it in the $\hat{x}$ direction, followed by the detector lens (right before the detector), which we move along the same direction. We then move them together, in $\hat{y}$ this time. We next adjust the pinhole lens in one direction and come back to the detector lens as we make adjustments, after which we align the other direction, with the same steps. Finally, we move the pinhole itself in both directions, very carefully since it is the most sensitive part of the detector.

At the end of a round of alignment, we do an optical scan to confirm that we are still sitting on the edge, and that the sample hasn't moved much. We iterate the alignment process, until improvements get marginal.

For the next step, it is useful to imagine that the detector is a light source and that its light goes through the optics and the telescope like the laser source does and converges at the same point that the laser source does, keeping in mind that the focal point is not a point but rather a Point Spread Function, a volume in the shape of a droplet. The procedure of alignment is then aiming at placing the two volumes at the same place, the excitation volume being the one where the laser converges and the detection volume being the one where the detector "converges".

For the first sample, we used a reflective sample, meaning that the input light and the reflected light were green. To make sure that the two paths are still aligned and superimposed when we will be using NV centers which emit in the red, we repeat the alignment process with the Microspheres, which are fluorescent, absorbing green and emitting red.

As we faced the case that the two volumes were not overlapping, we arranged an additional red laser to act as incident beam. We chose a red diode laser and simply sent it through a telescope to expand its beam waist to that of the green laser before the galvanometers. We used a pair of mirrors to move it and tilt it until it was concentric and

superimposed with the green laser. For this purpose, we used a partially reflecting silver coated film that reflects and transmits about half of the light going through. Since this device is in the path of the input and reflected beam, we lose a factor of 4 in the number of photons collected, which is not crucial at this step of calibration. Furthermore, since the filters of the detectors are set to block green light and let red light go through, it is important to introduce additional filters blocking out the red laser to make sure that not too many photons reach the detector, to save it from burning. A safe upper bound of photons per second is 30×10^6 ph/s. At that point, it will become apparent if the volume observed is the same as the excited volume. Observing a micro sphere under each laser source, one at a time, we could see that they were in very close proximity one from the other, less than 0.1 μm, which is more than enough to see NV centers, given that they show up with a width of about 1 μm under optical inspection. The resolution we reach there is limited by the pinhole, which is 5 μm wide, setting the scale of the resolution before we reach the wavelength limit.

Chapter 3

Characterization of two microwave sources, theory and experiments

In this chapter, we will cover the multiple experiments we conducted to characterize our microwave sources as well as highlighting the weaknesses of our approach, the steps we took to overcome them and the tools we will need in the future.

Simply put, characterizing our microwave sources boils down to measuring the relative amplitude as seen by an NV center due to its location and orientation relative to the wires.

The relative amplitude can be measured absolutely by performing Rabi experiments with each of the wires. We will begin by showcasing the different frequencies this experiment generates under different conditions, with a single or two microwave sources, targeting one of both transitions as well as using a large or no field.

The relative phase needs to be measured with some pulsed experiment, we will present two of those, which we performed, each with different advantages. We will describe them and since we did them in presence of a magnetic field, we will extrapolate the results we would expect at low field.

3.1 Transitions available under different conditions and their Rabi frequencies

In this section, we will present the Rabi frequencies we can expect to obtain in order to generate transitions from $|0\rangle$ to another ($|-1\rangle$ or $|1\rangle$) or both levels ($\frac{|-1\rangle+|+1\rangle}{\sqrt{2}}$) at once,

in the presence or absence of a magnetic field. Unless necessary, we will assume a single microwave source. This will be used to explain the frequency increase we obtain with two microwave sources instead of one.

3.1.1 High field

Under the influence of a magnetic field along the principal axis system $\vec{B} = (0, 0, B_z)$, the electronic internal Hamiltonian, with no microwave control, will be $H_0 = \Delta S_z^2 + \gamma B_z S_z$ where Δ is the strength of the zero field splitting, 2.87 GHz, γ is the gyro-magnetic ratio for the NV center and B_z is the magnetic field parallel to the PAS, giving the Zeeman splitting: $\omega_z = \gamma B_z$.

Single transition

First, let's consider the transition from $|0\rangle$ to a single level, say to $|1\rangle$.

In this case we have $H_0 = \Delta S_z^2 + \omega_z S_z$, the control Hamiltonian will be $H_{ctrl} = \sqrt{2}\Omega \cos(\omega t) S_x$ where we choose the amplitude $\sqrt{2}\Omega$ to simplify the analysis later while setting $\omega = \Delta - \omega_z$.

Applying a frame transformation about $H_{rot} = (\Delta - \omega) S_z^2$, we get

$$\begin{aligned}
H_0 + H_{ctrl} &= \Delta S_z^2 + \omega_z S_z + \sqrt{2}\Omega \cos((\Delta - \omega)t) S_x \\
\tilde{H} &= e^{i(\Delta-\omega)S_z^2 t}(H_0 + H_{ctrl} - (\Delta - \omega)S_z^2)e^{-i(\Delta-\omega)S_z^2 t} \\
&= \omega_z S_z^2 + \omega_z S_z + \sqrt{2}\Omega \cos((\Delta - \omega)t)[cos((\Delta - \omega)t)S_x - \sin((\Delta - \omega)t)S_y] \\
&\approx \omega_z S_z^2 + \omega_z S_z + \frac{\Omega}{\sqrt{2}} S_x
\end{aligned}$$

Where the last lines neglects the fast oscillating terms.

Writing down this new Hamiltonian in matrix form, we will use the qubit approximation to study the transition from $|0\rangle$ to $|-1\rangle$ and $|0\rangle$ to $|+1\rangle$ individually. This approximation comes from the observation that the three-by-three matrix can be seen as two two-by-two matrices sharing the central entry, while neglecting the anti-diagonal elements, since they

are null. With $\mathbb{0}_1$, the zero matrix of dimension 1, we get:

$$\begin{pmatrix} 2\omega_z & \frac{\Omega}{2} & 0 \\ \frac{\Omega}{2} & 0 & \frac{\Omega}{2} \\ 0 & \frac{\Omega}{2} & 0 \end{pmatrix} = \begin{pmatrix} 2\omega_z & \frac{\Omega}{2} \\ \frac{\Omega}{2} & 0 \end{pmatrix} \oplus \mathbb{0}_1 + \mathbb{0}_1 \oplus \frac{\Omega}{2}\sigma_x$$
$$= (\omega_z(\sigma_z + \mathbb{1}_1) + \frac{\Omega}{2}\sigma_x) \oplus \mathbb{0}_1 + \mathbb{0}_1 \oplus \frac{\Omega}{2}\sigma_x$$

In the regime where $\omega_z >> \frac{\Omega}{2}$, the first term becomes off resonance, can be approximated as $\omega_z\sigma_z \oplus \mathbb{1}_2$ and only generates a rotation along the $\hat{z}$ axis $\omega_1\sigma_z$. The second term generates a spin flip $\frac{\Omega}{2}\sigma_x$.

Measuring the state after this experiment, we get:

$$P(t) = \left| \langle 0| \, e^{-i((\omega(\sigma_z+\mathbb{1}_1)+\frac{\Omega}{2}\sigma_x)\oplus\mathbb{0}_1+\mathbb{0}_1\oplus\frac{\Omega}{2}\sigma_x)t} \, |0\rangle \right|^2 \tag{3.1}$$
$$\approx \left| \langle 0| \, e^{-i((\omega(\sigma_z+\mathbb{1}_1))\oplus\mathbb{0}_1+\mathbb{0}_1\oplus\frac{\Omega}{2}\sigma_x)t} \, |0\rangle \right|^2 \tag{3.2}$$
$$= \frac{1+\cos(\Omega t)}{2}$$

To justify the approximation made here, we will consider the situation we can safely expect to be found in our experiments and simulate the difference that applying the approximation makes. Using values for the Zeeman splitting of 100 MHz, a Rabi strength of 6 MHz and a maximal pulse duration of $1.2\mu s$, we can take the difference in $P(t)$ with and without the approximation (subtracting the right side of 3.1 from 3.2). Over $1.2\mu s$, the largest difference will be less than 0.001, a relative difference of 0.1%, as seen in figure 3.1. Comparing these values to the noise we get experimentally, we can justify the approximation.

Double transition

First, let's consider the transition to both levels. For that purpose, the control Hamiltonian will be generated with a microwave pulse and is expressed along $\vec{x}$: $H_{ctrl} = \sqrt{2}\Omega(t)\cos(\omega_1 t)\cos(\omega_2 t)S_x$, where ω_1 and ω_2 are the carrier frequencies and $\Omega(t)$ is the envelope amplitude. The two carrier frequencies will be useful for the two frame transformations; for the Zero Field Splitting term and the Zeeman splitting term.

Under the RWA, with $\omega_1 = \Delta$, the effective Hamiltonian then becomes

$$H_0 + H_{ctrl} = \Delta S_z^2 + \omega_z S_z + \sqrt{2}\Omega(t)\cos(\Delta t)\cos(\omega_2 t)S_x \tag{3.3}$$

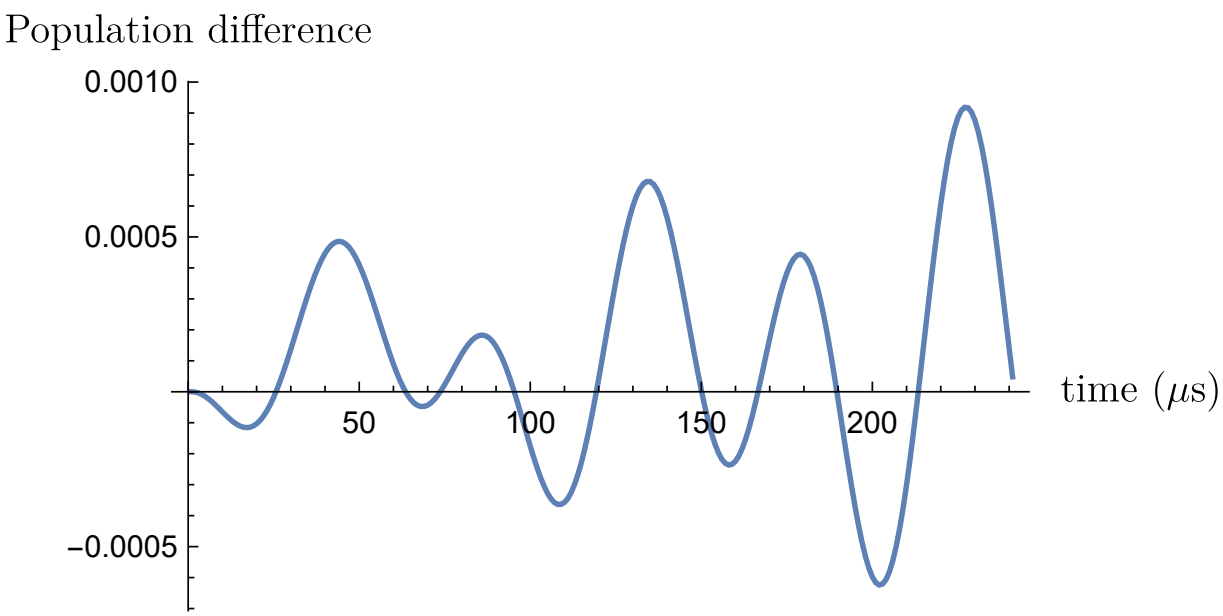

Figure 3.1: Difference in population ($P(t)$) if the qubit approximation is made or not, in 100 MHz magnetic field, with Rabi Frequency of 6 MHz

and

$$\begin{aligned}\tilde{H}_1 &= e^{i\Delta S_z^2 t}(H_0 + H_{ctrl} - \Delta S_z^2)e^{-i\Delta S_z^2 t} \\ &= \omega_z S_z + \sqrt{2}\Omega[\cos^2(\Delta t)\cos(\omega_2 t)S_x + \cos(\Delta t)\sin(\Delta t)\cos(\omega_2 t)S_y'] \\ &\approx \omega_z S_z + \Omega\frac{\cos(\omega_2 t)}{\sqrt{2}}S_x \end{aligned} \tag{3.4}$$

At this point, to suppress the Zeeman interaction term, we can apply another frame transformation and jump to the $\omega_z S_z$ frame, setting $\omega_2 = \omega_z$:

$$\begin{aligned}\tilde{H}_2 &= e^{i\omega_z S_z t}(\tilde{H}_1 - \omega_z S_z)e^{-i\omega_z S_z t} \\ &= \Omega\frac{\cos(\omega_z t)}{\sqrt{2}}[cos(\omega_z t)S_x - \sin(\omega_z t)S_y] \\ &\approx \frac{\Omega}{2\sqrt{2}}S_x \end{aligned} \tag{3.5}$$

Measuring the state after this experiment, we can find the frequency at which $|0\rangle$ is depopulated towards $\frac{|+1\rangle+|-1\rangle}{\sqrt{2}}$:

$$\begin{aligned} P(t) &= \left|\langle 0| \, e^{-i\frac{\Omega}{2\sqrt{2}}S_x t} \, |0\rangle\right|^2 \\ &= \frac{1+\cos\left(\frac{\Omega}{\sqrt{2}}t\right)}{2} \end{aligned}$$

3.1.2 No field

For this section, we will look at the control we need to perform single and double transitions when there is no magnetic field.

Single transition

This case is different from the single transition with a field for two reasons. First, we loose the $\omega_z S_z$ term in the Hamiltonian, which was necessary to suppress the undesirable transition. Second, and to alleviate this, we introduce a second degree of control. We will assume again that the first microwave source is along $\hat{x}$, by definition, while the other is along $\hat{y}$, with independant amplitude and phase. The control Hamiltonian then looks like

$$H_{ctrl} = H^1_{ctrl} + H^2_{ctrl} \tag{3.6}$$

$$= \sqrt{2}\Omega_1 \cos(\omega_1 t + \phi_1) S_x + \sqrt{2}\Omega_2 \cos(\omega_2 t + \phi_2) S_y \tag{3.7}$$

As previously, setting the modulation frequency to the one of the Zero Field Splitting and moving to its rotating frame will suppress the largest term of the system (ΔS_z^2), while we can neglect the counter rotating wave. Thus, we set $\omega_1 = \omega_2 = \Delta$

Again, as described in section 1.2, $S'_y = i[S_z^2, S_x]$ and similarly, $S'_x = i[S_z^2, S_y]$. In the rotating frame, the control Hamiltonian is expressed as :

$$\tilde{H}_{ctrl} = \frac{\Omega_1 \cos(\phi_1)}{\sqrt{2}} S_x - \frac{\Omega_1 \sin(\phi_1)}{\sqrt{2}} S'_y + \frac{\Omega_2 \cos(\phi_2)}{\sqrt{2}} S_y - \frac{\Omega_2 \sin(\phi_2)}{\sqrt{2}} S'_x \tag{3.8}$$

This will give us access to four operators that trigger a Quantum Transition between $|0\rangle$ and either $|-1\rangle$ or $|+1\rangle$ in the rotating frame: S_x, S_y, S'_x and S'_y. For a better grasp of

the level transitions these operators produce, we will use a change of basis and use angular momentum specific operators:

$$
\begin{aligned}
S_x^+ &= \frac{S_x - S_x'}{\sqrt{2}} = \begin{pmatrix} 0 & 0 & 0 \\ 0 & 0 & 1 \\ 0 & 1 & 0 \end{pmatrix} \qquad S_y^+ = \frac{S_y + S_y'}{\sqrt{2}} = \begin{pmatrix} 0 & 0 & 0 \\ 0 & 0 & -i \\ 0 & i & 0 \end{pmatrix} \\
S_x^- &= \frac{S_x + S_x'}{\sqrt{2}} = \begin{pmatrix} 0 & 1 & 0 \\ 1 & 0 & 0 \\ 0 & 0 & 0 \end{pmatrix} \qquad S_y^- = \frac{S_y - S_y'}{\sqrt{2}} = \begin{pmatrix} 0 & -i & 0 \\ i & 0 & 0 \\ 0 & 0 & 0 \end{pmatrix}.
\end{aligned}
\tag{3.9}
$$

We can then re-write 3.8 as

$$
\tilde{H}_{ctrl} = \left(\frac{\Omega_1 \cos(\phi_1)}{2} + \frac{\Omega_2 \sin(\phi_2)}{2} \right) S_x^+ + \left(\frac{\Omega_1 \cos(\phi_1)}{2} - \frac{\Omega_2 \sin(\phi_2)}{2} \right) S_x^- \tag{3.10}
$$

$$
+ \left(\frac{\Omega_2 \cos(\phi_2)}{2} - \frac{\Omega_1 \sin(\phi_1)}{2} \right) S_y^+ + \left(\frac{\Omega_2 \cos(\phi_2)}{2} + \frac{\Omega_1 \sin(\phi_1)}{2} \right) S_y^- \tag{3.11}
$$

Since Ω_1,Ω_2, ϕ_1, and ϕ_2 are all independent and adjustable, we reach four independent degrees of freedom and it becomes clear how to set one of the pre-factor one of the operators of the Hamiltonian and the remaining three to zero, triggering one transition over the others by solving the four equations of the pre-factors with four degrees of freedom. Thus, with 1) two independent microwave sources, 2) a zero magnetic field, 3) knowledge of the amplitude and phase of each microwave source as seen by the NV center (which depends on the distance of the NV center from each microwave source as well as its orientation), it is possible to activate a Single Quantum Transition (SQT) from $|0\rangle$ to any of the two other levels without populating the last level.

For example, using $\Omega_1 = \Omega$, $\Omega_2 = \Omega$, $\phi_1 = 0$ and $\phi_2 = \pi/2$, we will get contribution from the first term only, S_x^+. Measuring the final state once more, the population evolution of $|0\rangle$ is :

$$
\begin{aligned}
P(t) &= \left| \langle 0| \, e^{-i\Omega S_x^+ t} \, |0\rangle \right|^2 \\
&= \frac{1 + \cos(2\Omega t)}{2}
\end{aligned}
$$

Which is faster than the Rabi oscillations from the single transition with a field by a factor

of 2, see section 3.1.1. At the same time, the population of $|-1\rangle$ and $|1\rangle$ evolve like:

$$\begin{aligned} P_1(t) &= \left|\langle 1| e^{-i\Omega S_x^+ t} |0\rangle\right|^2 &&= \frac{1-\cos(2\Omega t)}{2} \\ P_{-1}(t) &= \left|\langle -1| e^{-i\Omega S_x^+ t} |0\rangle\right|^2 &&= 0 \end{aligned}$$

Double transition

Without an external magnetic field, we only need a single microwave source to generate the transition between $|0\rangle$ and the coherent superposition of $|-1\rangle$ and $|+1\rangle$.

Following section 3.1.1, we will set the first frequency to $\omega_1 = \Delta$ and because there is no magnetic field, $\omega_z = 0$ and $\omega_2 = 0$ as well. In the lab frame, the Hamiltonian is $H_0 + H_{ctrl} = \Delta S_z^2 + 0S_z + \sqrt{2}\Omega(t)\cos(\omega_2 t)\cos(0t)S_x$

Following equation 3.4, it becomes

$$\begin{aligned} \tilde{H}_1 &\approx 0S_z + \Omega\frac{\cos(0t)}{\sqrt{2}}S_x \\ &= \frac{\Omega}{\sqrt{2}}S_x \end{aligned}$$

Finally, measuring one more time gives:

$$\begin{aligned} P(t) &= \left|\langle 0| e^{-i\frac{\Omega}{\sqrt{2}}S_x t} |0\rangle\right|^2 \\ &= \frac{1+\cos\left(\sqrt{2}\Omega t\right)}{2} \end{aligned}$$

Which is faster than the Rabi oscillations from the single transition with a field by a factor of $\sqrt{2}$

3.1.3 Insight from the previous section

Table 3.1 collects the relative frequencies collected in the previous sections. From it, few relationships can be seen.

Field regime	Target Transition	μw sources	Rabi Frequency
High	Single transition	1	Ω
field	Double transition	1	$\Omega/\sqrt{2}$
No	Single transition	2, $\perp$	2Ω
field	Double transition	1	$\sqrt{2}\Omega$

Table 3.1: Relative Rabi frequencies under different regimes and with different objectives. $\perp$ expresses that the microwave sources are perpendicular.

First, generating transitions to both levels instead of one increase the frequency by a factor of $\sqrt{2}$. This can be seen through the definition of the operators; S_x includes a factor of $1/\sqrt{2}$ which σ_x does not possess. Thus when we can express the Hamiltonian in terms of S_x instead of σ_x, a factor of $\sqrt{2}$ is absorbed in the spin-1 operator, speeding up the Rabi oscillations by the same factor. This is highlighted by the difference between the single transition with a field and the double transition without a field.

Second, whenever we need to apply a Rotating Wave Approximation, half the power goes to the counter rotating part of the Hamiltonian, cutting the frequency in half. This is highlighted by the difference between the double transition with and without a field.

Third, using a second microwave source and doubling the available power doubles the Rabi frequency. This is highlighted by the difference between the single transition at high field and the single transition at no field.

3.2 Two wires board

We have talked in length of the microwaves sources being parallel or perpendicular in the frame of the NV center. For the following experiments, we will deal with the wires themselves. In order for the two wires to be close enough, parallel and not touching, Thomas Alexander designed a printed board (figure 3.2) on top of which a thin diamond (thickness of 100 μm) is secured with wax. This sample holder was designed to minimize the mutual inductance of the wires. With that in mind, we measured the transmission and reflection of the signal with an Agilent 4-ports Vector Network Analyzer (VNA) (N5230A PNA-L 4-Port Network Analyzer). We calibrated the four cables used with the Network Analyzer to account for the phase and the power loss in them for the reflection and the transmission. The plane of reference is then the interface between the cables and the sample board. When we used a same small connector to connect the cables pairwise, we neglected the insertion loss and the phase accumulated through the connector.

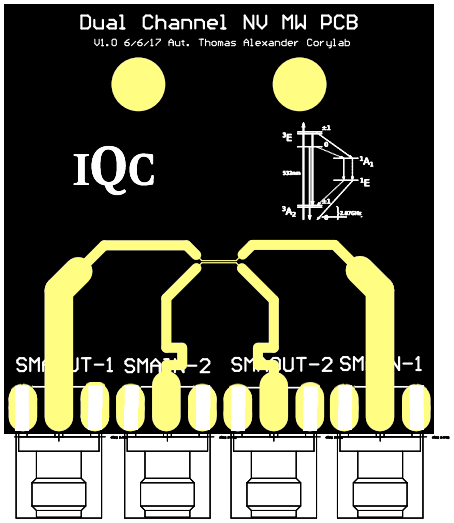

(a) Schema of the PCB, top view. The diamond is placed on top of the middle section, where the wires are brought close together. From left to right, the ports of the device under test are connected to the ports 1 through 4 of the VNA. The sample board itself (black section) is 5 cm by 5 cm.

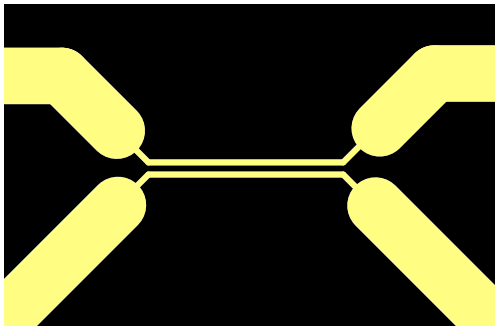

(b) Detail of the PCB sample board where the diamond sits. Each wire is 127 μm thick (5 mils) and the spacing between the wires is also 127 μm.

Figure 3.2: Top view of the parallel wires setup on a PCB.
This first generation of PCB consists of printed wires, without transmission lines or optimisation. The diamond taht sits on the wires is 5 mm long, 2 mm wide and 0.1 mm thick.

To discuss the transmission and the reflection of the device under test, we connected the port 1 of the VNA to the SMA OUT-1 port, port 2 to the SMA IN-2 port, port 3 to the SMA OUT-2 port and port 4 to the SMA IN-1 port. In consequence, measuring S12 tells us about the transmission between the ports SMA OUT-1 and SMA IN-2 and measuring S34 tells us about the transmission between the ports SMA OUT-2 and SMA IN-1, for example. Similarly, measuring S33 will give the reflection at the SMA OUT-2 port.

Looking at the results in figure 3.4 the desired transmission (S41 and S23, see figure 3.2a) is relatively stable and takes values of -1.03 dB with a standard deviation of $\sigma = 0.08$ dB and -2.90 dB with $\sigma = 0.16$ dB, respectively. All these values are relative to the power output by the Network Analyzer into the circuit. On the other hand, the leakage of signal

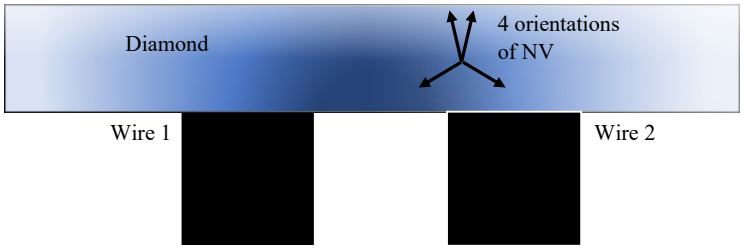

Figure 3.3: Cross section of the diamond (seen from the side of fig: 3.2a). The NV of interest is not necessarily in the center and its orientation is not predetermined.

from the input of one wire to the input of the other, as well as similarly for the output (S42 and S13), is -17.9 dB ($\sigma = 0.9$ dB) and -19.1 dB ($\sigma = 1$ dB). There is then a factor of 15 dB of isolation ($\sigma = 1$ dB), when the signal goes into the first input, between the two legs of the circuit across the junction while the isolation is 18 dB ($\sigma = 1$ dB) between SMA IN-1 and SMA OUT-2 when the signal comes from port SMA IN-2. The last pair of transmissions (S43 and S12) is the leaking signal that stays on the same half of the PCB. We treat this signal as crossing the gap between the wires as early as possible, providing little to no signal to site where the NV center rests, closer to the center of the parallel wires. Their average is -9.13 dB ($\sigma = 0.14$ dB) and -8.09 dB ($\sigma = 0.17$ dB). To generate those two independent microwave sources, we used two parallel wires, controlled by an Arbitrary Waveform Generator (AWG). This design was chosen to simplify the geometry of the problem: in planes perpendicular to the parallel wires, each plane is identical and the two wires acting are treated like point sources, reducing the problem to 2 dimensions. The wires are placed on a Printed Circuit Board (PCB) to ensure that they are parallel. Each wire has a width of 127 μm (5 mils) and they are separated by the same distance (5 mils). On top of those wires, the diamond has a thickness of 100 μm, length of 4 mm and width of 2 mm.

As the original setup was used for single wires experiment, the electronics that were installed on this optical setup had a single double channel AWG for the quadrature signal, a circuit to modulate it around 2.87 GHz and an amplifier before the sample itself. With some of the work already done by Zimeng Wang previously, we installed a new AWG with two double channels and assembled the rest of the electronics to synchronize the two input signals on the same clock and characterized the power loss throughout the circuit, making sure that the power delivered to each wire was similar.

Similarly, the software to control all this experiment had previously been written by few graduate students and edited several times since 2009 (C. Ryan, J. Hodges, C. Granade, I. Hincks, O. Moussa, M. Kononenko). Because of the previous design, the code was designed

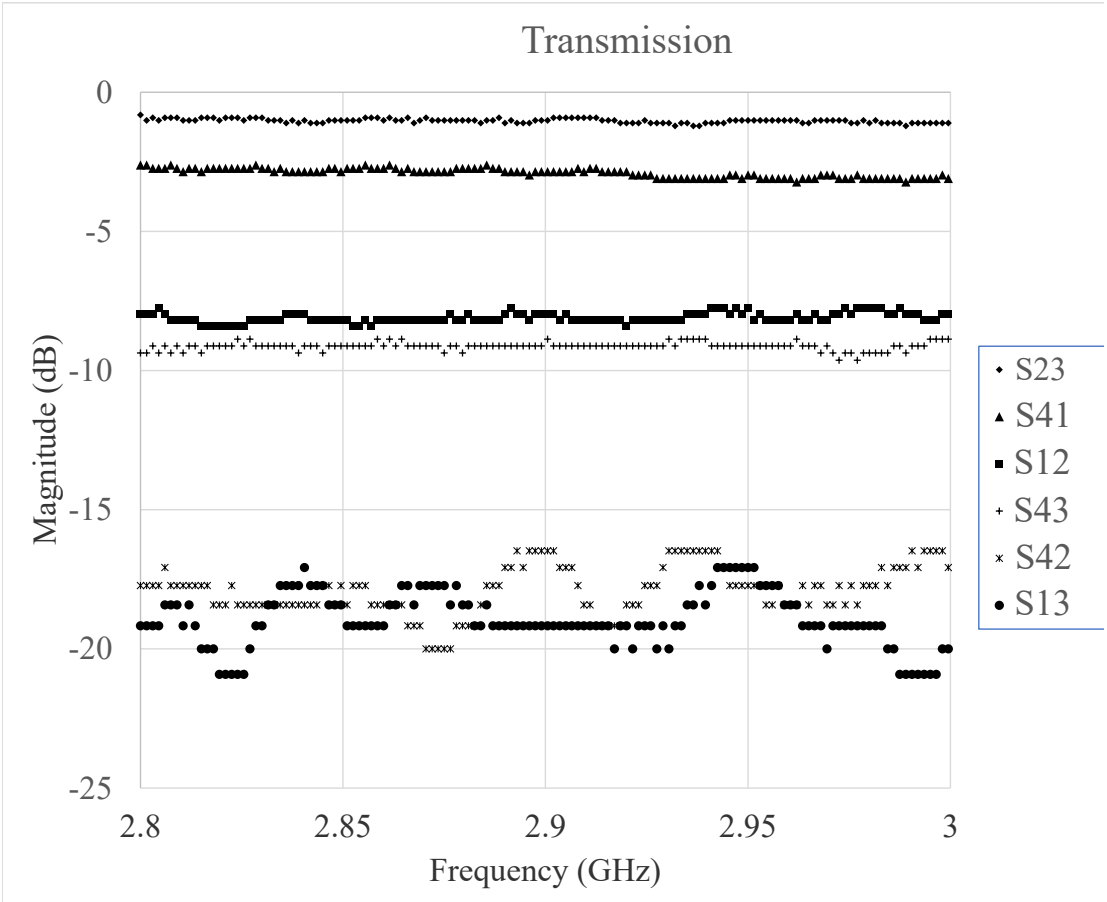

Figure 3.4: Response of the circuit for transmission. Transmissions forward and backward are similar. Their difference is less that 0.3 dB on average.

to control and display the current through one wire only. I modified the code so that the GUI displays the power diagrams for both wires and turns on the proper channels.

We ordered a thin diamond, 100 μm thick, of electronic grade, from Applied Diamond Inc. The diamond is first annealed on one side, at atmosphere pressure with a 80:20 Ar:O_2 gas mix. The annealing will help with conversion from neutral NV centers (NV^0) to negatively charged NV centers (NV^-). This process can be expected to increase the ratio of NV^-/NV^0 to a depth in the order of tens of μm [32]. It is then preferable to make sure that the side with higher concentration of NV centers is closer to the wires to achieve better coupling. The diamond is then cleaned in an ultrasonic bath of acetone, followed by one of isopropanol, for 20 minutes each, at room temperature. Finally, the diamond is mounted

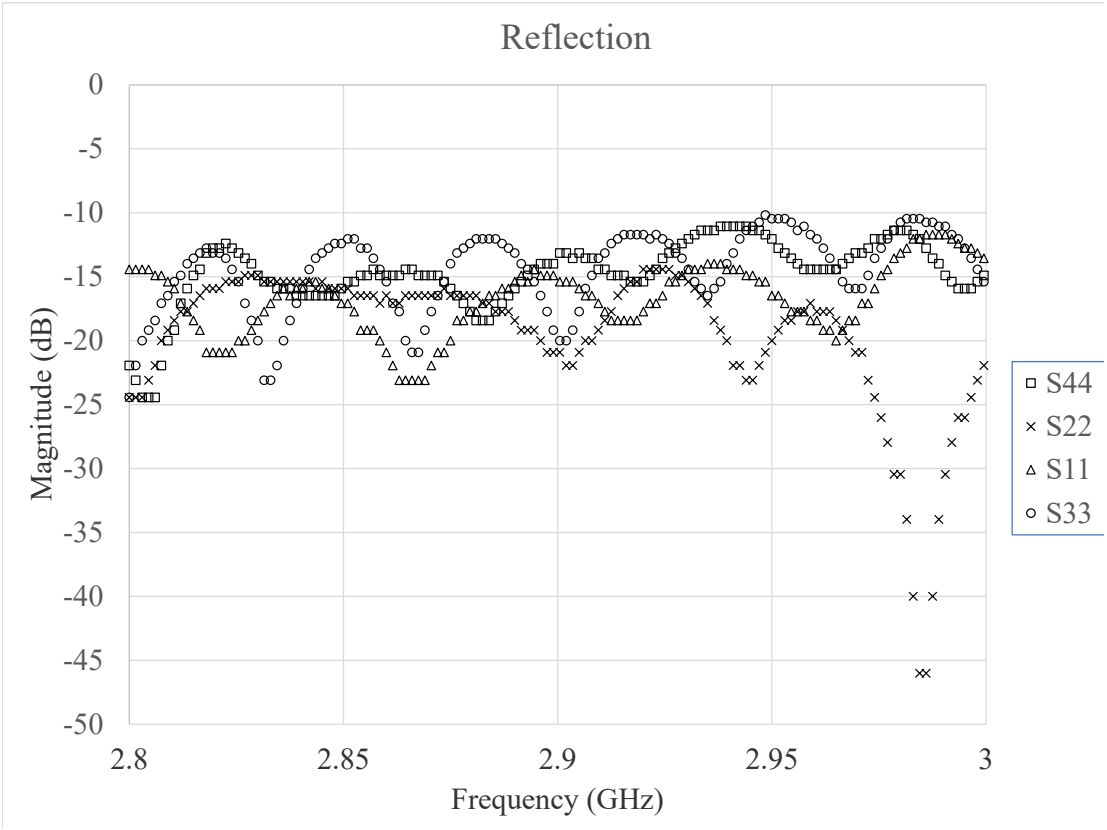

Figure 3.5: Reflections from and to the same port

on the sample board holder with a glue pump, by placing the diamond on a drop of melted wax. Heating the sample board, a piece of wax of millimeter dimension is carefully dropped on the wires, melting in a minute. The diamond is then placed with a vacuum pump; a needle, mounted on a three axis stage with micro-metric screws, that holds the diamond by suction. By pressing down the diamond, the wax spreads around the wires, leaving the diamond to touch them. The distance of the wax from the volume observed in the diamond is of the order of tens of micro-meters, and since the wax doesn't possess the same ZFS that the NV centers do, it will not introduce noise in our measurements. The advantage of using a glue pump is the ease of manipulation of the diamond compared to the manipulation with hands and tweezers. This is important for thin diamonds because with a thickness of $100\mu m$, they bend easily, pop, flip and jump, vanishing from sight.

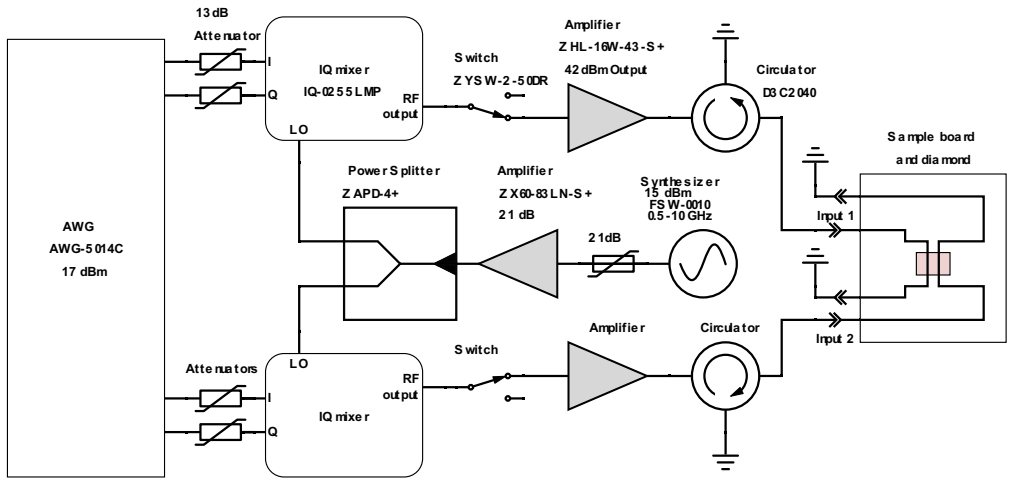

Figure 3.6: New circuit with 2 control wires on the sample holder

3.3 Two microwave sources

As we have seen in the last section, using two independent microwave sources can enable additional transitions. In this section, we will discuss the effect the orientation of the sources can have. It can be intuitive that if the microwave sources are parallel in the NV center frame, they can be reduced to a single source, and such, the more interesting case is complementary. Before looking at the general case, let's begin with two sources perpendicular.

3.3.1 Perpendicular microwave sources

With the tools from section 3.1.2 (no magnetic field, two microwave sources), S_x^+ and S_x^- can be generated from the general Hamiltonian, by carefully choosing Ω_1, Ω_2, ϕ_1 and ϕ_2. Applying them in succession generates a DQT, which is a population exchange between $|-1\rangle$ and $|+1\rangle$ while leaving $|0\rangle$ intact. With $U_+ = e^{-iS_x^+\frac{\pi}{2}}$ and $U_- = e^{-iS_x^-\frac{\pi}{2}}$, we can write:

$$U_-^+ = U_+ \cdot U_- \cdot U_+ = -\begin{pmatrix} 0 & 0 & 1 \\ 0 & 1 & 0 \\ 1 & 0 & 0 \end{pmatrix}$$

This enables a flip flop operator within the $\{|-1\rangle, |+1\rangle\}$ subspace, enabling experiments where each level is sensitive to the magnetic field, doubling the sensitivity to magnetic field. Indeed, this contrasts with NV center experiments that would use the $|0\rangle$ level, which is not sensitive to the magnetic field. Furthermore, working in this manifold allows to minimize the effect of errors from the Zero Field Splitting, since it does not separate $|-1\rangle$ and $|1\rangle$.

3.3.2 Microwave sources with arbitrary microwave orientation

In this section, we will look at the more general case, when the first microwave source is along $\hat{x}$, by definition, while the other degree of control is along an arbitrary direction $\cos(\theta)\hat{x} + \sin(\theta)\hat{y}$, each with independent amplitude and phase. The control Hamiltonian is then

$$H_{ctrl} = H^1_{ctrl} + H^2_{ctrl} \tag{3.12}$$

$$= \sqrt{2}\Omega_1 \cos(\omega_1 t + \phi_1) S_x + \sqrt{2}\Omega_2 \cos(\omega_2 t + \phi_2)(\cos(\theta) S_x + \sin(\theta) S_y) \tag{3.13}$$

In the absence of a magnetic field, the usual Rotating frame approximation will be made with $\omega_1 = \omega_2 = \Delta$. Again, as described in section 1.2, $S'_y = i[S_z^2, S_x]$ and similarly, $S'_x = i[S_z^2, S_y]$. In the rotating frame, the control Hamiltonian is expressed as :

$$\begin{aligned}\tilde{H}_{ctrl} =& \frac{\Omega_1 \cos(\phi_1)}{\sqrt{2}} S_x - \frac{\Omega_1 \sin(\phi_1)}{\sqrt{2}} S'_y + \\ & \frac{\Omega_2 \cos(\phi_2)}{\sqrt{2}} (\cos(\theta) S_x + \sin(\theta) S_y) - \frac{\Omega_2 \sin(\phi_2)}{\sqrt{2}} (\cos(\theta) S'_y + \sin(\theta) S'_x)\end{aligned} \tag{3.14}$$

Measuring at this stage already reveals something interesting:

$$\begin{aligned}P(t) &= \left| \langle 0| e^{-i\tilde{H}_{ctrl} t} |0\rangle \right|^2 \\ &= \frac{1}{2}\left(1 + \cos\left(\sqrt{2(\Omega_1^2 + \Omega_2^2 + 2\Omega_1\Omega_2 \cos(\theta)\cos(\phi_1 - \phi_2))}\ t\right)\right)\end{aligned} \tag{3.15}$$

Meaning that the Rabi frequency depends on the angle between the two microwaves sources (in the NV center frame) as well as the phase difference between them. This is interesting because θ is a parameter that is fixed, giving an upper bound on the Rabi frequencies; for $\Omega_1 = \Omega_2 = \Omega$ and $\phi_1 - \phi_2 = \theta$, we get

$$P(t) = \frac{1}{2}\left(1 + \cos\left(\sqrt{1 + \cos^2(\theta)}\ 2\Omega t\right)\right) \tag{3.16}$$

This will reach a maximum when $\theta = 0$, for a Rabi frequency of $2\sqrt{2}\Omega$, when the sources are parallel. This is simply doubling the available power in the case of the NV center under no field and for a double transition, which also doubles the Rabi frequency:

$$\tilde{H}_{ctrl}(\Omega_1 = \Omega_2 = \Omega, \phi_1 = \phi_2 = \theta = 0) = \sqrt{2}\Omega S_x \tag{3.17}$$

Alternatively, if $\theta = \pi/2$, we can get the fastest SQT, to $|+1\rangle$ (with $\phi_2 = \pi/2$) or to $|-1\rangle$ (with $\phi_2 = -\pi/2$):

$$\tilde{H}_{ctrl}(\Omega_1 = \Omega_2 = \Omega, \phi_1 = 0, \phi_2 = \pm\pi/2, \theta = \pi/2) = \Omega S_x^{\pm} \tag{3.18}$$

3.3.3 Microwave sources with arbitrary microwave orientation and no magnetic field

This case of the microwaves being perpendicular is unlikely to arise with our current setup because it would require the NV center that we are studying to have a PAS parallel to the wires, which we did not look to achieve in this setup. In the more general Hamiltonian, shown in equation 3.13, the second microwave source will have some contribution from S_x as well as S_y.

Let's spend some time to look at this Hamiltonian in the rotating frame (as in equation 3.14). Since our operators are Hermitian and only have four non-zero entries, at the same positions, the total Hamiltonian can be simplified:

$$H = \begin{pmatrix} 0 & A & 0 \\ A^* & 0 & B \\ 0 & B^* & 0 \end{pmatrix} \tag{3.19}$$

Where we have

$$A = \frac{\Omega_1}{2} e^{-i\phi_1} + \frac{\Omega_2}{2} e^{-i(\theta+\phi_2)} \tag{3.20}$$

$$B = \frac{\Omega_1}{2} e^{i\phi_1} + \frac{\Omega_2}{2} e^{i(\theta-\phi_2)} \tag{3.21}$$

In a zero field setting, we then want to activate one transition at a time, setting $A = 0$ or $B = 0$. Using $\Omega_2 = \Omega_1$ and $\phi_2 = \pi + \phi_1 + \theta$, we get $B = 0$ and

$$H_{ctrl}^{-} = \Omega_1 \sin(\theta)[\sin(\theta + \phi_1)S_x^{-} - \cos(\theta + \phi_1)S_y^{-}] \tag{3.22}$$

While using $\Omega_2 = \Omega_1$ and $\phi_2 = \pi + \phi_1 - \theta$, we get $A = 0$ and

$$H^+_{ctrl} = \Omega_1 \sin(\theta)[\sin(\theta - \phi_1)S^+_x - \cos(\theta - \phi_1)S^+_y] \tag{3.23}$$

In both cases, we notice a same common factor of $\Omega_1 \sin(\theta)$, which reinforces the idea that the angular momentum specific operators can only be present if $\theta \neq 0$, if the microwave sources are not parallel.

Measuring one more time and taking H^+_{ctrl} without loss of generality, we get

$$\begin{aligned} P(t) &= \left| \langle 0| \, e^{-iH^+_{ctrl}t} \, |0\rangle \right|^2 \\ &= \frac{1 + \cos(2\Omega_1 \sin(\theta)t)}{2} \end{aligned}$$

This gives us a relationship for the maximal Rabi frequency we can expect for an arbitrary orientation of microwave sources in the absence of a magnetic field.

3.3.4 Microwave sources with arbitrary microwave orientation and magnetic field

In section 3.1.1, we established that with a single microwave source and a magnetic field, we could generate transitions from $|0\rangle$ to another level. We will now quickly look at what a second microwave source brings to this situation.

In both cases, the frame transformation to $(\Delta + \omega)S^2_z$ will leave the same internal Hamiltonian: $\tilde{H}_0 = \omega(S_z - S^2_z)$. We restrict our attention to the case where both amplitudes are equal: $\Omega_1 = \Omega_2 = \Omega$ and without loss of generality, we set the phase (of the only or the first source) to zero: $\phi_1 = 0$. The difference then lies in the angle and the phase between each microwave source.

Setting $\phi_2 = -\theta$, the control Hamiltonian is then

$$\tilde{H}_{ctrl} = \begin{pmatrix} 0 & \Omega & 0 \\ \Omega & 0 & \Omega\cos(\theta)e^{-i\theta} \\ 0 & \Omega\cos(\theta)e^{i\theta} & -2\omega \end{pmatrix} \tag{3.24}$$

The θ dependent entries of the matrix vanish for $\theta = \pi/2 + n\pi$ with $n \in \mathbb{Z}$, when the two microwave sources are perpendicular. They take the real value of Ω for $\theta = n\pi$, when the sources are parallel, and complex values in between.

Let's remember from the linear case (section 3.1.1), that since $\omega >> \Omega$, the lower part of the matrix can be approximated as a σ_z operation and doesn't trigger transitions between levels. The transition happens because of the top left section of the matrix, which is independent of the angle.

In consequence, with a magnetic field, there is no increase in Rabi frequency from using perpendicular microwave sources, we only get a better approximation. The difference between the parallel and perpendicular situations becomes apparent in the absence of magnetic field, where we can take advantage of the angular momentum difference between the levels of the NV center instead of relying on their energy difference.

3.4 Theoretical target

From previous work in the group by Z. Wang [33], and as we demonstrated, it was shown that once the amplitude and the phase can be individually addressed, we can generate SQT and DQT as necessary. Wang demonstrated, with ideal unitaries, how one can use a GRadient Ascent Pulse Engineering (GRAPE) algorithm to ensure that the pulse will reach a fidelity of 99.9% over a sample volume of $\sim$10 nm^2. In the next few sections, we will present methods to characterise the amplitude and the phase, such that these previously simulated pulses can be generated.

3.4.1 Data collection

This section will revisit the data collection of a general experiment (see figure 1.4) while applying it to the Rabi experiment scheme.

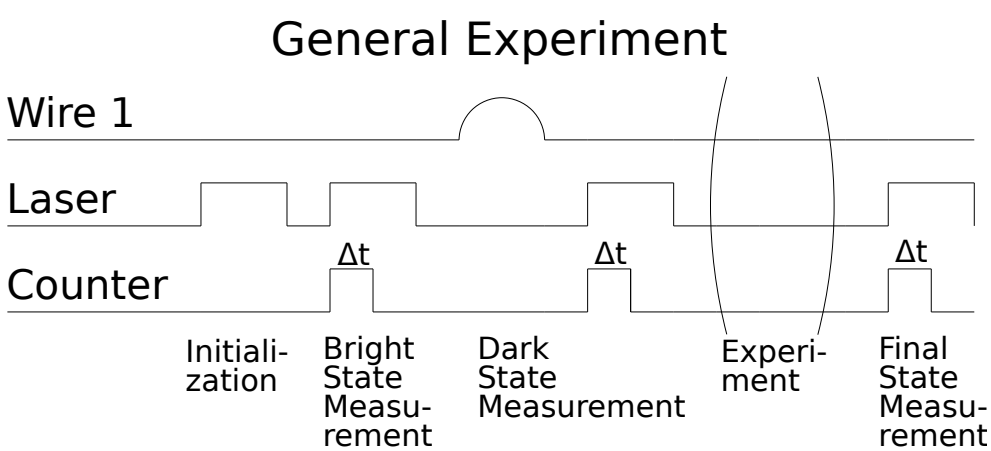

Figure 1.4: Outline of a single shot of an experiment.

During the Initialization, a laser pulse polarizes the NV center to $|0\rangle$. During the Bright State Measurement, the counter opens to measure the photons emitted by the NV center in the $|0\rangle$ state. The Dark State Measurement sees an adiabatic pulse to invert populations followed by the counter opening again to measure the photons emitted by the NV center in the $|-1\rangle$ state. The Experiment is kept general for now. During the Final State Measurement, the counter opens one last time to measure the photons emitted by the NV center in the state of interest.

The first one is the bright reference, which serves as a reference for the NV center in the $|0\rangle\langle 0|$ state. To prepare this state, we shine the green laser for 3 μs, to ensure the polarization in the $m_s = 0$ state (see section 1.4 and Figure 1.3). We wait 1.5 μs to make sure that everything is settled, since the longest shelf time is 300 ns (see section 1.3). Finally we open the counter and shine the laser for 600 ns to measure the number of photons $|0\rangle\langle 0|$ will emit. The laser is left on for an additional 2.4 μs to re-polarize the NV center at the same time.

The second one is the dark reference, which serves as a reference for the NV center not in the $|0\rangle\langle 0|$ state. To prepare this state, we start from the polarized state prepared by the last step and apply an adiabatic pulse that slowly inverses the polarity of the NV center ($|0\rangle \rightarrow |1\rangle$) over a $1/\Delta \approx 300$ ns time frame, with Δ being the Zero Field Splitting. We wait 1.5 μs to make sure that everything settled and again, open the counter for 600 ns as well as the laser to measure the number of photons emitted in the dark state. The laser is left on for 3 μs to repolarize the NV center.

For the Rabi experiment, the experiment, its measurement and its re-polarization are performed twice for each increment of time, to prepare and measure the state of the NV center with a square wave excitation from either wire, with time t, for the Rabi pulse duration. After each of those experiment, the counter is open 600 ns once more to measure the signal and re-polarize. The outline of this experiment is given in figure 3.7

The photon count is then mapped to population of $|0\rangle\langle 0|$ with the following equation:

$$\mathrm{Tr}[\rho\,|0\rangle\langle 0|] = \frac{\text{signal - dark reference}}{\text{bright reference - dark reference}} \tag{3.25}$$

For a given value of t, the experiment is repeated few thousand times before moving to the next value. Once all the points have been sampled that way, we perform a tracking routine to confirm that the NV center hasn't moved too much, before collecting another round of

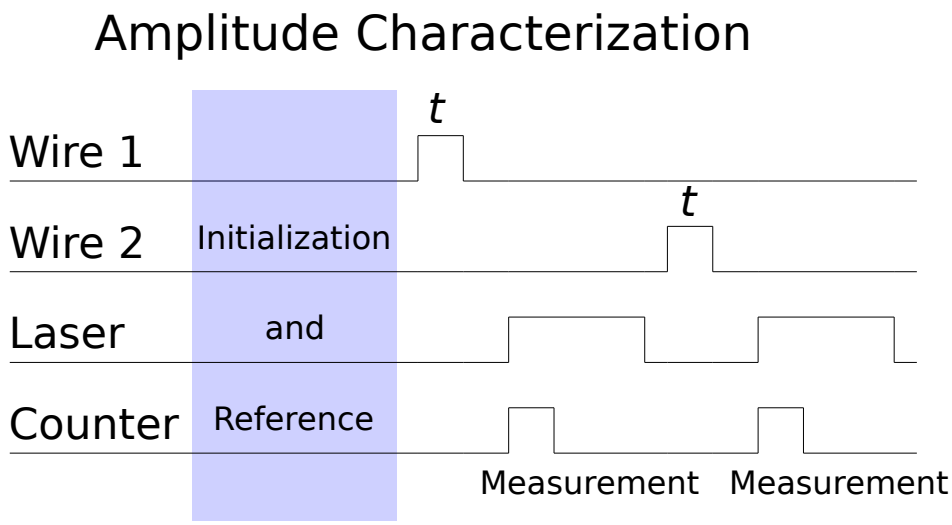

Figure 3.7: Pulse diagram of the Rabi Experiment.
After a sequence of initialization done as in section 1.4.1, a square pulse of duration t is applied from either wire 1 or wire 2 and the final state is recorded to measure the Rabi frequency of each microwave source.

each data point. If it becomes necessary, this tracking routing moves the galvanometers such that the focal point remains on the brightest spot. Since many factors can move the sample (humidity and temperature being the most obvious), we perform this tracking routine multiple times during the experiment instead of collecting all the data at once.

3.5 Relative amplitude

In an ideal situation, both microwave sources would be produced identically and would be going through an identical circuit before reaching the NV center. That NV center would be at equal distance from each wire and would see similar field coming from each wire. Since this situation is unlikely, we need to characterize the coupling of each source to the NV center in its frame and adjust it as necessary. To measure and correct that imbalance, we choose to perform a Rabi experiment with each of the microwave sources, one at a time. This way, we can measure the imbalance in the circuit directly where it matters, at the site of the NV center, rather than keeping track of the accumulation of errors in each part of the circuit. These Rabi experiments will be conducted in a field and target the transition $|0\rangle \leftrightarrow |-1\rangle$ since we will also require a magnetic field to calibrate the phase. See section

3.1.1 for a description of a Rabi experiment in high field.

Fits from experiments summarized in figure 3.9 and 3.10 give us a hint of a beating between two frequencies. They are due to the hyperfine splitting of the Nitrogen, which introduces a $A_{N,\parallel}S_z$ term to the Hamiltonian. Given that the relaxation time of the Nitrogen is of the order of the millisecond and that our experiments are all well under that time scale, it is a fair approximation to estimate our results as the average of 3 experiments conducted under different magnetic fields, at $-A_{N,\parallel}S_z$, at 0 and at $+A_{N,\parallel}S_z$. In the cases where the field due to the Nitrogen is not 0, the microwaves are then not on resonance. This increases the Rabi frequency to $\Omega' = \sqrt{\Omega^2 + A_{N,\parallel}^2}$ while reducing the contrast.

Given experimental values of $A_{N,\parallel} = -2.14$ MHz [34] and the values of our Rabi frequency around 5 MHz, we would expect to distinguish the peaks on the Fourier Transform plots. As this is not the case, we chose not to fit the beating and simplify the fit model for the data. This simplified model doesn't include effects from the nearby Nitrogen. The fit are then chosen to support a single frequency and a T_2 relaxation. It accepts smaller values for the amplitude of the oscillation as well as its average. The T_2 values are comparable to the values previously obtained with the previous experimental setup. Results are summarized in table 3.2.

Parameter	Value for the fit of the first wire (95% confidence interval)	Value for the fit of the second wire (95% confidence interval)
A	0.23 (0.18, 0.27)	0.24 (0.20, 0.28)
ω (MHz)	5.506 (5.498, 5.514)	5.277 (5.269, 5.284)
T_2 (μs)	6 (3, 9)	5 (3, 8)
C	0.55 (0.54, 0.56)	0.54 (0.53, 0.56)

Table 3.2: Fit of the Rabi oscillations displayed in figure 3.9 using MATLAB fit function. Function fitted: $\mathrm{Tr}[\rho\,|0\rangle\langle 0|] = A\cos(2\pi\omega t)e^{-t/T_2} + C$

3.6 Relative phase

Similarly to the previous section, we will perform specific experiments to measure the angle between the two microwave sources in the frame of the NV centers. This second crucial parameter will enable Single Quantum Transitions by giving the relative phase between each microwave source to reach the desired operations. The first experiment we performed

is an experiment that generates discrete increments of rotation by z, which we then call a Discrete Ramsey experiment. The procedure is as follow.

After making sure that the amplitudes from the wires are well calibrated relative to one another with the previous experiment, we applied a small magnetic field with a permanent magnet to generate a 100 MHz splitting (about 35 Gauss). The position of the magnet is determined by placing the magnet at different locations allowed by the stage arm and recording the splitting produced at the NV center. Using simulation tools and interpolation, we can use this data to predict where the magnet should be placed to produce a field exclusively along the PAS of the NV of interest, without worrying about its orientation in the lab frame. This will ensure that we will be allowed to work with pseudo 1/2 spin operators and that the usual Pauli commutation relations will be observed; a Bloch Sphere will be appropriate for illustration.

Hence, after calibrating the power of the micro wave sources so that they have the same values, we prepare the NV center in the $|0\rangle$ state. Given the splitting field, we apply a $\pi/2$ rotation with the first microwave source to bring the NV center to a superposition of $\frac{|0\rangle+|1\rangle}{\sqrt{2}}$. Once this state is prepared, we apply a π rotation by the second wire, followed by a π rotation by the first wire. These two π rotations constitute one increment, which will be repeated multiple times. Finally, a last rotation by $-\pi/2$ by the first source will allow for measurement along the quantization axis. See figure 3.11 for a graphical description.

Expressing the first microwave source along $\hat{x}$, the second microwave source will be expressed θ away, resulting in some orientation of $n_2 = (\cos(\theta), \sin(\theta), 0)$. Given the Pauli matrices relationships, a π pulse in this direction is given by

$$\begin{aligned}
U_{\hat{\theta}}(\pi) &= e^{-i(\cos(\theta)\frac{\sigma_x}{2}+\sin(\theta)\frac{\sigma_y}{2})\pi} \\
&= -i(\cos(\theta)\sigma_x + \sin(\theta)\sigma_y) \\
&= -i(\cos(\theta)\sigma_x + \sin(\theta)(i\sigma_x\sigma_z)) \\
&= (-i\sigma_x)(\cos(\theta) + i\sin(\theta)\sigma_z) \\
&= e^{-i\pi\frac{\sigma_x}{2}} e^{i2\theta\frac{\sigma_z}{2}}
\end{aligned}$$

When this pulse is preceded by a π pulse by $\hat{x}$, the two π pulses accumulate to the identity, leaving us with the 2θ rotation by $\hat{z}$. By inspection, we can see that θ and $\theta+\pi$ will generate the same evolution since the extra π factor is multiplied to the identity. Furthermore, taking the conjugate square of this unitary highlights the fact that a θ or $-\theta$ gives the same result.

Therefore, generating series of π pulses will generate an evolution around the $\hat{z}$ direction, for which a Ramsey experiment measure the frequency. Since the evolution is discrete and counted in terms of increments of steps rather than a continuous time evolution, we will

call this a Discrete Ramsey experiment. The angular frequency will correspond to twice the angle between the microwaves in the transverse plane, remains to find the appropriate quadrant.

Parameter	Value from the fit (95% confidence interval)
A	0.37 (0.28, 0.45)
θ (rad)	0.390 π (0.386π, 0.395π)
ϕ (rad)	1.6π (1.5π, 1.7π)
T_2 (increment)	11 (7, 17)
T_2 (μs)	2 (1, 3)
C	0.45 (0.43, 0.47)

Table 3.3: Fit of the Discrete Ramsey experiment oscillations displayed in figure 3.12 using MATLAB fit function.
Function fitted: $\mathrm{Tr}[\rho\,|0\rangle\,\langle 0|] = A\cos(\pi(2\theta)n + \phi)e^{-t/T_2} + C$

This separation angle is intrinsic and can't be changed for a given NV center but we can adjust their relative phase to modify the effective angle between them. It is important to distinguish the angle between the projection of the wire (which is fixed) and the phase of each current that goes through them (which can be varied to adjust the final Hamiltonian at the NV center). They both have an influence on the control we have on the NV center, but arise from different reasons.

Figure 3.12 displays the result of this experiment. The low contrast is mostly due to a combination of detuning and over- or under-rotation of the $\pi/2$ pulses, which then leave the NV center not in the transverse plane.

The fit on the data gives: $f(n) = A\cos(2\pi(2\theta)n + \phi)\, e^{-n/T_2} + C$, where $f(n)$, A, θ, n, ϕ, T_2 and C are: the dependent variable ($\mathrm{Tr}[\rho\,|0\rangle\,\langle 0|]$), the amplitude of the oscillations, the angle between the two microwave sources, the number of pairs of π pulses, the phase shift, the transverse relaxation time, and the offset, respectively. Values for these parameters are given in table 3.3.

3.7 Absolute phase

When conducting the previous experiment, we became aware of the fact that the 2θ rotation could be too fast to record properly. Indeed, sampling after every 2θ rotation, for $\theta > \pi/2$,

provokes under-sampling, since we can't sample faster than the Nyquist frequency. In fact, any of the four frequencies $\theta = \pm\pi \pm \theta'$, where θ' is the value of interest, would give us similar data. We then conducted a second experiment that would be sensitive to the quadrant in which θ would be.

Here is its procedure.

After calibrating the bright and dark state as usual, we prepare the NV center in its $|0\rangle$ state by applying the usual green laser. With the given magnetic field, we apply a $\pi/2$ rotation with the first microwave source, fixing its phase to $\phi_1 = 0$, to bring the NV center to a superposition of $\frac{|0\rangle+|1\rangle}{\sqrt{2}}$. Immediately after, we apply another $\pi/2$ rotation with the second microwave source, with a phase ϕ_2, which will be our independent variable. At this point, the state readout is going to be the dependent variable.

Again, assuming that the first pulse can be expressed along $\hat{x}$ exclusively, the second microwave source will be along $\cos(\theta)\hat{x} + \sin(\theta)\hat{y}$. Assuming that 1) the magnetic field is positive, 2) it produces a splitting of ω and 3) $\omega >> \Omega$, then in the rotating frame, the Hamiltonians are

$$H_1 = \frac{\Omega}{\sqrt{2}}\cos(\phi_1)S_x - \frac{\Omega}{\sqrt{2}}\sin(\phi_1)S'_y + \omega(S_z + S_z^2) \tag{3.26}$$

$$\begin{aligned} H_2 = &\frac{\Omega}{\sqrt{2}}\cos(\theta)(\cos(\phi_2)S_x - \sin(\phi_2)S'_y) \\ &+ \frac{\Omega}{\sqrt{2}}\sin(\theta)(\cos(\phi_2)S_y - \sin(\phi_2)S'_x) \\ &+ \omega(S_z + S_z^2) \end{aligned} \tag{3.27}$$

At this point, as in section 3.1.1, we will use the qubit approximation to simplify the situation. This approximation is not necessary to reach the conclusion but it makes it easier to follow, by focusing our attention to one subset of the dynamics at a time. Looking at the lower part of the Hamiltonian (discarding anything involving $|1\rangle$), we have

$$H'_1 = \frac{\Omega}{2}(\cos(\phi_1)\sigma_x - \sin(\phi_1)\sigma_y) \tag{3.28}$$

$$H'_2 = \frac{\Omega}{2}(\cos(\theta - \phi_2)\sigma_x + \sin(\theta - \phi_2)\sigma_y)) \tag{3.29}$$

The extra factor of $\frac{1}{\sqrt{2}}$ comes from the definition of the spin-1 operators. σ_x and σ_y are the Pauli Operators.

Applying these two Hamiltonians one at a time to generate a $\pi/2$ pulse each time, the final state is

$$Pr(|0\rangle\langle 0|) = \mathrm{Tr}\Big[|0\rangle\langle 0| e^{-iH_2'\pi/(2\Omega)} e^{-iH_1'\pi/(2\Omega)} |0\rangle\langle 0| e^{iH_1'\pi/(2\Omega)} e^{iH_2'\pi/(2\Omega)}\Big] \tag{3.30}$$

$$= \frac{1}{2}(1 - \cos(\theta + \phi_1 - \phi_2)) \tag{3.31}$$

We then get a cosine oscillation as a function of ϕ_2 whose phase is given by $\psi_1 = \theta + \phi_1$. This doesn't seem too useful until we repeat the same experiment for the other resonant condition, when $(S_z + S_z^2) \to (S_z - S_z^2)$. We then turn our attention to the $|1\rangle$ and $|0\rangle$ part of the Hamiltonian by using the qubit approximation once more. We get:

$$H_1'' = \frac{1}{\sqrt{2}}(\cos(\phi_1)\sigma_x + \sin(\phi_1)\sigma_y) \tag{3.32}$$

$$H_2'' = \frac{1}{\sqrt{2}}(\cos(\theta + \phi_2)\sigma_x + \sin(\theta + \phi_2)\sigma_y)) \tag{3.33}$$

This second pulse sequence gives

$$Pr(|0\rangle\langle 0|) = \frac{1}{2}(1 - \cos(\theta - \phi_1 + \phi_2)) \tag{3.34}$$

This time, the phase is $\psi_2 = -\theta + \phi_1$. Taking the sum or the difference of the phases from each experiment then gives us the angle between the microwave sources and the phase of the first microwave in the NV center frame:

$$\theta = \frac{\psi_1 - \psi_2}{2} \tag{3.35}$$

$$\phi_1 = \frac{\psi_1 + \psi_2}{2} \tag{3.36}$$

For these experiments, we placed the magnet to produce a 40 MHz splitting. Their results are on figure 3.13, with the values for the fit in table 3.4. This then gives us a value for θ of $\theta = (-0.59 \pm 0.09)\pi$. This would then seem in rather good agreement with the value obtained from the Discrete Ramsey Oscillations, which, in the last section, gave us $\theta = (0.390 \pm 0.005)\pi$, granted that the quadrant is chosen appropriately (an addition of π would be adequate).

However, through the setup of the experiment, the symmetry of the circuit was not taken into consideration. Instead, each half of the circuit going from the AWG to the sample board was connected with cables of different length. Though this physical length translates

Parameter	Value for the experiment at 2.850 GHz (95% confidence interval)	Value for the experiment at 2.890 GHz (95% confidence interval)
A	0.19 (0.17, 0.21)	0.45 (0.38, 0.52)
ψ_1 or ψ_2 (rad)	1.13π (1.09π, 1.16π)	1.72π (1.67π, 1.77π)
C	0.32 (0.31, 0.34)	0.44 (0.39, 0.49)

Table 3.4: Fit of the pulsed experiment displayed in figure 3.13 using MATLAB fit function. Function fitted: $\mathrm{Tr}[\rho\,|0\rangle\langle 0|] = A\cos(2\pi\phi_2 + \psi_i) + C$

to different electrical lengths at a given frequency, this only translates to a different relative phase at the site of the NV center. More specifically, this relative phase then depends on the frequency, which means that the phase-phase experiments we conducted at two different frequencies have different relative phases. The results obtained in this section are then to be taken with a grain of salt and a more expansive description of this problem (and potential solutions) is given in chapter 4. In general, this phase dependence is mostly linear with the length of the wires when the circuit doesn't display resonances.

3.8 Relative phase at low field

The question remains of the necessity of the magnetic field to conduct all of these experiments. The fact is that using a magnetic field was a very nice tool to work with the Pauli operators but some relationships still apply at zero field, when we can't make the qubit approximation.

3.8.1 Discrete Ramsey experiment at zero field

Using an approach similar to section 3.6, we will assume the amplitudes have already been calibrated. Once they are calibrated, without the magnetic field, in the rotating frame, the control Hamiltonians of each microwave sources are:

$$\tilde{H}_1 = \Omega/\sqrt{2}(\cos(\phi_1)Sx - \sin(\phi_1)S'_y) \tag{3.37}$$

$$\tilde{H}_2 = \Omega/\sqrt{2}\big(\cos(\theta)(\cos(\phi_2)S_x - \sin(\phi_2)S'_y) + (\sin(\theta)(\cos(\phi_2)S_y - \sin(\phi_2)S'_x)\big) \tag{3.38}$$

While it is harder to work with the exponents of the spin-1 than those of the spin-1/2, the spin-1 operators exhibit the same property that we needed earlier. The second pulse

can be re-written as:

$$U_{\hat{\theta}}(\pi) = e^{-i(\cos\theta S_x + \sin\theta S_y)\pi} \tag{3.39}$$
$$= e^{-i\pi S_x} e^{-i(-2\theta)S_z} \tag{3.40}$$

Crucially, this is independent of the phase of the second pulse, ϕ_2. Similarly, the first unitary is independent of the first phase, of the Hamiltonian from the first microwave source, ϕ_1. Thus, if this re-written Unitary is preceded by a π pulse by $\hat{x}$, the first part accumulates to the identity and we are left with a $\hat{z}$ rotation by an angle 2θ.

Unlike the case of the experiment with a field, the angular frequency that we could measure would be given by:

$$\begin{aligned} P(t) &= \left| \langle 0| \, e^{-iS_x\pi/2} \cdot U_{\hat{\theta}}(\pi) \cdot e^{-i\tilde{H}_1\sqrt{2}\pi/\Omega} \cdot e^{-iS_x\pi/2} \, |0\rangle \right|^2 \\ &= \frac{1+\cos(4\theta)}{2} \end{aligned}$$

This second measure of the angle is now twice as sensitive to under-sampling, but can be used in conjunction with the first Discrete Ramsey experiment to narrow down the value of θ.

With the setup that we have currently, there is no efficient way to take out the magnet and reliably put it back at the same location. This limited the number of experiment we wanted to do. If we could achieve zero-field reliably, we could perform these experiments so the next chapter covers suggestions on how to improve the current setup to allow simple experiments at zero field, with other suggestions as well.

3.8.2 Phase-phase experiment at zero field

Encouraged by the new information one could get at zero field with a Discrete Ramsey experiment, one could be interested in repeating the Phase-phase experiment at zero field for a similar effect.

This time, the Hamiltonian imparted by each microwave source is given by:

$$H_1 = \frac{\Omega}{\sqrt{2}}\cos(\phi_1)S_x - \frac{\Omega}{\sqrt{2}}\sin(\phi_1)S'_y \tag{3.41}$$
$$H_2 = \frac{\Omega}{\sqrt{2}}\cos(\theta)(\cos(\phi_2)S_x - \sin(\phi_2)S'_y) + \frac{\Omega}{\sqrt{2}}\sin(\theta)(\cos(\phi_2)S_y - \sin(\phi_2)S'_x) \tag{3.42}$$

At this point, there is no point in looking at the top or the bottom part of the matrix since there is no suppression of transitions this time. The simple application of each pulse then gives:

$$\begin{aligned} P(t) &= \left|\langle 0| \, e^{-iS_1\pi/2} \cdot e^{-iH_2\pi/2} \, |0\rangle\right|^2 \\ &= \frac{1+\cos(2\theta)}{2} \end{aligned}$$

And this value is independent of ϕ_2, the variable we were sweeping. Thus, this would give us a single value, independent of the relative phase of each microwave source, to compare with our other methods. It is then advantageous to enable zero field experiments given these two experiments.

3.9 Confirmation of the characterization

Conducting few experiments, we can in theory confirm that we have the right values for the relative amplitudes as well as the angle between the microwave sources.

3.9.1 Confirmation of relative amplitudes

Using the characterization methods we laid out in this chapter, conducting Rabi experiments under various conditions can confirm that the ratio of the amplitudes is calibrated properly. As we only worked with a magnetic field, we prepared three experiments. The first one, the reference, is a single transition between $|0\rangle$ and $|1\rangle$ in a field, with a single wire, which gives us the value Ω. The second, a dual transition ($|0\rangle \leftrightarrow \frac{|-1\rangle+|1\rangle}{\sqrt{2}}$), in a field, also with a single wire, will give us a Rabi frequency of $\Omega/\sqrt{2}$. Finally, a third transition, between $|0\rangle$ and $|1\rangle$ in a field, but with both wires this time, will give us a Rabi frequency of 2Ω.

3.9.2 Confirmation of relative phase

Because the Rabi experiment at high field with two microwave sources is independent of the angle, these previous experiments don't confirm the relative phase. We need to use other experiments for that. Z. Wang described in her thesis [33], a pulsed experiment that follows this procedure: after preparing the NV center in $\frac{|-1\rangle+|+1\rangle}{\sqrt{2}}$ with a $\pi/2$ pulse by S_x,

Conditions	Frequency measured
1 wire	5.71 ± 0.02
Single Transition	5.37 ± 0.02
1 wire	3.90 ± 0.01
Dual Transition	3.99 ± 0.02
2 wires	11.37 ± 0.02
Single Transition	11.19 ± 0.02

Table 3.5: Rabi Frequency measured under different conditions.
For each condition, the frequency was measured twice.

we apply the pulse designed by the calibrating experiments. Applying a $\pi/2$ rotation by S_x to bring the NV center state back in the measurement subspace, we can observe the effect of the unitary. A double quantum transition will not have the same effect as a S_x operation or as the identity. Others [2, 3] use Electron Spin Resonance (ESR) experiments to show that one of the two transitions can be suppressed in a field. Once the electrical length issue is tackled and the relative phase is controlled, this straightforward experiment can be performed with fields large enough to produce non-overlapping ESR peaks or even at lower fields. The advantage of the larger fields is that in this regime, the qubit approximation can be used to reduce the problem to spin-1/2 dynamics and enable the Bloch equations to be used directly while the smaller fields let us confirm that the suppression of the transition can only come from the polarization of the microwaves, as opposed to de-tuning of the microwaves. A non-rigorous example of this low field ESR experiment is given in appendix E.

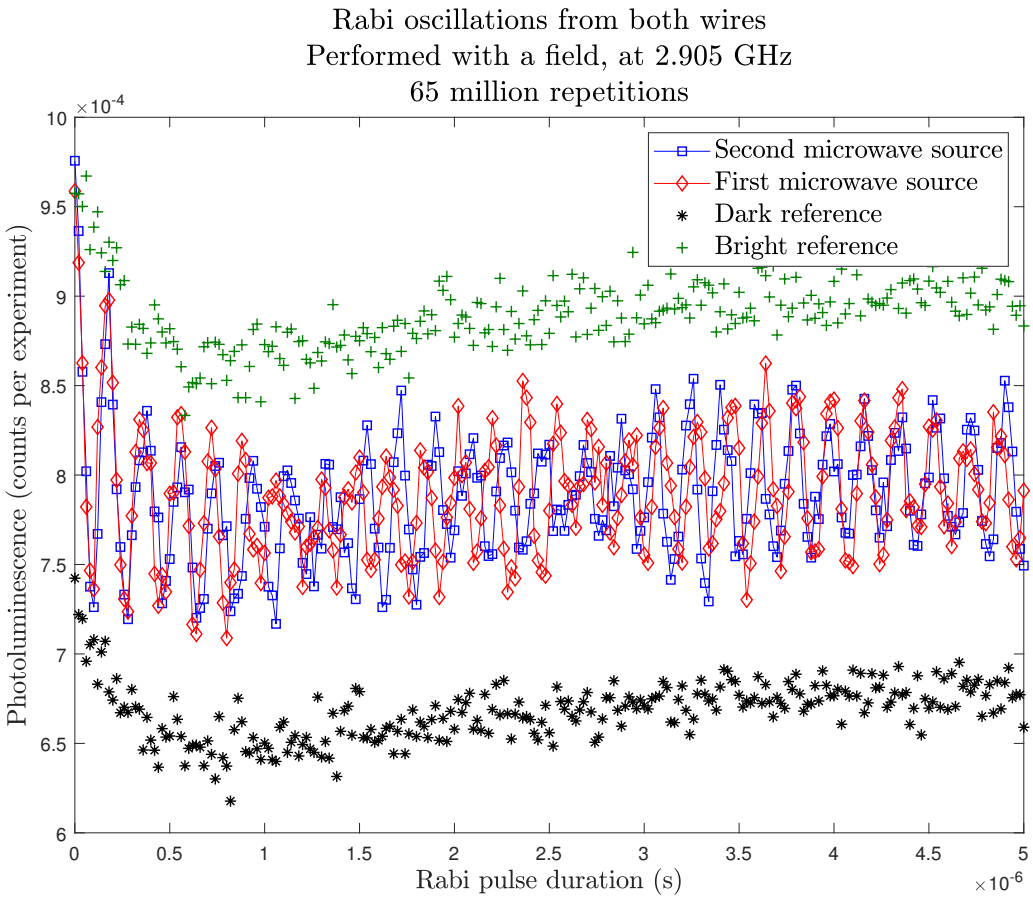

Figure 3.8: Rabi experiment repeated 65 million times for each wire. Line connecting each point is given as a guide to the eye.

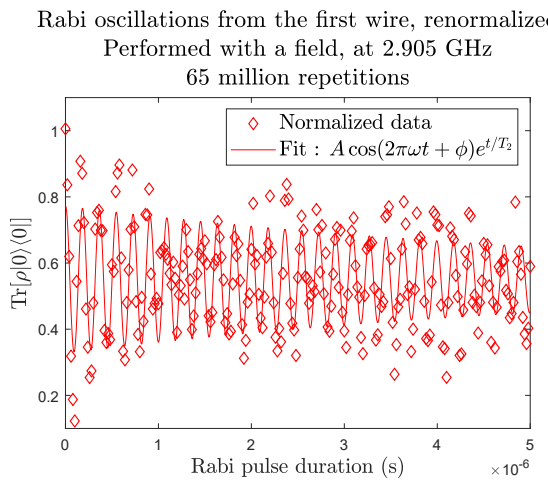

(a) Rabi oscillations when the system is driven by the first wire only.

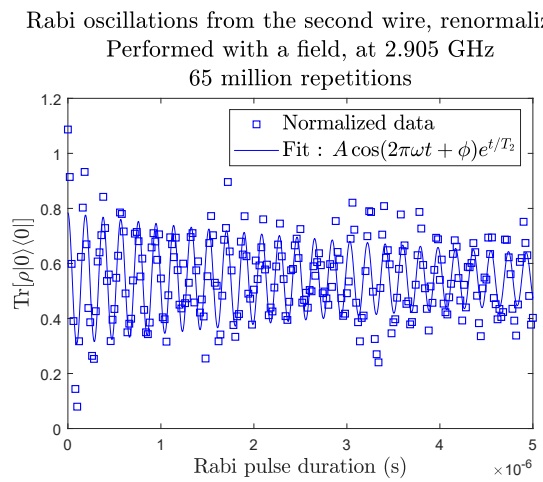

(b) Rabi oscillations when the system is driven by the second wire only.

Figure 3.9: Normalized data from 3.8. Line connecting the points is a guide to the eye. Fit results given in table 3.2

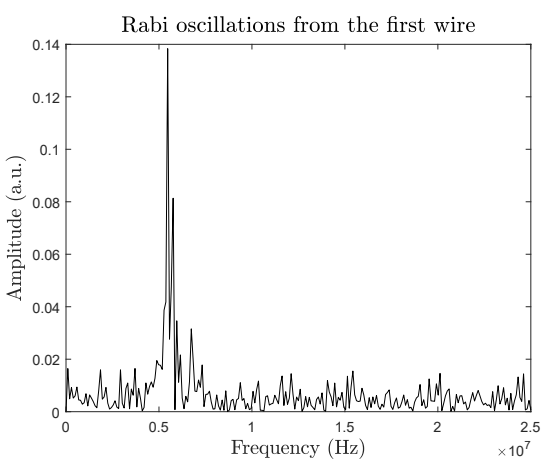

(a) Power Spectrum for Rabi oscillations when the system is driven by the first wire only.

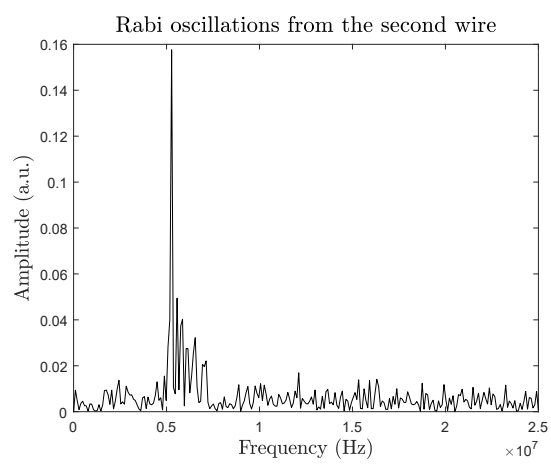

(b) Power Spectrum for Rabi oscillations when the system is driven by the second wire only.

Figure 3.10: Power spectrum of the Rabi flops

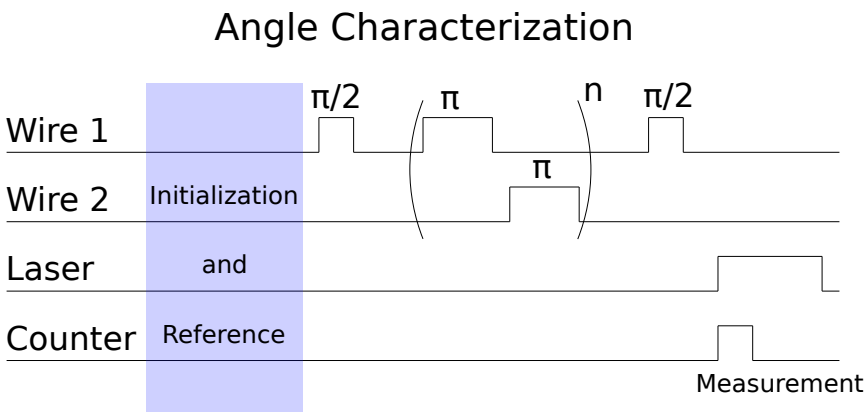

Figure 3.11: Pulse diagram of the Discrete Ramsey Experiment.
After a sequence of initialization done as in section 1.4.1, a series of π pulses is applied by each wire, which is surrounded by $\pi/2$ pulses by one of the wires to prepare and measure.

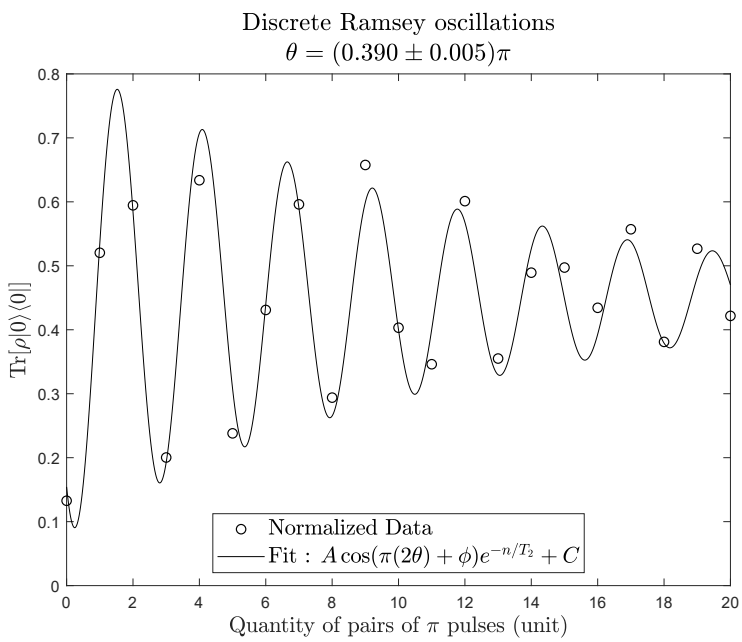

Figure 3.12: Discrete Ramsey experiment repeated 75 million times.

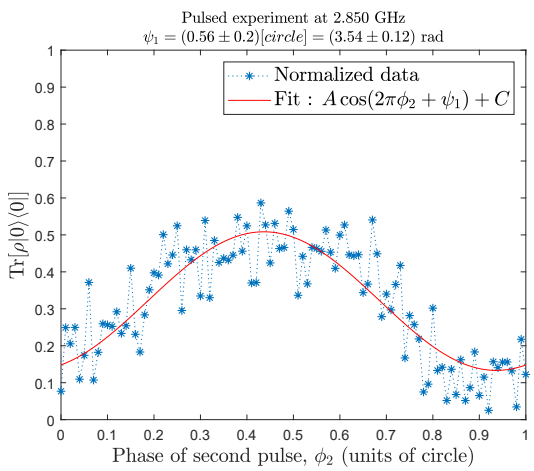

(a) Pi/2 at the low frequency

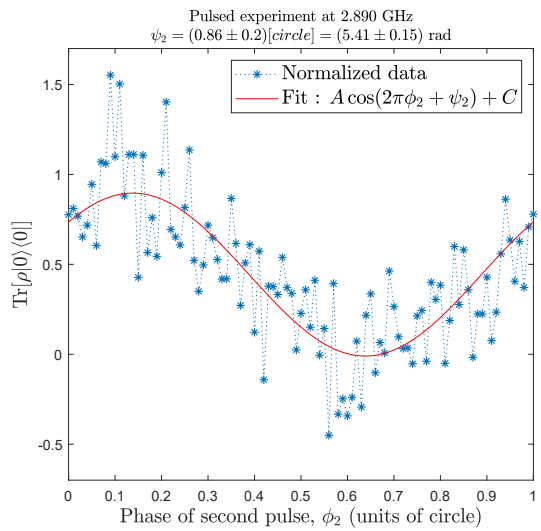

(b) Pi/2 at the higher frequency

Figure 3.13: Evolution of the population of $|0\rangle$ as the two $\pi/2$ pulses get in and out of alignment.

Notice the different scale for the vertical axis.

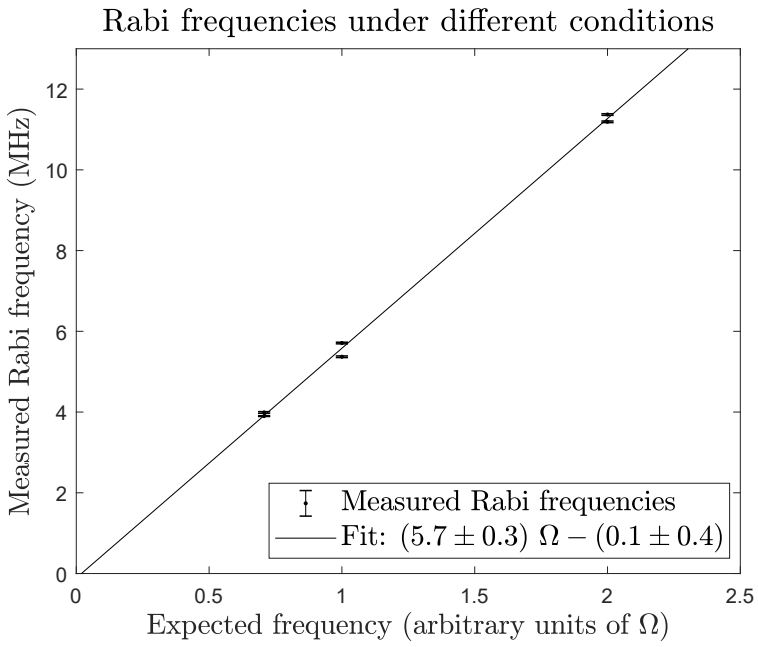

Figure 3.14: An expected frequency of 1Ω corresponds to a single transition under a magnetic field. Expected ratios are treated in section 3.1 and summarized in table 3.5

Chapter 4

Improvements on the current design

4.1 Current issues

While each experiment was conducted successfully, one central aspect of the circuit was neglected, leading to unreliable data. Since we are using microwaves with frequencies around 3 GHZ, the corresponding wavelength is about 10 cm. In order for each signal to remain in phase, it is then imperative that both sections of the circuit have the same length, to much less than 10cm of difference. This is even more important when working with different frequencies, since the phase different changes with the electrical length difference.

In a simple example, in a wire where the electric signal would travel at constant speed, the current can be described with a planar wave equation:

$$I(x,t) = Ae^{-i(\omega t + kx)} \tag{4.1}$$

where I is the current, x and t are the position along the wire and the time respectively, A is the amplitude and ω and k are the constant angular frequency and wave number respectively. The phase of the planar wave is then the argument of the exponential. If k is unknown, it is then convenient, for a given angular frequency, to express the (electrical) length of the wire in terms of phase. Similarly, for a given wire with a fixed length, using different frequencies generates different phases in the signal. The situation at hand is then one where there are two wires of different lengths that are used to carry microwaves at different frequencies.

This had been neglected when the current setup was assembled, leading to each half of the circuit exhibiting vastly different electrical lengths. For the current experiments, this

means that the phase difference between the signals, which is set at the AWG, picks up an additional quantity depending at which frequency the experiment is conducted.

Consequently, when we conducted the phase-phase experiment, the phase difference we measured was also frequency dependent. In the ideal case, for equal electrical length, the phase difference depends on the phase of the first signal (ϕ_1), the phase of the second signal (ϕ_2) and the angle between the microwave sources (θ), each independent of frequency. In our real case, for different electrical length, the phase difference is now a function of $\phi_1(\omega)$, $\phi_2(\omega)$ and θ.

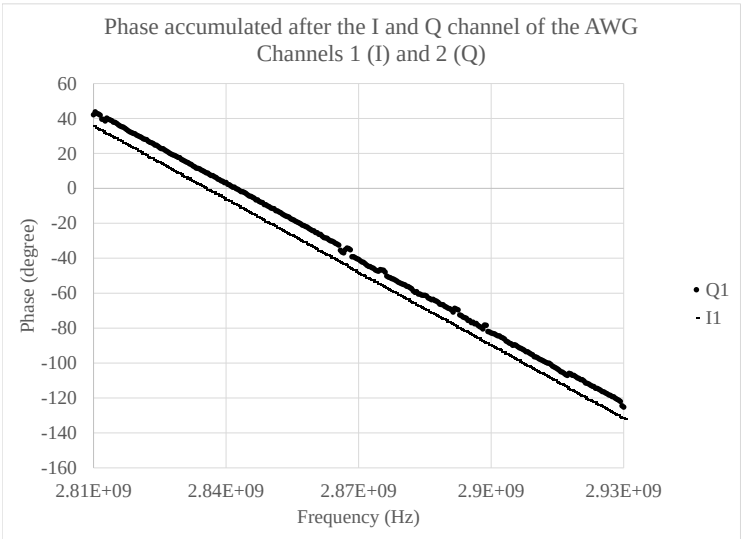

Figure 4.1: Phase accumulated in the wires from the channels 1 and 2 of the AWG (I and Q) to the mixer

To support this idea, we measured the accumulated phase at different frequencies with the help of a network analyzer. Specifically, we measured the phase accumulated from the I and Q channels of the AWG to the mixer and from the mixer to the sample board. Figures 4.1 and 4.2 show that the phase difference between I and Q is very similar across all frequencies for both sources; they can be kept as is[1]. Figure 4.3 shows that the phase

[1]Fitting a linear slope on the accumulated phase as a function of the frequency, the electrical length can be computed as 83 cm, longer than the 60 cm of physical length and giving a velocity factor of 0.72 c.

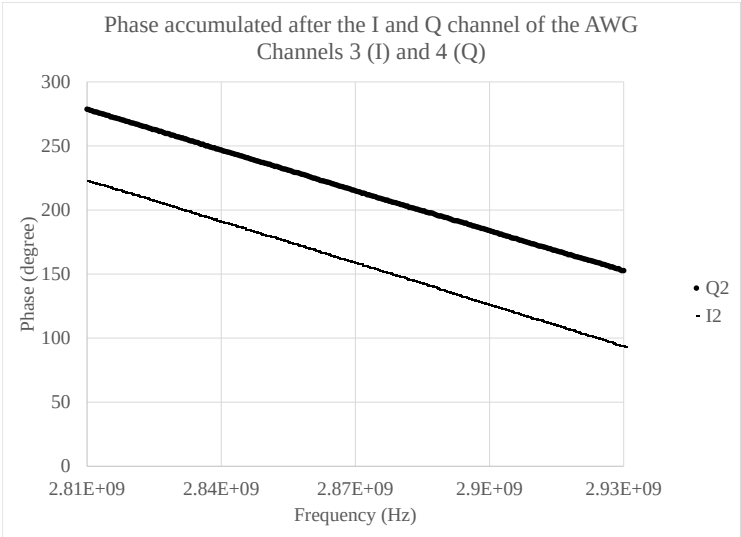

Figure 4.2: Electrical length of the wires from the channels 3 and 4 of the AWG (I and Q) to the mixer

difference between each half of the circuit beyond the mixer until the sample board is very different across the frequency range we have been using (2.82 GHz to 2.92 GHz)[2]. They will need to be replaced and immobilized by means of a solid box or secure attachments so that they display a much more constant phase difference and robustly do so.

Once the circuit itself is symmetric, one can turn their attention to the circuit board, which is not symmetric with respect to the electrical length.

4.2 Proposition for a new sample board

In order to ensure that the circuit is as symmetric as possible, we should update the design of the sample board. The current setup looks symmetric but a quick inspection reveals that the electrical length of each line is different, the path from SMA IN 1 to SMA OUT 1

[2]This time, the electrical length of the first cable can be computed to be 7.2 m while the second cable is 3.4 m

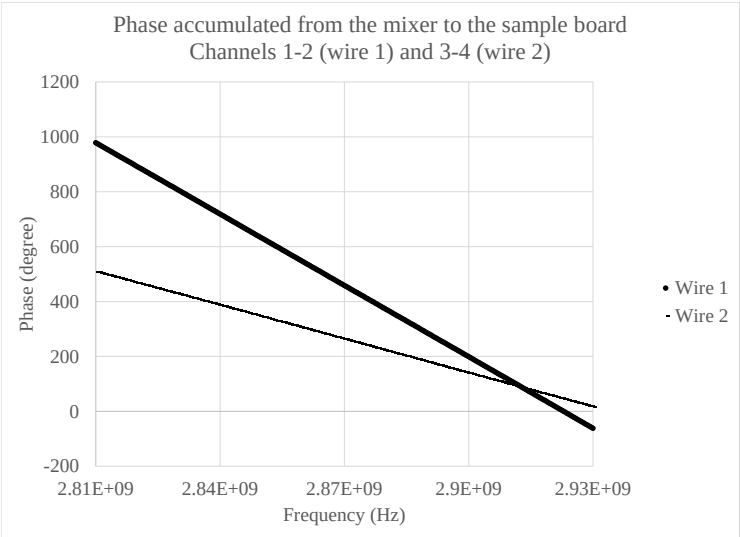

Figure 4.3: Electrical length of the wires from the mixers 1 and 2 to the input of the sample board

is longer that the path from SMA IN 2 to SMA OUT 2. A simple update could be to rotate the section where the wires are close together and prevent the wires from crossing the axe of symmetry, connecting the each input to the end of the wire further from the edge where the SMA connectors lie and the output to the close end of the wire. As a quick example, without care of dimensions or consideration for sharp edges or resonance properties of the sample board, one could make a sample holder as the one on figure 4.4b.

From working with the current setup, I would like to suggest another modification: the spacing between the SMA connectors. As it is currently, all four ports are quite close together on a single edge and tightening SMA cables to their port can be a frustrating endeavour. A solution to this could be to make the new sample board longer such that it hangs further out on the stage on which it rests. This would allow the SMA connectors to be installed on three edges instead of one, increasing the spacing between the connectors, making it easier to install and uninstall the sample holder, to clean it for instance.

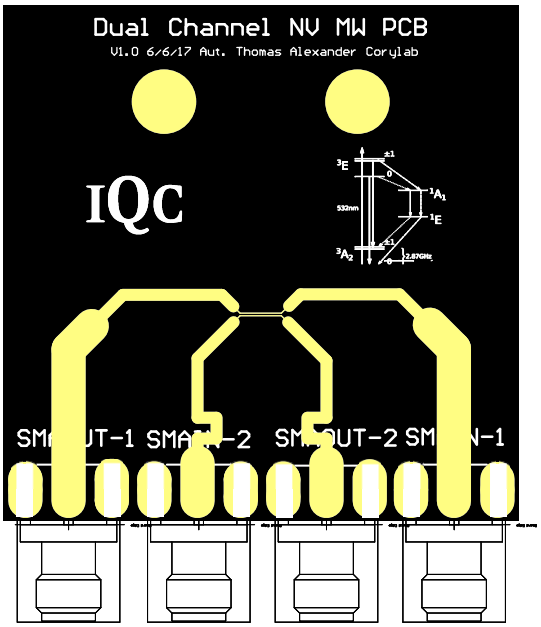

(a) Diagram of the current sample holder

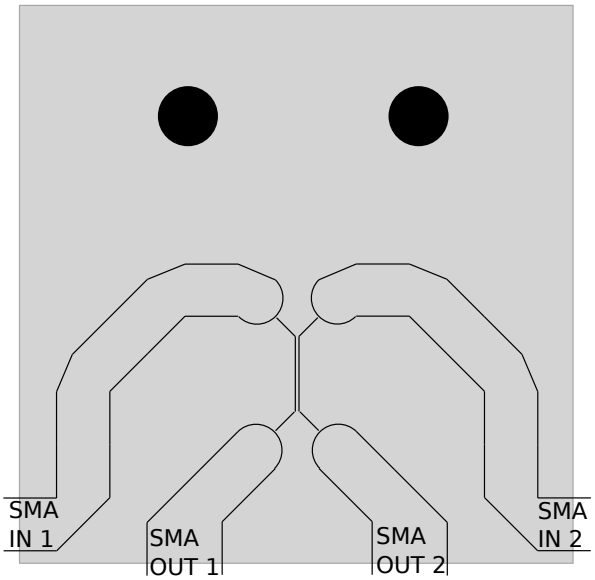

(b) Diagram of the new sample holder

Figure 4.4: Current and suggested PCB sample holders.

4.3 Improvement for the magnet

With the current setup, we use a bar magnet to produce a permanent magnetic field at the site of the NV center. The bar magnet is placed arbitrarily on a stage, which has a range of motion of an inch in each three directions. The calibration of the position of the magnet with respect to the NV center is done by measuring, with an NV center, the field produced by moving the stage at several locations. Using software previously developed, we then find the NV center orientation, its potential rotation from the lab frame and its distance between the NV center and the magnet numerically, with a least square fitting method. In turn, these values are used to compute the position of the magnet to produce a field along the Principal Axis of the NV center, with splitting of 0 to 100 MHz. Given the limited range of motion of the stage and the geometry of the NV center, it is likely that for some orientations of NV center, the magnet cannot be placed to produce a field in its $\hat{z}$ direction only, with large enough splittings.

If future experiments still require the ability to change from a high field to a low field

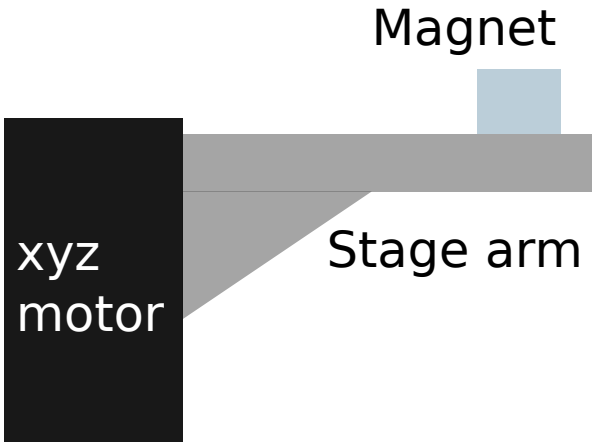

(a) Diagram of the current setup to hold and move the magnet.

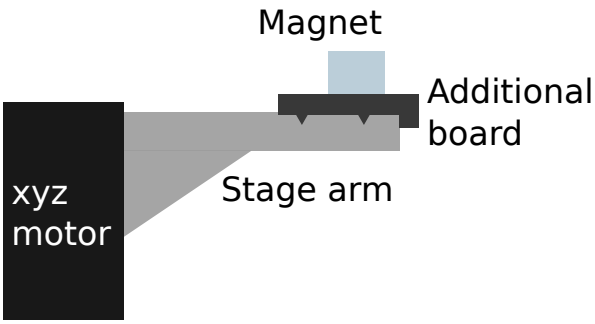

(b) Diagram for a suggested magnet holder, with additional board to easily mount and dismount the magnet whenever necessary.

Figure 4.5: Current and suggested magnet holders.

with a bar magnet, we suggest to modify the setup slightly to allow the magnet to be taken away and placed back at the exact same location. This could be as simple as a little board with hooks on the sides to rest on the stage, going back to the same location every time, as seen on the diagram of figure 4.5b. Instead of taping the magnet to the stage as it is currently, the magnet could be attached to the board and the board could be easily put on and off the stage. Naturally, there are more options, such as replacing the stage for another one with much larger motion range, detaching the diamond from its board and re mounting it until the orientation of the NV centers within is desirable, changing the bar magnet by an electromagnet that could be turned off and so on. However, this solution of installing a magnet holder on top of the stage has the advantage of being easy to implement and modify as little as possible to the current setup. The current and suggested setups can be seen in figure 4.5.

Alternatively, one could position a solenoid on the stage arm, which would allow turning on the magnetic field on command as well as controlling its magnitude more gradually.

4.4 Synchronize the devices

In the current setup, the AWG and the frequency synthesizer are each operating with their own internal clock. This offers two potential problems: they might have slightly

different frequencies and accumulate phase difference over time and there is no guarantee that they are in phase, leading to a phase difference at the beginning of each experiment. The frequency generated by the Synthesizer is used to generated the ≈2.87 GHz carrier frequency and is split before the I/Q mixers, which are triggered by the AWG to generate the envelope of the signal, square in all our experiments. If this causes a phase difference, this will trickle down the rotating wave approximation as an offset of the reference in the rotating frame. If there is only one microwave source, this is irrelevant as the reference can be defined arbitrarily, but in the case of two microwave sources, especially when dealing with multiple NV center orientations at once, this is important.

To improve this situation, one of the devices should be set as a reference clock, which can be used by the other. Since the AWG has a vast library of functions and is easier to program than the Synthesizer, it is easier to control its reference input, that is the Synthesizer will serve as the reference (outputting a signal) while the AWG will be timed on this signal.

At factory default, the Synthesizer will output a 10 MHz signal from its REF OUT port, not to be confused with the RF OUT port which provides the requested ≈ 2.87 GHz. This can then be connected to the AWG, via its Reference Clock Input. Finally, a few commands need to be executed on the AWG to specify the new eternal source as the clock source. The details of the command lines to execute are in Appendix F.

Chapter 5

Extension to ensemble control

We demonstrated that two microwave sources can be characterized to control a single NV center by controlling the microwave field at its site. In the next section, we will propose that homogeneous fields across the whole sample can allow the control of ensembles of NV centers with the same orientation at once and even take into account the NV centers of other orientations.

Since we are now dealing with different NV center orientations, we will need to be more careful with the orientation of each NV center and keep track of frame transformations between the lab frame and each NV center frame. Since the only axis that is intrinsic to the NV center frame is its $\hat{z}$ axis, changing frames, from the lab frame to a NV center frame, can be done with any rotation effecting the $\hat{z}$ axis, and there are infinitely many of such rotations. Without looking too far, one simple way to rotate the $\hat{z}$ axis from one frame to the other is to execute a rotation of the angle between the two $\hat{z}$ axes (using the dot product) about their cross product. Since the NV centers are all in a crystal structure, we will break down this frame transformation in two steps. The first transformation maps the lab frame to the crystal frame, which depends on the cut of the diamond, and the second transformation maps the crystal frame to each of the NV centers, which is the same regardless of the crystal cut.

For example, regarding the first transformation, the $\langle 1\,1\,1 \rangle$ diamond cut will have its $\hat{z}$ axis along $\vec{u}_{111} = \frac{1}{\sqrt{3}}(1,1,1)$ and the frame transformation between the lab frame and the crystal frame will be $R_{lc} = R_{\vec{v}_{lc}}(\theta_{lc})$ such that the rotation is applied about the vector $\vec{v}_{lc} = \hat{z} \times \vec{u}_{111} = \frac{1}{\sqrt{3}}(-1,1,0)$ and by an angle $\theta_{lc} = \arccos(\hat{z} \cdot \vec{u}_{111}) = \arccos(1/\sqrt{3})$ where l is associated with the lab frame and c is associated with the crystal frame.

Regarding the second transformation, within a crystal frame, the NV centers will be

Direction	Rotation angle θ_i	Rotation vector $\vec{v}_i$
NV_1: $\vec{u}_1$	$\theta_1 = \arccos\left(1/\sqrt{3}\right)$	$\vec{v}_1 = 1/\sqrt{2}\ (-1, 1, 0)$
NV_2: $\vec{u}_2$	$\theta_2 = \arccos\left(1/\sqrt{3}\right)$	$\vec{v}_2 = 1/\sqrt{2}\ (1, 1, 0)$
NV_3: $\vec{u}_3$	$\theta_3 = \arccos\left(-1/\sqrt{3}\right)$	$\vec{v}_3 = 1/\sqrt{2}\ (-1, -1, 0)$
NV_4: $\vec{u}_4$	$\theta_4 = \arccos\left(-1/\sqrt{3}\right)$	$\vec{v}_4 = 1/\sqrt{2}\ (1, -1, 0)$

Table 5.1: Frame transformation between the crystal frame and each NV center frame

distributed along $\vec{u}_1 = \frac{1}{\sqrt{3}}(1,1,1)$, $\vec{u}_2 = \frac{1}{\sqrt{3}}(1,-1,-1)$, $\vec{u}_3 = \frac{1}{\sqrt{3}}(-1,1,-1)$ and $\vec{u}_4 = \frac{1}{\sqrt{3}}(-1,-1,1)$. The rotation between the crystal frame and each of the NV center frames labeled with i is then always the same: $R_{\vec{v}_i}(\theta_i)$ where $\vec{v}_i = \hat{z} \times \vec{u}_i$ is angle of rotation and $\theta_i = \arccos\left(\hat{z} \cdot \vec{u}_i\right)$ is the angle of rotation. For an explicit list, see table 5.1

Using these two frame transformations in succession, we then have a tool to express the fields that are produced in the laboratory frame in each NV center frame and then find the effect of a given Hamiltonian on each of these orientations. Assuming that the microwave sources are perpendicular in the laboratory frame, the control Hamiltonian is

$$H_{ctrl} = \Omega_1 \cos\left(\omega t + \phi_1\right) S_x + \Omega_2 \cos\left(\omega t + \phi_2\right) S_y$$

We can express this Hamiltonian in the frame of each of the 4 NV centers:

$$H^i_{ctrl} = \Omega_1 \cos\left(\omega t + \phi_1\right) R_{\vec{v}_i}(\theta_i) \cdot R_{lc} \cdot S_x + \Omega_2 \cos\left(\omega t + \phi_2\right) R_{\vec{v}_i}(\theta_i) \cdot R_{lc} \cdot S_y$$

where $R_{\vec{v}_i}(\theta_i)$ is a rotation about the vector $\vec{v}_i$ by an angle θ_i, defined in table 5.1. For instance, using the $\langle 1\,1\,1 \rangle$ defined diamond cut, $\hat{x}$ and $\hat{y}$ would now be expressed in multiple directions, as expressed in table 5.2.

Finally, we will reuse equations 1.26 to 1.32 to express the Hamiltonian, from the lab frame, in the rotating frame of each NV center. Terms will be collected by their factor $\Omega_i f(\phi_i)$ where i is 1 or 2; the index of the microwave source and f is cos or sin; the trigonometric function of ϕ_i. An example is given in table 5.3.

Once the control fields are expressed in the frames of each of the four NV center orientations, we have the tools required to use a GRadient Ascneding Pulse Engineering (GRAPE) algorithm to design the pulse of interest. In the lab frame, we have control over Ω_1, Ω_2, ϕ_1 and ϕ_2, which can vary between maximal values of $\Omega \in [-\Omega_{max}, \Omega_{max}]$ and $\phi \in [0, 2\pi]$, where Ω (or ϕ) are used to denote either Ω_1 (or ϕ_1) or Ω_2 (or ϕ_2) and where Ω_{max} is the maximal amplitude one can provide. In our case, we set Ω_{max} at 5 MHz, which is close to the experimental values we reached in chapter 3. Additionally, we

NV center frame and direction	$R_{\vec{v}_i}(\theta_i) \cdot R_{lc} \cdot \hat{x}$	$R_{\vec{v}_i}(\theta_i) \cdot R_{lc} \cdot \hat{y}$
$\mathrm{NV}_1 : \vec{u}_1$	$\left(\frac{3+\sqrt{3}}{6}, \frac{-3+\sqrt{3}}{6}, -\frac{\sqrt{3}}{3}\right)$	$\left(\frac{-3+\sqrt{3}}{6}, \frac{3+\sqrt{3}}{6}, -\frac{\sqrt{3}}{3}\right)$
$\mathrm{NV}_2 : \vec{u}_2$	$\left(\frac{3-\sqrt{3}}{6}, \frac{3+\sqrt{3}}{6}, -\frac{\sqrt{3}}{3}\right)$	$\left(\frac{3+\sqrt{3}}{6}, \frac{3-\sqrt{3}}{6}, \frac{\sqrt{3}}{3}\right)$
$\mathrm{NV}_3 : \vec{u}_3$	$\left(\frac{3-\sqrt{3}}{6}, \frac{3+\sqrt{3}}{6}, \frac{\sqrt{3}}{3}\right)$	$\left(\frac{3+\sqrt{3}}{6}, \frac{3-\sqrt{3}}{6}, -\frac{\sqrt{3}}{3}\right)$
$\mathrm{NV}_4 : \vec{u}_4$	$\left(\frac{3+\sqrt{3}}{6}, \frac{-3+\sqrt{3}}{6}, \frac{\sqrt{3}}{3}\right)$	$\left(\frac{-3+\sqrt{3}}{6}, \frac{3+\sqrt{3}}{6}, \frac{\sqrt{3}}{3}\right)$

Table 5.2: Unit vectors of the laboratory frame expressed in NV center frames

Independent variable (Amplitude)	Operator
$\Omega_1 \cos(\phi_1)$	$1/12\Big((3+\sqrt{3})S_x + (-3+\sqrt{3})S_y\Big)$
$\Omega_1 \sin(\phi_1)$	$-1/12\Big((-3+\sqrt{3})S'_x + (3+\sqrt{3})S'_y\Big)$
$\Omega_2 \cos(\phi_2)$	$1/12\Big((-3+\sqrt{3})S_x + (3+\sqrt{3})S_y\Big)$
$\Omega_2 \sin(\phi_2)$	$-1/12\Big((3+\sqrt{3})S'_x + (-3+\sqrt{3})S'_y\Big)$

Table 5.3: Amplitudes of each operator in the frame of the $(1,1,1)$ NV center in the $\langle 1\,1\,1\rangle$ diamond cut

will restrict the range of ϕ_1 and ϕ_2 such that their image will be virtually independent: $\cos(\phi_1), \sin(\phi_1) \in [-1/\sqrt{2}, 1/\sqrt{2}]$. This additional step is not necessary but simplifies the simulation by making the coefficients of each control Hamiltonian dependent on linear functions of $\cos(\phi)$ (and $\sin(\phi)$) instead of dependent on trigonometric functions of ϕ. Given this set of parameter ranges, the internal Hamiltonian, the control Hamiltonians described earlier, the target unitary and an initial pulse sequence chosen randomly, the algorithm incrementally improves the pulse sequence until the final pulse sequence approaches the target unitary. For demonstration, the unitary we want to apply is to apply the same pulse on all NV centers, a $\pi/2$ rotation by S_x^+. The last step is to transform back the solutions given by the simulation into values for Ω_1, Ω_2, ϕ_1 and ϕ_2. This will easily be done by solving the system of four equations and four unknown at each time step.

As an example, using the previously mentioned control Hamiltonians, a randomly generated pulse sequence as the seed of the pulse engineering, and 100 steps of 10 ns, we find a solution that offers the unitary of interest, within a global phase, with a fidelity of 0.999, using the Frobenius distance for this metric. Plots can be found in figure 5.1. The Frobenius distance is defined as:

$$||U - V||_F^2 = \mathrm{Tr}\{(U - V)(U - V)^\dagger\} \tag{5.1}$$

$$= ||U||_F^2 + ||V||_F^2 + \mathrm{Tr}\{UV^\dagger\} - \mathrm{Tr}\{VU^\dagger\} \tag{5.2}$$

$$= 2d^2 - 2\,\mathrm{Re}\{\mathrm{Tr}\{UV^\dagger\}\} \tag{5.3}$$

Where U and V are the unitaries to compare and d is the dimension of the unitaries, 3 in this case.

Few more considerations need to be taken into account for these simulations. First, using a $\langle 1\,1\,1 \rangle$ diamond, we made sure that the microwave fields in each NV center frame were not co-planar with the PAS. If that was the case, using the first microwave source to define the $\hat{x}$ direction as done previously, each control Hamiltonian would only have contribution of S_x and S_z, lacking the necessary S_y. In the lab frame, this can be seen if the PAS of any NV center is in the vector space spanned by the vector fields of the two microwave sources.

Furthermore, two NV center orientations can't have the same coefficients for their control Hamiltonians. This would come up if the vectors describing the fields from both microwave source lied in the plane of symmetry between PAS from two NV centers. In that case, two NV centers would have similar coefficients for their control Hamiltonian. The coefficients in $\hat{x}$ and $\hat{y}$ would be the same and only the sign of the $\hat{z}$ coefficient would be

different and unless the microwave couplings are of the order of the ZFS (which is not the case in this experiment; the microwave coupling is about 5 MHz while the ZFS is about 3 GHz), that difference will be negligible, they can be suppressed during the RWA.

Beyond these geometric edge cases to keep an eye out for, other orientations of diamond will be adequate to perform arbitrary unitaries on each of the NV centers individually.

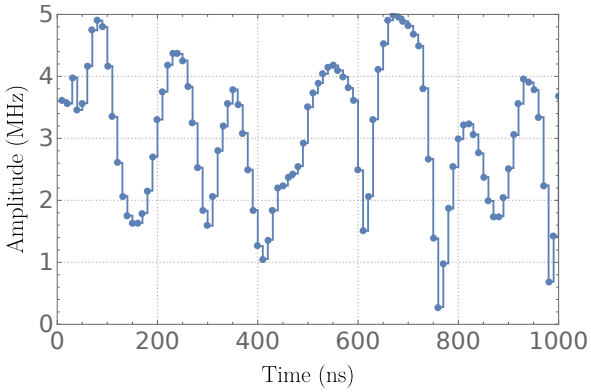

(a) Step-wise time independent evolution of the amplitude of Ω_1

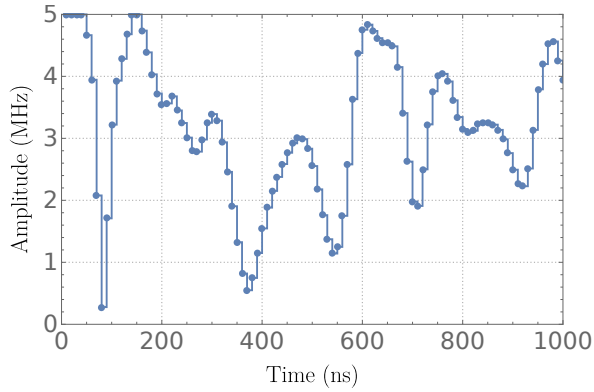

(b) Step-wise time independent evolution of the amplitude of Ω_2

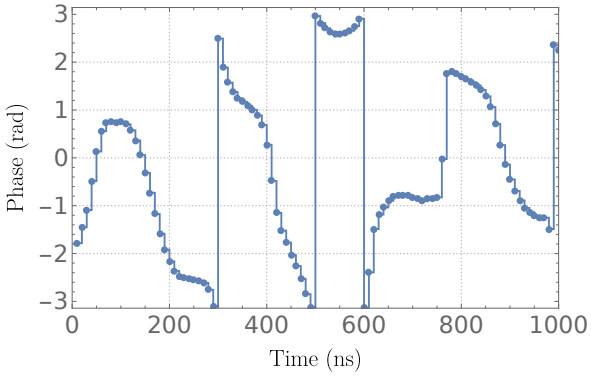

(c) Step-wise time independent evolution of the amplitude of ϕ_1

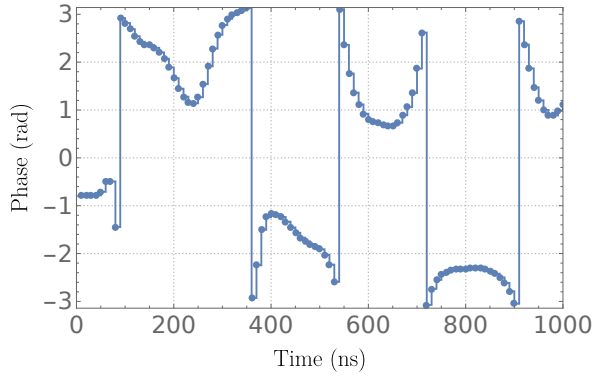

(d) Step-wise time independent evolution of the amplitude of ϕ_2

Figure 5.1: Example of pulse sequence producing a $\pi/2$ rotation about S_x^+ for each NV center orientation.

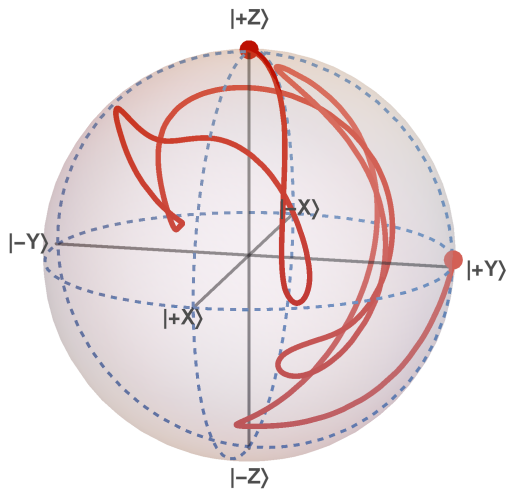

(a) Bloch Sphere trajectory for NV1

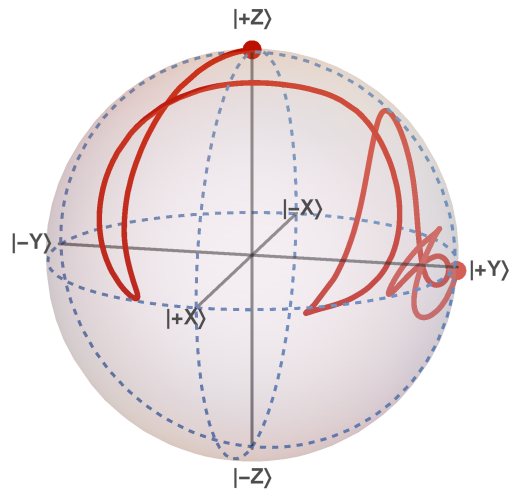

(b) Bloch Sphere trajectory for NV2

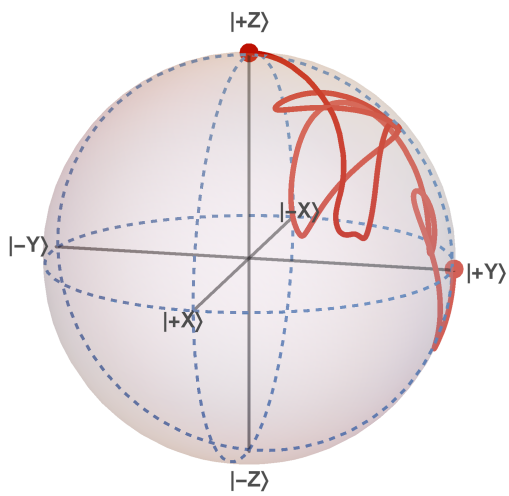

(c) Bloch Sphere trajectory for NV3

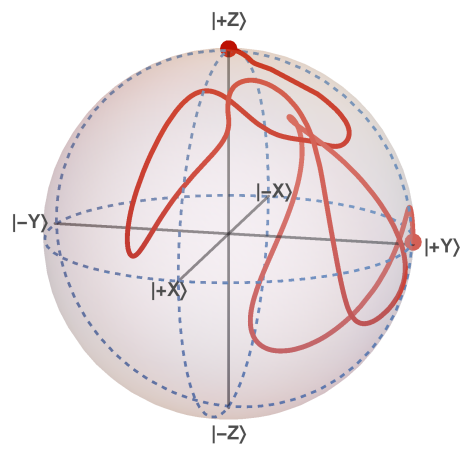

(d) Bloch Sphere trajectory for NV4

Figure 5.2: Trajectories in a Bloch Sphere representation as per our simulation. Given that NV center are spin-1 objects and can't be represented in a Bloch Sphere, we are here focusing on the subspace spanned by $|0\rangle$ and $|1\rangle$. We have $|+Z\rangle = |0\rangle$, $|-Z\rangle = |+1\rangle$, $|+X\rangle = \frac{|0\rangle+|1\rangle}{\sqrt{2}}$, $|-X\rangle = \frac{|0\rangle-|1\rangle}{\sqrt{2}}$, $|+Y\rangle = \frac{|0\rangle+i|1\rangle}{\sqrt{2}}$, $|-Y\rangle = \frac{|0\rangle-i|1\rangle}{\sqrt{2}}$.

Conclusion

This thesis saw the development of new techniques to characterize two microwave sources as seen by an NV center. With these techniques, one can reliably measure the power of their microwave sources in the frame of the NV center as well as measuring the angle between the projection of each source in this frame. With this information, we demonstrated how one can adjust the relative power and the phase between the sources to generate circularly polarized pulses that carry angular momentum, able to target specific transitions between the $m_s = 0$ level of the NV center to only one other level, suppressing transitions to the third level. This is especially useful when we consider NV centers in the absence of a magnetic field, where linearly polarized microwaves would fail to distinguish between the $m_s = -1$ and $m_s = 1$ states, which are degenerate. Finally, with this techniques to control any orientation of NV centers located in a volume larger than demonstrated previously [3], the next step on which one can focus their attention is to control ensembles of NV centers by means of pulse sequences to target each orientation separately, generating independent unitaries for each.

In addition to these novel techniques, we covered the maintenance of the confocal microscope used to perform ODMR on a single NV center, its improvement to work with this new setup requiring two microwave sources as well as the steps we took to optimize it. Similarly, the electric circuit underwent a significant improvement to support the addition of another microwave source, which came with a delicate update of the software, custom built, that controls the whole apparatus.

We have reviewed each section of the optical table and covered the metrics used to confirm its rightful operation, from the laser source to the avalanche photo diode, going through the acousto-optic modulator, the mode shaping arm, the telescope and the objective. We have thus emphasized on the maintenance of the optic table as the first step to enable the spin experiments to come to fruition.

References

[1] Thiago P. Mayer Alegre, Charles Santori, Gilberto Medeiros-Ribeiro, and Raymond G. Beausoleil. Polarization-selective excitation of nitrogen vacancy centers in diamond. *Phys. Rev. B*, 76:165205, Oct 2007. doi: 10.1103/PhysRevB.76.165205. URL https://link.aps.org/doi/10.1103/PhysRevB.76.165205.

[2] T. P. Mayer Alegre, A. C. Torrezan, and G. Medeiros-Ribeiro. Microstrip resonator for microwaves with controllable polarization. *Applied Physics Letters*, 91(20):204103, 2007. doi: 10.1063/1.2809372. URL https://doi.org/10.1063/1.2809372.

[3] M. Mrzek, J. Mlynarczyk, D. S. Rudnicki, and W. Gawlik. Circularly polarized microwaves for magnetic resonance study in the ghz range: Application to nitrogen-vacancy in diamonds. *Applied Physics Letters*, 107(1):013505, 2015. doi: 10.1063/1.4923252. URL https://doi.org/10.1063/1.4923252.

[4] C. A. Ryan, J. S. Hodges, and D. G. Cory. Robust decoupling techniques to extend quantum coherence in diamond. *Phys. Rev. Lett.*, 105:200402, Nov 2010. doi: 10.1103/PhysRevLett.105.200402. URL https://link.aps.org/doi/10.1103/PhysRevLett.105.200402.

[5] Gopalakrishnan Balasubramanian, Philipp Neumann, Daniel Twitchen, Matthew Markham, Roman Kolesov, Norikazu Mizuochi, Junichi Isoya, Jocelyn Achard, Johannes Beck, Julia Tissler, Vincent Jacques, Philip R. Hemmer, Fedor Jelezko, and Jörg Wrachtrup. Ultralong spin coherence time in isotopically engineered diamond. *Nature Materials*, 8:383 EP –, Apr 2009. URL https://doi.org/10.1038/nmat2420.

[6] A. Gruber, A. Drbenstedt, C. Tietz, L. Fleury, J. Wrachtrup, and C. von Borczyskowski. Scanning confocal optical microscopy and magnetic resonance on single defect centers. *Science*, 276(5321):2012–2014, 1997. ISSN 00368075, 10959203. URL http://www.jstor.org/stable/2892971.

[7] J Harrison, M.J Sellars, and N.B Manson. Optical spin polarisation of the n-v centre in diamond. *Journal of Luminescence*, 107(1):245 – 248, 2004. ISSN 0022-2313. doi: https://doi.org/10.1016/j.jlumin.2003.12.020. URL http://www.sciencedirect.com/science/article/pii/S0022231303001972. Proceedings of the 8th International Meeting on Hole Burning, Single Molecule, and Related Spectroscopies: Science and Applications.

[8] N. Bar-Gill, L. M. Pham, A. Jarmola, D. Budker, and R. L. Walsworth. Solid-state electronic spin coherence time approaching one second. *Nature Communications*, 4: 1743 EP –, Apr 2013. URL https://doi.org/10.1038/ncomms2771. Article.

[9] J. M. Boss, K. S. Cujia, J. Zopes, and C. L. Degen. Quantum sensing with arbitrary frequency resolution. *Science*, 356(6340):837–840, 2017. ISSN 0036-8075. doi: 10.1126/science.aam7009. URL https://science.sciencemag.org/content/356/6340/837.

[10] L Rondin, J-P Tetienne, T Hingant, J-F Roch, P Maletinsky, and V Jacques. Magnetometry with nitrogen-vacancy defects in diamond. *Reports on Progress in Physics*, 77(5):056503, may 2014. doi: 10.1088/0034-4885/77/5/056503. URL https://doi.org/10.1088%2F0034-4885%2F77%2F5%2F056503.

[11] S. Steinert, F. Dolde, P. Neumann, A. Aird, B. Naydenov, G. Balasubramanian, F. Jelezko, and J. Wrachtrup. High sensitivity magnetic imaging using an array of spins in diamond. *Review of Scientific Instruments*, 81(4):043705, 2010. doi: 10.1063/1.3385689. URL https://doi.org/10.1063/1.3385689.

[12] D. Le Sage, K. Arai, D. R. Glenn, S. J. DeVience, L. M. Pham, L. Rahn-Lee, M. D. Lukin, A. Yacoby, A. Komeili, and R. L. Walsworth. Optical magnetic imaging of living cells. *Nature*, 496(7446):486–489, Apr 2013. ISSN 1476-4687. doi: 10.1038/nature12072. URL https://www.ncbi.nlm.nih.gov/pubmed/23619694. 23619694[pmid].

[13] L M Pham, D Le Sage, P L Stanwix, T K Yeung, D Glenn, A Trifonov, P Cappellaro, P R Hemmer, M D Lukin, H Park, A Yacoby, and R L Walsworth. Magnetic field imaging with nitrogen-vacancy ensembles. *New Journal of Physics*, 13(4):045021, apr 2011. doi: 10.1088/1367-2630/13/4/045021. URL https://doi.org/10.1088%2F1367-2630%2F13%2F4%2F045021.

[14] V. M. Acosta, E. Bauch, M. P. Ledbetter, A. Waxman, L.-S. Bouchard, and D. Budker. Temperature dependence of the nitrogen-vacancy magnetic resonance in diamond.

Phys. Rev. Lett., 104:070801, Feb 2010. doi: 10.1103/PhysRevLett.104.070801. URL https://link.aps.org/doi/10.1103/PhysRevLett.104.070801.

[15] F. Dolde, H. Fedder, M. W. Doherty, T. Nöbauer, F. Rempp, G. Balasubramanian, T. Wolf, F. Reinhard, L. C. L. Hollenberg, F. Jelezko, and J. Wrachtrup. Electric-field sensing using single diamond spins. *Nature Physics*, 7:459 EP –, Apr 2011. URL https://doi.org/10.1038/nphys1969.

[16] G. Kucsko, P. C. Maurer, N. Y. Yao, M. Kubo, H. J. Noh, P. K. Lo, H. Park, and M. D. Lukin. Nanometre-scale thermometry in a living cell. *Nature*, 500:54 EP –, Jul 2013. URL https://doi.org/10.1038/nature12373.

[17] Om Patange. On an instrument for the coherent investigation of nitrogen-vacancy centres in diamond, 2013. URL http://hdl.handle.net/10012/7955.

[18] M W Doherty, J Michl, F Dolde, I Jakobi, P Neumann, N B Manson, and J Wrachtrup. Measuring the defect structure orientation of a single NV- centre in diamond. *New Journal of Physics*, 16(6):063067, jun 2014. doi: 10.1088/1367-2630/16/6/063067. URL https://doi.org/10.1088%2F1367-2630%2F16%2F6%2F063067.

[19] N. B. Manson, J. P. Harrison, and M. J. Sellars. Nitrogen-vacancy center in diamond: Model of the electronic structure and associated dynamics. *Phys. Rev. B*, 74:104303, Sep 2006. doi: 10.1103/PhysRevB.74.104303. URL https://link.aps.org/doi/10.1103/PhysRevB.74.104303.

[20] J. A. Larsson and P. Delaney. Electronic structure of the nitrogen-vacancy center in diamond from first-principles theory. *Phys. Rev. B*, 77:165201, Apr 2008. doi: 10.1103/PhysRevB.77.165201. URL https://link.aps.org/doi/10.1103/PhysRevB.77.165201.

[21] Yoshimi Mita. Change of absorption spectra in type-ib diamond with heavy neutron irradiation. *Phys. Rev. B*, 53:11360–11364, May 1996. doi: 10.1103/PhysRevB.53.11360. URL https://link.aps.org/doi/10.1103/PhysRevB.53.11360.

[22] M. W. Doherty, F. Dolde, H. Fedder, F. Jelezko, J. Wrachtrup, N. B. Manson, and L. C. L. Hollenberg. Theory of the ground-state spin of the nv^- center in diamond. *Phys. Rev. B*, 85:205203, May 2012. doi: 10.1103/PhysRevB.85.205203. URL https://link.aps.org/doi/10.1103/PhysRevB.85.205203.

[23] D.J. Griffiths. *Introduction to Quantum Mechanics*. Cambridge University Press, 2016. ISBN 9781107179868. URL https://books.google.ca/books?id=0h-nDAAAQBAJ.

[24] Marcus W. Doherty, Neil B. Manson, Paul Delaney, Fedor Jelezko, Jrg Wrachtrup, and Lloyd C.L. Hollenberg. The nitrogen-vacancy colour centre in diamond. *Physics Reports*, 528(1):1 – 45, 2013. ISSN 0370-1573. doi: https://doi.org/10.1016/j.physrep.2013.02.001. URL http://www.sciencedirect.com/science/article/pii/S0370157313000562. The nitrogen-vacancy colour centre in diamond.

[25] Hincks, Ian. Exploring practical methodologies for the characterization and control of small quantum systems, 2018. URL http://hdl.handle.net/10012/13711.

[26] M. L. Goldman, A. Sipahigil, M. W. Doherty, N. Y. Yao, S. D. Bennett, M. Markham, D. J. Twitchen, N. B. Manson, A. Kubanek, and M. D. Lukin. Phonon-induced population dynamics and intersystem crossing in nitrogen-vacancy centers. *Phys. Rev. Lett.*, 114:145502, Apr 2015. doi: 10.1103/PhysRevLett.114.145502. URL https://link.aps.org/doi/10.1103/PhysRevLett.114.145502.

[27] Lucio Robledo, Hannes Bernien, Toeno van der Sar, and Ronald Hanson. Spin dynamics in the optical cycle of single nitrogen-vacancy centres in diamond. *New Journal of Physics*, 13(2):025013, feb 2011. doi: 10.1088/1367-2630/13/2/025013. URL https://doi.org/10.1088%2F1367-2630%2F13%2F2%2F025013.

[28] Ian Hincks. nvham, August 2018. URL https://github.com/ihincks/nvham.

[29] Michal Leskes, P.K. Madhu, and Shimon Vega. Floquet theory in solid-state nuclear magnetic resonance. *Progress in Nuclear Magnetic Resonance Spectroscopy*, 57(4):345 – 380, 2010. ISSN 0079-6565. doi: https://doi.org/10.1016/j.pnmrs.2010.06.002. URL http://www.sciencedirect.com/science/article/pii/S0079656510000798.

[30] Richard P. Mildren, James E. Butler, and James R. Rabeau. Cvd-diamond external cavity raman laser at 573 nm. *Opt. Express*, 16(23):18950–18955, Nov 2008. doi: 10.1364/OE.16.018950. URL http://www.opticsexpress.org/abstract.cfm?URI=oe-16-23-18950.

[31] ISO 11146-1:2005. Lasers and laser-related equipment – Test methods for laser beam widths, divergence angles and beam propagation ratios – Part 1: Stigmatic and simple astigmatic beams. Standard, International Organization for Standardization, Geneva, CH, January 2001.

[32] K.-M. C. Fu, C. Santori, P. E. Barclay, and R. G. Beausoleil. Conversion of neutral nitrogen-vacancy centers to negatively charged nitrogen-vacancy centers through selective oxidation. *Applied Physics Letters*, 96(12):121907, 2010. doi: 10.1063/1.3364135. URL https://doi.org/10.1063/1.3364135.

[33] Wang, Zimeng. Probing surface spin interaction dynamics using nitrogen-vacancy center quantum sensors with high-fidelity state-selective transition control, 2017. URL http://hdl.handle.net/10012/12659.

[34] S. Felton, A. M. Edmonds, M. E. Newton, P. M. Martineau, D. Fisher, D. J. Twitchen, and J. M. Baker. Hyperfine interaction in the ground state of the negatively charged nitrogen vacancy center in diamond. *Phys. Rev. B*, 79:075203, Feb 2009. doi: 10.1103/PhysRevB.79.075203. URL https://link.aps.org/doi/10.1103/PhysRevB.79.075203.

[35] ISO 11146-2:2005(E). Lasers and laser-related equipment Test methods for laser beam widths, divergence angles and beam propagation ratios Part 2: General astigmatic beams. Standard, International Organization for Standardization, Geneva, CH, February 2005.

[36] *AWG5000 and AWG7000 Series Arbitrary Waveform Generators Programmer Manual*. Tektronix, Inc., 14150 SW Karl Braun Drive P.O. Box 500 Beaverton, OR 97077 USA, August 2011. Revision A.

Appendices

Appendix A

Introduction to M squares measurement by ISO

If simplicity is not sought, ISO published standard 11146, which recommends sampling 20 points around the beam waist, within at least three generalized Rayleigh lengths to compute the second order moments of the Wigner distribution and to create an artificial beam waist with an aberration-free focusing lens if the beam waist is not easily accessible, for example when it is collimated or focuses far away. The ten second order moments of the Wigner function are: $\langle x^2 \rangle$, $\langle y^2 \rangle$, $\langle xy \rangle$, $\langle \Theta_x^2 \rangle$, $\langle \Theta_y^2 \rangle$, $\langle \Theta_x \Theta_y \rangle$, $\langle x\Theta_x \rangle$, $\langle x\Theta_y \rangle$, $\langle y\Theta_x \rangle$ and $\langle y\Theta_y \rangle$. These second order moments are then used to compute M^2, the invariant quantity related to the focusability of the beam:

$$M_{eff}^2 = \frac{4\pi}{\lambda} \left[\det \begin{pmatrix} \langle x^2 \rangle & \langle xy \rangle & \langle x\Theta_x \rangle & \langle x\Theta_y \rangle \\ \langle xy \rangle & \langle y^2 \rangle & \langle y\Theta_x \rangle & \langle y\Theta_y \rangle \\ \langle x\Theta_x \rangle & \langle y\Theta_x \rangle & \langle \Theta_x^2 \rangle & \langle \Theta_x \Theta_y \rangle \\ \langle x\Theta_y \rangle & \langle y\Theta_y \rangle & \langle \Theta_x \Theta_y \rangle & \langle \Theta_y^2 \rangle \end{pmatrix} \right]^{1/4} \tag{A.1}$$

For more details on how to compute those second order moments, consult ISO 11146-2:2005(E): "Test methods for laser beam widths, divergence angles and beam propagation ratios Part 2: General astigmatic beams"[35].

Appendix B

Choosing a fiber coupler

When choosing a single mode fiber, there are few criteria that need to be considered to achieve sufficiently strong coupling. The first one is the mode of the fiber itself, in this case, the wavelength that is supported. The second is the radius of the beam, both inside and outside of the fiber. The free space beam must be focused to the core of the fiber with an incident angle small enough that the total internal reflection criteria will be respected. Assuming that the two fixed parameters we cannot change are the radius of the beam in free space and the choice of single mode fibers, the free parameter is the focal length of the fiber coupler. On one hand, it can't be too small or the incident angle will be too large and on the other hand, it must be large enough that the free space beam is completely guided into the fiber. For our application, given the spot size of the optical fiber is 3.4 μm and numerical aperture of 0.12, we need a fiber coupler that will have a focal length large enough to produce an incident angle low enough such that

$$f \geq \frac{D}{2\tan\theta_A},$$

where f is the focal length of the fiber coupler, $D = 1.6$ mm is the collimated beam diameter, $\theta_A = \arcsin NA$ is the acceptance angle of the fiber (half angle). This simple calculation gives a lower bound of 6.61 mm. The upper bound of the focal length is given by

$$f \leq \frac{MFD\pi D}{4\lambda},$$

where the Mode Field Diameter (MFD) of the fiber $MFD = 3.4$ μm is the spot size, which is the point where the intensity of the beam falls to $1/e^2 \approx 0.135$ of the maximal intensity. This gives an upper value of 8.8 mm for the focal length. With the current model of the fiber coupler announcing a focal length of 7.86 mm, we are well between the bounds.

Appendix C

Common experimental problems and solutions

C.1 Hard reset of the Micro Stepper and piezo controller

It is not unusual that fails the motorized controllers that move the sample holder and the diamond. In these cases, if restarting Matlab is not sufficient, the steppers themselves need to be reset.

In this case, it is best to exit the Matlab software, disconnect the power of the apt - piezo controller as well as powering off the APT Stepper Motor Controller. Both these devices will be re-powered and reconnected. As resetting the controllers will move the sample holder, the micro-metric screw should be used to move it as far as possible from the microscope objective, to protect all pieces.

The software used for this is the Thorlab APT User. After re-connecting the apt - piezo controller, opening the APT User software should give two cascading windows, in which the position should be reset by clicking Zero. Furthermore, under the Feedback Loop/Loop Mode, the Close Loop option should be switched to Open Loop and confirming the choice.

Next, the APT Stepper Motor Controller can be turned on again and if the APT User displays three more cascading windows for each of the axis, they should all be reset by clicking Home/Zero.

If the controllers crash while an important NV center is sitting under the microscope objective and moving the sample stage means loosing it, it is possible to let go of the

last Home/Zero step. This will shift the origin of the controllers, making it look that the current position is at (0,0,0) instead of the position it held before the crash.

As a last detail, it is good practice to exit and launch the APT User between each step, making sure that the process terminated properly each time.

C.2 Sweeping the phase

In the .pp files, following the Bruker syntax convention, the values given for the phase can only be expressed in reduced fractions, in units of circle. As such, to write out a phase of $\pi/4$, we need to write ph1 = (4) 1 to divide the circle in 4 sections and use the first them.

To try multiple values of ph1 close to that value, we can't use decimal expressions such ph1 = (4) 0.9 or ph1 = (4) 1.1, because they are going to be rounded to 0 and $\pi/4$, respectively. We must instead write ph1 = (40) 9 and ph1 = (40) 11, similar fractions, to get the values we need.

If the phase is the independent variable that is going to be swept, the value saved in the .pp file will be dismissed in favor of the "Sweeps" variable, which will have units of circle. For instance, to sweep ph1 from $\pi/3$ to $5\pi/6$ in 25 points, the parameters to enter are on table C.1.

Parameter	Value
Variable	ph1
Array	(leave empty)
Start	0.333
Stop	0.833
Number of Points	25

Table C.1: Values to provide to the "Sweeps" environment to perform an experiment sweeping ph1 from $\pi/3$ to $5\pi/6$ in 25 steps

C.3 AWG Socket Server protocol

When rebooting, the AWG might go back to its default TekVISA LAN Socket Server protocol. If this happen, it is necessary to switch it back to the AWG software Socket Server protocol. To do so, one must disable the LAN socket and enable the Software socket. Detailed instructions are given in Appendix D

Appendix D

Instructions to reset the AWG Socket Server

This section is a document was provided by Tektronix as an option to restore communication protocols between the laboratory computer and the AWG used.

AWG5k/7k raw sockets

- TekVISA socket server prematurely terminates waveform writes
  - Not a typical use-case for Tektronix oscilloscopes
  - Very much a typical use-case for Tektronix arbitrary waveform generators
- AWG software integrated socket server does not prematurely terminate while writing binary block data
- Resolution:
  - Disable TekVISA socket server
  - Enable AWG software socket server

Disable TekVISA socket server

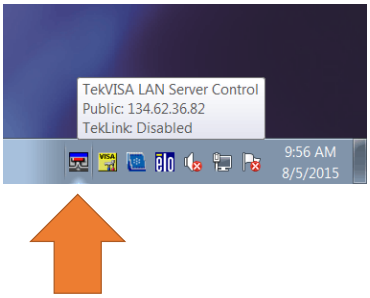

In the system tray notification area of Microsoft Windows, right-click on the TekVISA LAN Server Control icon.

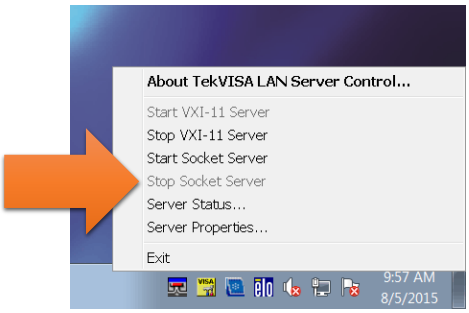

Click on “Stop Socket Server”
If the text is gray (and not black), then the TekVISA Socket Server is not running

Enable AWG software socket server

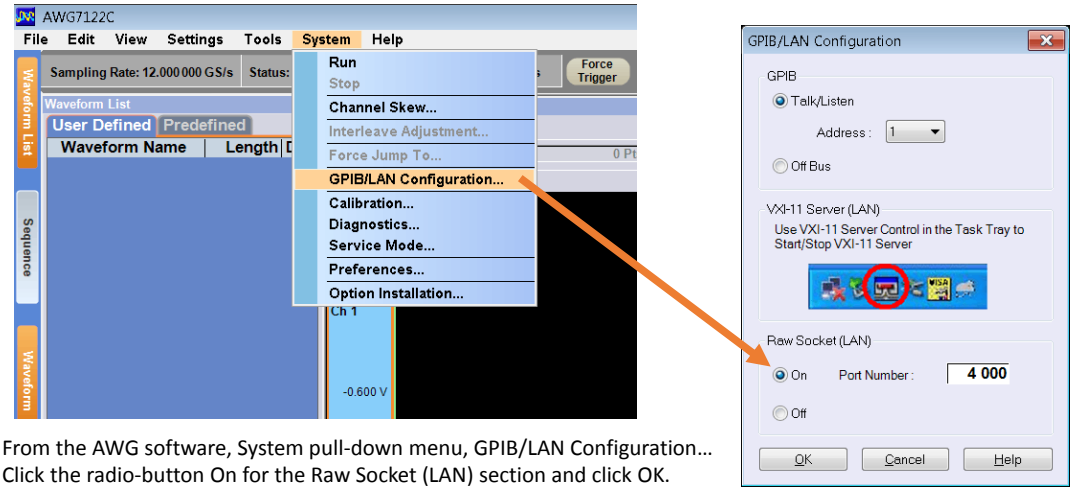

From the AWG software, System pull-down menu, GPIB/LAN Configuration…
Click the radio-button On for the Raw Socket (LAN) section and click OK.

Appendix E

Ad hoc confirmation of microwave control

In this appendix, we establish the basis for Continuous Wave (CW) experiment to calibrate the phase. As were describing in section 3.9.2, one can show that the microwaves are circularly polarized by suppressing one transition, for any field. Or, by restating the situation, after calibrating the relative amplitudes of the microwaves, one can use a series of CW experiments to determine the values of ϕ_2 that enable a suppression.

At fields high enough to justify the qubit approximation, the situation can be reduced to two transitions whose spectrum can be described by the Bloch equations:

$$PL = B.C. - \frac{(B.C. - D.C.)T_2\Omega}{1 + T_2^2\Delta\omega^2 + T_1T_2\Omega^2} \tag{E.1}$$

Where PL stands for the Photo Luminescence, $B.C.$ is the Bright Counts, $D.C.$ is the Dark Counts, Ω is the amplitude of the microwaves, T_1 and T_2 are the longitudinal and transverse relaxation times and $\Delta\omega$ is the de-tuning.

At fields too low to justify this approximation, the spectrum becomes more complex and asks for a generalization of the Bloch Equations for spin-1 NV center. Looking at this situation, we conducted the sus-mentioned experiment; fixing the amplitudes $\Omega_1 = \Omega_2 = \Omega$ with a Rabi experiment, we fixed the phase of the first microwave source $\phi_1 = 0$ and conducted CW experiments while changing the phase ϕ_2 of the second microwave source. Assuming that the 10 MHz splitting we generated was still high enough to justify using Lorentzian functions to describe the spectrum, we plotted the scaling factor of both transitions as a function of the second phase. Assuming that the evolution of the scaling

factor was a sinusoidal function of ϕ_2, we found the values for which the scaling factor is minimal. Using the corresponding values of ϕ_2 as well as the value for which the scaling factors were closest, we produced CW spectra that highlight the suppression of a transition, hence the presence of circularly polarized microwaves. These results are presented in figure E.1. Since the sampling of ϕ_2 was made with a resolution of $\pi/10$, the error value for the values of ϕ_2 is going to be half of that value.

From these values of ϕ_2, similar to section 3.7, one can find the values of θ and ϕ_1. Again, this is assuming that the electrical length is constant for all frequencies. If this was the case and assuming that the previous assumptions are valid, we can find $\theta = \frac{1.86\pi - 0.79\pi}{2} = (0.54 \pm 0.05)\pi$ while $\phi_1 = \frac{1.86\pi + 0.79\pi}{2} = (1.33 \pm 0.05)\pi$. Unsurprisingly, this value of ϕ_1 is very close to the value of ϕ_2 to generate linear polarization.

There are several assumptions that are made with this model which will need to be revisited. First, we assumed that the line shapes would be Lorentzian, which might not be the case at low field. Second, we assumed that the scaling factor was a simple sinusoidal function of the phase but that doesn't have to be the case; an expression closer to 3.3.2 might already have the parameters necessary to describe the fact that the scaling factor doesn't reach zero even when the phase is chosen carefully. Thirdly, we assumed that the resonance would remain centered at the same frequency, whereas simulations of CW experiments using straightforward time dependent evolution suggest that the peak positions are dependent on the phase. Finally, this work still doesn't take into consideration that the electrical length is not constant for all frequencies.

In conclusion, repeating this experiment with more care could explore the physics of Bloch equations for NV centers and enable new methods of confirming the circular nature of the polarization of the microwave sources.

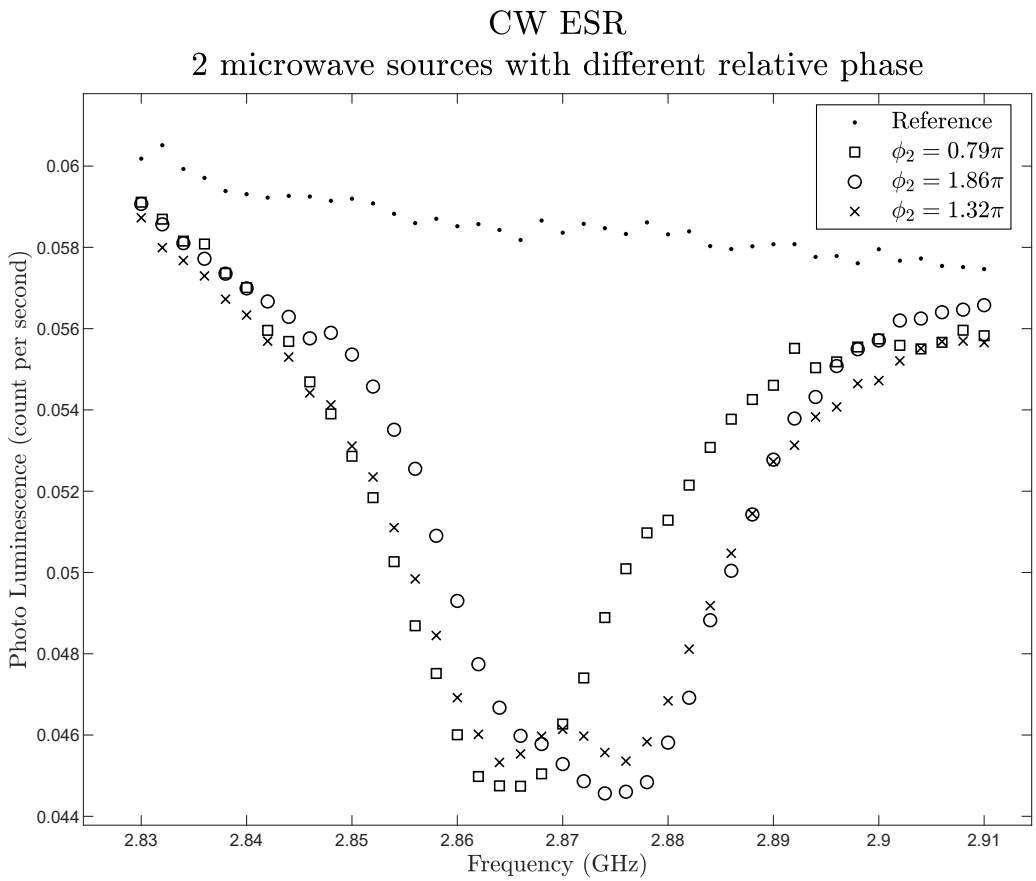

Figure E.1: CW ESR experiment with similar contribution from each wire, $\phi_1 = 0$ and ϕ_2 defined for each curve.

Appendix F

Commands relevant to synchronizing the devices to the same clock

In order for all devices to share a same frequency, we need to use the following instructions. In this list, we offer the general command, from the AWG5000 programmer Manual[36], followed by the specific arguments required in our case.

- `[SOURce[1]]:ROSCillator:SOURce` This command selects the reference oscillator source. INTernal means that the reference frequency is derived from the internal precision oscillator. EXTernal means the reference frequency is derived from an external signal supplied through the Reference Clock Input connector.
  - `SOUR:ROSC:SOUR EXT` The reference frequency is derived from an external signal supplied through the reference clock input.
- `AWGControl:CLOCk:SOURce` This command and query sets or returns the clock source. When the clock source is internal, the arbitrary waveform generator's internal clock is used to generate the clock signal. If the clock source is external, the clock signal from an external oscillator is used.
  - `AWGC:CLOC:SOUR EXT` specifies that the clock signal from external oscillator is used.

  `[SOURce[1]]:ROSCillator:TYPE`

- This command selects the type of the reference oscillator. This parameter is valid only when Clock Source is Internal and Reference Source is External.
  - `SOURCE1:ROSCILLATOR:TYPE FIXED` selects a fixed frequency external reference oscillator. The frequency is fixed to 10 MHz, 20 MHz, or 100MHz.